ODESSA ASTRONOMICAL PUBLICATIONS

Volume 28 Issue 1
(2015)
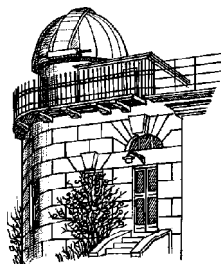
CONTENTS

DEPRESSION IN THE CONTINUOUS SPECTRUM OF SOLAR RADIATION IN THE REGION 6500 − 8200 Å

O.M.Stelmakh, N.L.Tyshko

Department of Astrophysics of Ivan Franko National University of Lviv,
Ukraine, *omstelmakh@gmail.com*

ABSTRACT. Based on the authors' computations of cross-sections of the basic processes which form continuous absorption in the photospheres of solar-type stars, the spectral dependence of the solar radiation intensity in the continuous spectrum in the visible and infrared regions has been investigated. It is shown that the depression observed in the continuous spectrum of solar radiation in the region $(6500 − 8200)$ Å is caused by the processes of photoionization of neutral hydrogen atoms excited up to the energy levels with the principal quantum number $n = 3$. The results of computation are in good agreement with the data observed.

Key words: cross-sections, continuous absorption, solar radiation intensity.

PACS 95.30.-k, 95.30.Cq, 96.60.-j, 97.10.Ex

1. Introduction

As is known, base on observations, Milne (1922) established general properties of the continuous absorption coefficient $æ_c(\lambda)$ of the Sun in the visible and infrared parts of the spectrum – with maximum near 9000 Å, deep minimum at 16400 Å and the subsequent growth at larger wavelengths. The suggestion made by Wildts (1939) that photoionization of negative hydrogen ions is the main mechanism of the continuous absorption explained the behaviour of $æ_c(\lambda)$ at $\lambda < 16400$ Å. Smith & Burch (1959), aimed to obtain precise measurement of the relative cross section $\sigma(\lambda)/\sigma(\lambda_0)$ (at $\lambda_0 = 5280$ Å) of the hydrogen ion photoionization under laboratory experimental conditions, found the presence of a fine structure in the region $(6500 − 8200)$ Å. It should be noted that in fact the effective cross-section of the hydrogen atom photoionization was determined during that experiment, and the H^- photoionization is just one of the processes, which, however, make a major contribution. The results of observations by Münchs (1948) are also indicative of specific features of $æ_c(\lambda)$ in the neighborhood of the maximum. Computations of $æ_c(\lambda)$ performed by Chandrasekhar & Breen (1946), base on Wildt's suggestion, showed no fine structure in the vicinity of the maximum. More accurate computations of the relative cross-section of the photoionization of H^- ion, which

were carried out with multiparameter variational wave functions by Geltman's (1962), appeared to be very close to the results obtained by Smith & Burch (1959) throughout all regions, except that one of maximum where the deviation was of the order of 2%. Neither Geltman nor other authors of later theoretical works (John (1988), Rau (1996)) paid any attention to these differences.

From general physical considerations it is clear that the photoionization of excited hydrogen atoms in the states with principal quantum number $n \geq 3$ should affect the continuous absorption in the small region at $\lambda < 8200$ Å. Primarily, it regards the ionization of atoms with $n = 3$, for which the ionization energy is equal to $0,1111... Ry$ that is twice as high as the H^- ionization energy $(0,0555... Ry)$. Although the photoionization of such excited atoms is analogous to that one of the H^- ions, these processes can not make a great contribution in quantitative terms as the concentration of excited atoms under the solar conditions is low.

Over the recent decades, the investigation of spectral dependence of the solar radiation intensity was a subject of a significant number of works performed with high accuracy (Burlov-Vasil'ev, Vasil'eva & Matveev, 1996). This raises the problem of detailed calculation of the continuous absorption coefficient for the purpose of interpreting the observed solar spectrum in the vicinity of the region $(6500 − 8200)$ Å, as well as clearing up the role of the excited hydrogen atom photoionization processes in the formation of spectra of stars similar to the Sun.

2. Cross-sections of the basic processes and continuous absorption coefficient

The continuous absorption coefficient in the visible and infrared regions of the spectrum for solar-type stars has the form:

$$æ_c(\lambda) = \{1 - \exp[-hc/\lambda T k_B]\} \times \qquad (1)$$

$$\times \left\{ \frac{N_{H^-}}{V} \sigma_{H^-}(\lambda) + \sum_{n \geq 1} \frac{N_H^{(n)}}{V} \sigma_H^{(n)}(\lambda) + \right.$$

$$+\frac{N_e}{V}\sigma_{ee}(\lambda) + \sum_a \frac{N_a}{V}\sigma_a(\lambda)\Bigg\},$$

where $\sigma_{H^-}(\lambda)$ is the cross-section of the photoionization process of isolated H^- ion; N_{H^-}/V is the concentration of H^- ions; $\sigma_H^{(n)}(\lambda)$ is the cross-section of photoionization of a neutral hydrogen atom in the state with the principal quantum number n; $N_H^{(n)}/V$ is the concentration of such atoms; $\sigma_{ee}(\lambda)$ is the cross-section of photon absorption by either a free electron which is in the field of hydrogen atoms in different states, or protons, or electrons, or other charged and neutral particles; N_e/V is the concentration of electrons; $\sigma_a(\lambda)$ is the cross-sections of photon interaction with other micro-particles (atoms and ions of helium, metals, etc.); N_a/V is the concentration of particles of the corresponding class. The sum

$$\sigma_{eff}(\lambda) \equiv \sigma_{H^-}(\lambda) + \sum_{n\geq1}\frac{N_H^{(n)}}{N_{H^-}}\sigma_H^{(n)}(\lambda),$$

$$\sigma_H^{(n)}(\lambda) = \sum_0^{n-1}\sigma_{n,l}(\lambda) \tag{2}$$

can be interpreted as an effective cross-section of hydrogen in visible and infrared regions os the spectrum as it is defined by bound-free transition in the H^- ions and neutral hydrogen atoms. This value per se corresponds to the results of measurements obtained by Smith & Burch (1959).

In this study we used the cross-sections $\sigma_{H^-}(\lambda)$ computed within the framework of basic approach in Vavrukh & Stelmakh (2013). As can be seen in Figure 1, it is very close to the most accurate calculation by Geltmans (1962). The thin curve in Fig. 1 represents the $\sigma_{eff}(\lambda) = \sigma_{H_-}(\lambda)$ aproximation.

For convenience, we will henceforth use the dimensionless wavelength $\lambda_* = \lambda/\lambda_0$, where $\lambda_0 = 4\pi a_0\alpha_0^{-1} = 911{,}27...$ Å (α_0 is the fine structure constant, a_0 – the Bohr radius). The cross-section $\sigma_{H^-}(\lambda)$ has zero asymptotics near the red limit of $\Lambda_* = (\Delta\varepsilon)^{-1} \cong 18{,}018...$ (where $-\Delta\varepsilon$ is the H^- ion ionization potential in Rydberg);

$$\sigma_{H^-}(\lambda) \sim (\lambda_* - \Lambda_*)^{3/2} \quad \text{at} \quad \lambda_* \to \Lambda_*. \tag{3}$$

Such behavior of $\sigma_{H^-}(\lambda)$ is conditioned by the fact that the photoelectron wave function in the weak field of a neutral hydrogen atom is close to the plane wave. The asymptotics of cross-section of the isolated hydrogen atom photoionization, computed by the photoelectron wave functions in the proton's Coulomb field (Karzas & Latter, 1961) are different:

$$\sigma_{n,l}(\lambda) \sim \begin{cases} x_n^{7/2+l} & \text{at} \quad x_n \ll 1, \\ x_n^3\Theta(1-x_n) & \text{at} \quad x_n \to 1, \end{cases} \tag{4}$$

where $x_n = \lambda_*/n^2$, $\Theta(z)$ is a single theta-function; l is the orbital quantum number.
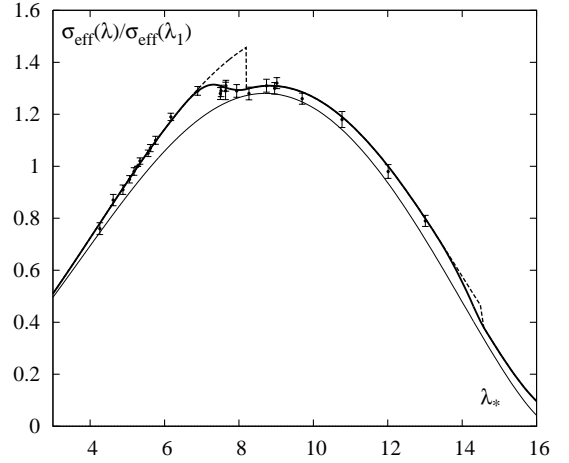
Figure 1: The spectral dependence of the effective relative cross-section in different approximations. Marks on the graph show the experimental results by Smith & Burch (1959).

Fig. 2 illustrates the spectral dependence of cross-section $\tilde{\sigma}_{3,l}(\lambda) = (\alpha_0 a_0^2)^{-1}\sigma_{3,l}$. The dashed curve in the Fig. 1 shows the effective cross-section in the vicinity of the maximum in approximation:

$$\sigma_{H^-}(\lambda) + \frac{N_H^{(3)}}{N_{H^-}}\sum_{l=0}^2\sigma_{3,l}(\lambda) + \frac{N_H^{(4)}}{N_{H^-}}\sum_{l=0}^3\sigma_{4,l}(\lambda). \tag{5}$$

As is seen from Fig. 1, such an approximation describes the results of Smith & Burch (1959) quite well; however, the deviation in the region $(6500 - 8200)$ Å is essential. It can be caused by the fact that the final stage of the the hydrogen atom photoionization in the vacuum differs from that one in the partially ionised
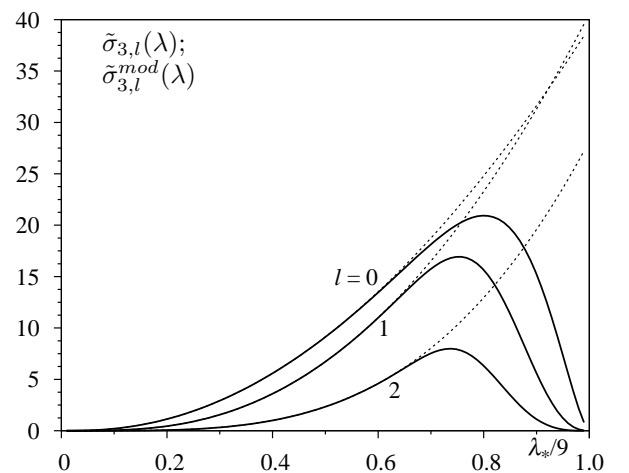
Figure 2: Dashed curves represent spectral dependences of the functions $\tilde{\sigma}_{3,l}(\lambda)$ while solid curves correspond to the model cross-sections $\tilde{\sigma}_{3,l}^{mod}(\lambda)$ at $b_{n,l} = 4{,}0$.

plasma. In vacuum the photoelectron is in the protons' Coulomb field. The duration of the photoelectron stay in the vicinity of the parent atom in the partially ionised photospheric plasma

$$\tau_1 = R/v_e \qquad (6)$$

can exceed the recombination time of the free electron with a proton:

$$\tau_2 = R/v. \qquad (7)$$

Here R is of the order of the Debye radius R_D, and the photoelectron speed is determined by the condition

$$\frac{m}{2}v_e^2 = \hbar\omega - \Delta E_n = \frac{e^2}{2a_0}(\omega_* - \Delta\varepsilon_n), \qquad (8)$$

where $\Delta\varepsilon_n$ is the ionization energy in Rydberg; and v is the mean square speed at the given temperature ($v^2 = 3k_B T/m$). Given that $\tau_1 > \tau_2$ ($v_e^2 < v^2$), we find that

$$\lambda_* > \lambda_*^{max}\left\{1 + \frac{3}{2}\lambda_*^{max}t\right\}^{-1} = \lambda_*^0, \qquad (9)$$

where $t = k_B T/Ry$ is the dimensionless photospheric temperature; $\lambda_*^{max} = n^2$. For $n = 3$ at the effective solar temperature $6\cdot 10^3$K we have $\lambda_*^0 \approx 6$, for $n = 4$ – $\lambda_*^0 \approx 8$, while $\lambda_*^0 \approx 10$ for $n = 5$. As it follows from formula (9), the photoelectron with low energy most of the time spends in the weak field of neutral hydrogen atom rather in the proton's Coulomb field. Therefore, at $\lambda_* < \lambda_*^0$ the correct cross-sections $\sigma_{n,l}(\lambda)$ are those ones calculated with the Coulomb photoelectron functions while at $\lambda_* > \lambda_*^0$ – those calculated by the functions close to plane waves. The latter have zero asymptotic at $\lambda_*^{max} = n^2$. As an example, we present the asymptotic of the cross-sections, calculated by the plane waves at $n = 3$

$$\sigma_{3,l}(\lambda) \approx \pi\alpha_0 a_0^2 2^{8+2l}3^{3-l}(x)^{7/2+l}(1-x)^{3/2+l}, \quad (10)$$

where $x = \lambda_*/9$. To approximately factor in the effects of recombination processes, the joining of the cross sections from the study by Karzas & Latter (1961) with those from (10) was used in the study by Vavrukh & Stelmakh (2013). In this paper we used the model cross-sections:

$$\sigma_{n,l}^{mod}(\lambda) = \sigma_{n,l}(\lambda) \times \qquad (11)$$
$$\times\left\{1 - \exp\left[-b_{n,l}\left(\frac{1 - \lambda_*/n^2}{1 - \lambda_*^0/n^2}\right)^{3/2+l}\right]\right\},$$

where $\sigma_{n,l}(\lambda)$ are the cross-sections calculated by the Coulomb functions by Karzas & Latter (1961); and parameters $b_{n,l} \sim 1$ are chosen in such a way that $\sigma_{n,l}^{mod}(\lambda)$ are close to the expression (10) near a red limit (Fig. 2). The thick curve in Fig. 1 corresponds to approximation (5) where $\sigma_{n,l}^{mod}(\lambda)$ is used instead of $\sigma_{n,l}(\lambda)$. The computation results correspond to the

temperature $T = 6\cdot 10^3$ K and the dimensionless barion concentration $\rho a_0^3 (m_H)^{-1} = 5 \cdot 10^{-8}$.

When calculating the cross-section of photon absorption by free electrons, we took into account the presence of protons and neutral hydrogen atoms in the ground and excited states. Approximately, the potential energy of an electron in the field of these particles can be presented in the form

$$V_e(\mathbf{r}) \cong \frac{1}{V}\sum_{\mathbf{q}}\{V_{ep}(\mathbf{q})S_p(-\mathbf{q}) + \qquad (12)$$
$$+ \sum_{n\geq 1}V_{eH}^{(n)}(\mathbf{q})S_H^{(n)}(-\mathbf{q})\}e^{i(\mathbf{q},\mathbf{r})},$$

where $S^p(-\mathbf{q}) = \sum_{j=1}^{N_p}\exp[-i(\mathbf{q}, \mathbf{R}_j^p)]$ is the structure factor of a proton subsystem; $\mathbf{R}_j^p$ is the radius vector of the j-th proton; $S_H^{(n)}(-\mathbf{q})$ is the structure factor of a neutral hydrogen atoms, which are in the state with the principal quantum number n;

$$V_{ep}(\mathbf{q}) = -4\pi e^2 a_0^2\{q_*^2 + \xi^2\}^{-1} \equiv \qquad (13)$$
$$\equiv 4\pi e^2 a_0^2 v_{ep}(q_*)$$

is a Fourier energy of the electron-proton interaction taking into account screening effects ($q_* = qa_0$, $\xi = a_0/R_D$ is the dimensionless reciprocal screening radius), with only s-states for centrally-symmetric potentials of electron-atom interaction accounted for. We obtain the following expressions:

$$V_{eH}^{(n)}(\mathbf{q}) = 4\pi e^2 a_0^2 v_{eH}^{(n)}(q_*);$$
$$v_{eH}^{(1)}(\mathbf{q}_*) = -(8 + q_*^2)(4 + q_*^2)^{-2}; \qquad (14)$$
$$v_{eH}^{(2)}(\mathbf{q}_*) = \{6 + 2q_*^2 + 3q_*^4 + q_*^6\}(1 + q_*^2)^{-4};....$$

In the Bohr approximation and at chaotic spatial distribution of particles when $< S_p(\mathbf{q})S_p(-\mathbf{q}) >= N_p$, $< S_H^{(n)}(\mathbf{q})S_H^{(n)}(-\mathbf{q}) >= N_H^{(n)}$, $< S_H^{(n)}(\mathbf{q})S_p(-\mathbf{q}) >= 0$,

$$\sigma_{ee}(\lambda) = \alpha_0 a_0^2 \pi^{3/2}\lambda_*^3 \frac{2^9}{3}\int_0^\infty dk\, k\, e^{-k^2/t}\int_{z_-}^{z_+} dz\, z \times (15)$$

$$\times\left\{\frac{N_p}{V}a_0^3 v_{ep}^2(z^{1/2}) + \sum_{n=1,2}\frac{N_H^{(n)}}{V}[v_{eH}^{(n)}(z^{1/2})]^2 + ...\right\},$$

where

$$z_- = (k - k_0)^2, \quad z_+ = (k + k_0)^2, \qquad (16)$$
$$k_0 = (k^2 + \lambda_*^{-1})^{1/2};$$

N_p/V is the proton concentration. At the ionization equilibrium under conditions of solar photosphere, the contribution into cross-section $\sigma_e(\lambda)$ made by an electron-proton interaction is of the same order as the contribution caused by interaction of electrons with hydrogen atoms in the ground state. The contribution
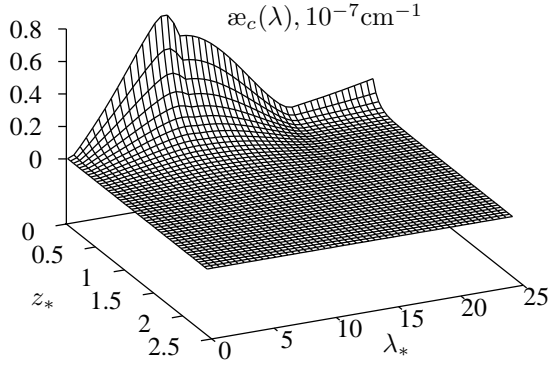
Figure 3: The spectral and coordinate dependence of the continuous absorption coefficient for the Sun.

due to the interaction of electrons with excited atoms is small. Generally, the contribution of the processes of photon absorption by free electrons to the continuous absorption coefficient in the region of maximum $æ_c(\lambda)$ is small. However, this contribution is essential in the wavelength region $\lambda > 14 \cdot 10^3$ Å.

3. Solar radiation intensity in the continuous spectrum

For the center of the solar disc the intensity of radiation in the continuous spectrum was calculated by the standard formula

$$I_\lambda = \int\limits_0^{z_0} dz\, æ_c(\lambda|z)\, B_\lambda(z) \exp\left\{ -\int\limits_z^{z_0} dz\, æ_c(\lambda|z) \right\},$$
(17)

where the Planck distribution function $B_\lambda(z) = \frac{4\pi c^2 \hbar}{\lambda_0^5} \frac{1}{\lambda_*^5} \{\exp[-\lambda_*^{-1} t(z)^{-1}] - 1\}^{-1}$ which accounts for the sum over photons polarization is used as the source function. We have chosen a plane-parallel model of atmosphere with the thickness $z_0 = 240$ km (Aller, 1971), in which the density and temperature distribution along the radius are approximated in the following form:

$$\rho(z) = \rho_0 \exp\left\{ -\frac{az_*}{t(z_*)} \right\},$$
(18)

$$t(z_*) = t_0 \exp\left\{ -\frac{bz_*}{1 + cz_*} \right\},$$

where $t_0 = T_0 k_B (e^2/2a_0)^{-1}$; $\rho_0 = 0{,}450 \cdot 10^{-6}$ g/cm³; $T_0 = 7{,}3 \cdot 10^3$ K; $a = 2{,}45$; $b = 0{,}36$; $c = 0{,}33$, $z_* = z \cdot 10^{-7}$ cm. The continuous absorption coefficient $æ_c(\lambda|z)$ for this atmosphere is shown in Fig. 3. The equilibrium concentration of particles for the given density and temperature werw calculated by the self-consistent method, which is examined in details for the hydrogen-helium model by Stelmakh (2014).

The results of numerical calculation I_λ in terms of

10^{14} J /s m³ sr. are shown in Fig. 4 (curve 1). The Figure also presents the results of the intensity measurement by Burlov-Vasil'ev, Vasil'eva & Matveev (1996) in the region $(6 - 11) \cdot 10^3$ Å. Curve 2 was calculated on the base of $æ_c(\lambda|z)$, not accounting for the cross-sections of the excited hydrogen atom photoionization at $n = 3$ and $n = 4$. As is seen from the Figure, the spectral behavior of curve 1 is similar to that of the curve, ploted by the observation data. Both curves have a deflection in the region $(6500 - 8200)$ Å relative to curve 2.
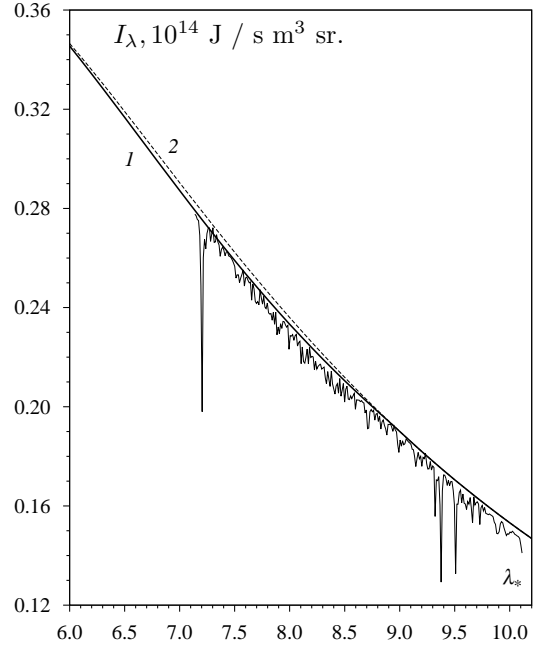
Figure 4: The continuous radiation intensity for the solar disk center.

As follows from our computations, the depression on the curve for the solar radiation intensity spectral distribution in the region $(6500 - 8200)$ Å is caused by the photoionization of neutral hydrogen atoms excited to the energy levels of the principal quantum number $n = 3$.

If the cross-sections of excited hydrogen atom photoionization, calculated by the Coulomb functions, are used, then there is a jump of the calculated curve of the solar radiation intensity in the continuous spectrum in the region 8200 Å; that is inconsistent with the data observed. The model cross-sections are in good agreement, which is indicative of their correct qualitative spectral dependence.

As is known, the intensity of solar radiation in the ultraviolet region depends on the phase of activity. In the phase of maximum it is 2-3 times higher than in the minimum intensity phase. Therefore, the concentration of hydrogen atoms, excited to the level with $n = 3$, can vary over 11-year cycle, and that can affect the depth of depression in the region $(6500 - 8200)$ Å.

Besides the point, the measurements of the solar radiation intensity, which provided the basis of paper by Burlov-Vasil'ev, Vasil'eva & Matveev (1996), had been performed during the period of minimum solar activity.

Depression, which is discussed in this paper, must also be observed in the spectra of stars of other spectral classes, in which the photoionization of negative hydrogen ions is the main mechanism of continuous absorption formation. In the spectra of the hotter stars, such depression should be stronger while its exhibitions will be weak and irregular in the stars with $T_{eff} < 5 \cdot 10^3$ K.

References

Milne E.: 1922, *Philos. Trans. Roy. Soc.*, **223**, 201.

Smith S., Burch D.: 1959, *Phys. Rev.*, **116**, 5.

Wildt R.: 1939, *Astrophys. J.*, **89**, 295 and **90**, 611.

Münch G.: 1948, *Astrophys. J.*, **108**, 116.

Chandrasekhar S., Breen F.: 1946, *Astrophys. J.*, **104**, 430.

Geltman S.: 1962, *Phys. Rev.*, **136**, 935.

Vavrukh M., Stelmakh O.: 2013, *J. of Phys. Studies.*, **17**, N 4, 4902.

John T.: 1988, *Astron. Astrophys.*, **193.**, 189.

Rau A.R.P.: 1996, *J.Astrophys. Astr.*, **17**, 113.

Karzas W., Latter R.: 1961, *Ap. JS.*, **6**, 167.

Aller L.: 1971, *Atoms, Stars and Nebulae*, Massachusets, 352.

Stelmakh O.: 2014, *Visnyk of Lviv University. Series Physics*, **49**, 39.

Burlov-Vasil'ev K., Vasil'eva I., Matveev Yu.: 1996, *Kinem. Phys. Celest. Bodies*, **12**, N 3, 75.

THE STUDY OF TIMING RELATIONSHIPS WHICH ARISE WHEN USING A TELEVISION CCD CAMERA WATEC WAT-902H2 SUPREME IN ASTRONOMICAL INVESTIGATIONS

V.V.Dragomiretsky, A.V.Ryabov, N.I.Koshkin

Astronomical Observatory, Odessa National University
Shevchenko Park, 65014, Odessa, Ukraine
andryabov(a)gmail.com

ABSTRACT. The present paper describes the study of timing relationships which arise when using an analogue CCD camera Watec WAT-902H2 Sup in astronomical investigations, particularly in time-domain measurements of LEO satellites which are fast-moving against stellar background.

An analogue CCD camera Watec WAT-902H2 Sup is used to observe artificial Earth satellites using theodolite KT-50 at the Astronomical Observatory of Odessa National University. Specific character of the LEO satellite observations requires recording instants of observations with the highest possible precision (Flohrer, 2008; Shakun & Koshkin, 2014).

To carry out the time reference to the UTC time scale, a timing signal from a GPS receiver is introduced into the CCD camera video output signal. The rising edge of the timing signal is synchronised with the beginning of a UTC second. The number of the UTC second is transmitted using a special code which allows of further automatic procession. The procedure of time referencing is described in detail in (Dragomiretsky et al., 2013; Research Report No 365, 2008).

As the reference to timing signals is carried out in the video output, there is a certain time interval between the instant of an astronomical event's observation and the instant of time referencing. To determine the length of this time interval the laboratory tests of the CCD camera Watec WAT-902H2 Sup were performed.

At the first stage of the laboratory tests the CCD camera was exposed to the strobe illumination with the further video signal recording and processing. The strobe flash duration was $1 \cdot 10^{-6}$s with the frequency of 20-100 Hz. The indicated tests were carried out both using uniform strobe illumination of the whole sensitive surface and with the light source focusing on a given area of the sensitive surface. Based on the results of these two tests, we concluded that when the CCD camera WAT-902H2 Sup runs in the mode of low ambient illumination with disabled AGC system, simultaneous recording of all events on the whole sensitive surface is performed. At that it is only possible to discuss the instants of the beginning and end of exposure in a similar way to the application of photo-sensitive emulsions.
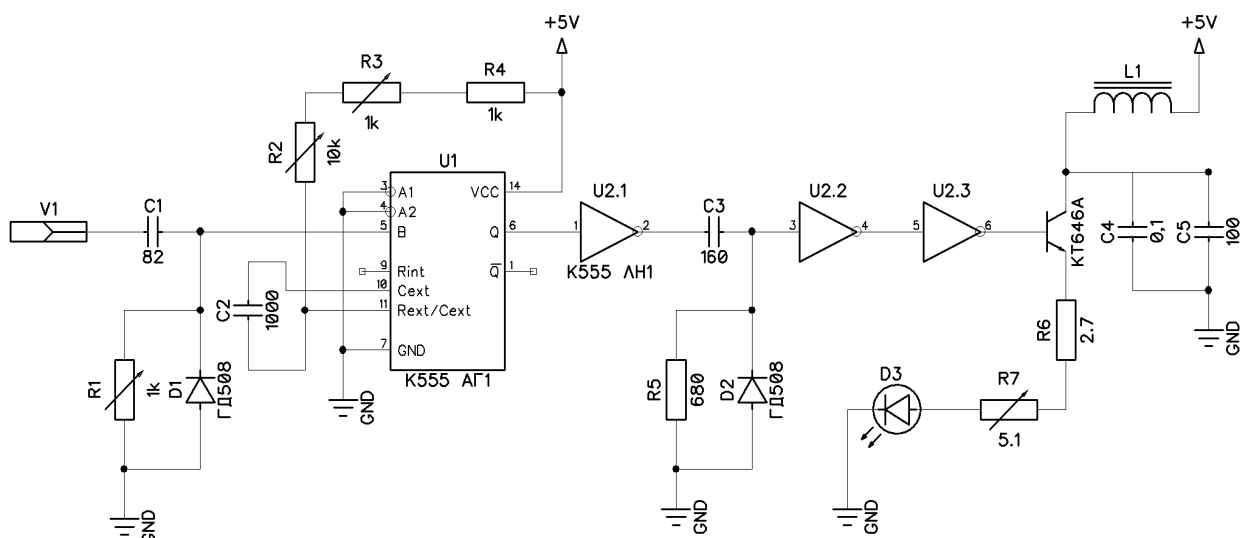
Figure 1.

Further investigations are focused on the determination of time intervals between the instant of recording of an astronomical event and the instant of time referencing of the video output with GPS signals. We used a stroboscope synchronised with procedure signals generated by the CCD camera. The stroboscope circuit is presented in Fig. 1. The strobe is synchronised with the signal *V1* generated by the timing controller CXD2463R integrated into the CCD camera (http://www.alldatasheet.com/datasheet-pdf/pdf/47009/SONY/CXD2463R.html). The connection of a stroboscope did not impair the CCD camera performance. The stroboscope circuit produces an intense electric impulse of 0.4 μs duration with a delay of 1÷8 μs relative to the rising edge of the signal *V1*. This delay is controlled by the resistors *R2* and *R3*. The stable synchronisation level is set by the resistor *R1*. The light pulse level is controlled by the resistor *R7*. It is assumed that the duration of the LED afterglow emission does not exceed 0.5 μs. Thus, the light pulse duration is no more than 1 μs. The CCD camera's dead zone (Fig. 2) was found by changing the light pulse delay. The dead zone where the sensitivity is completely lost is between the falling edge of the signal *V1* and the rising edge of the signal *V3* (http://www.alldatasheet.com/datasheet-pdf/pdf/47009/SONY/CXD2463R.html). The zone of reduced sensitivity was also found in the range between the rising edge of the signal *V1* and the falling edge of the signal *V3*.

It can be concluded from the above that the exposure of the previous frame ends when the signal *V1* is active while the exposure of the next frame begins when the signal *V3* is active.

The shape of the CCD camera video signal output is shown in Fig. 3. The beginning of the X-axis corresponds to the rising edge of the signal *V1*. In fact, a part of the video output signal between the rising edge of the signal *V1* and the beginning of the first image line corresponds to a certain part of the vertical synchronization pulse (https://commons.wikimedia.org/wiki/File:BAS_Zeilensig nal_unmoduliert_1.svg). As this part of the frame sync pulse remains constant when the camera WAT-902H2 Sup is operated in the above-indicated mode, it is possible to calculate the time constant correction between the end of the previous frame's exposure and the beginning of the first whole line of the corresponding video output signal.

As follows from the graph presented in Fig. 3, the time interval between the instant of time corresponding to the rising edge of the signal *V1* and the instant corresponding to the beginning of the first whole line of the video output signal is equal to 24 μs and nine complete periods corresponding to the video output line duration. Thus, the indicated time interval is $\Delta t = 24 + 9 \cdot 64 = 600$ *(μs)*. As follows from the graph presented in Fig. 2, the middle of the dead zone where the sensitivity is lost is separated in time by 3.55 μs from the instant of the *V1* signal's rising edge. Therefore, the time interval between the instant of the end of the previous frame's exposure and the instant of the beginning of the first whole data line of the corresponding video output signal is $t = (\Delta t - 2.3)$ *μs*, which makes *597.7μs*.
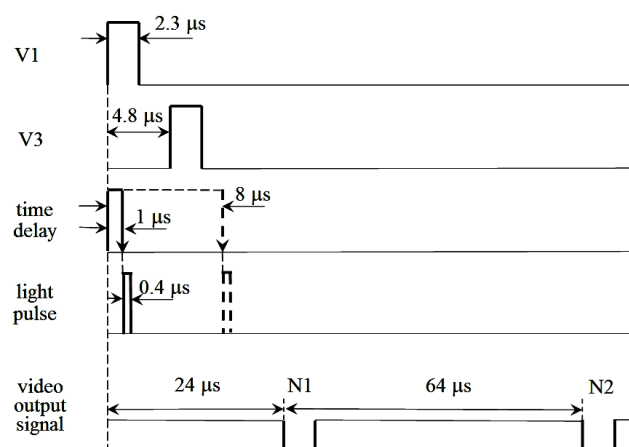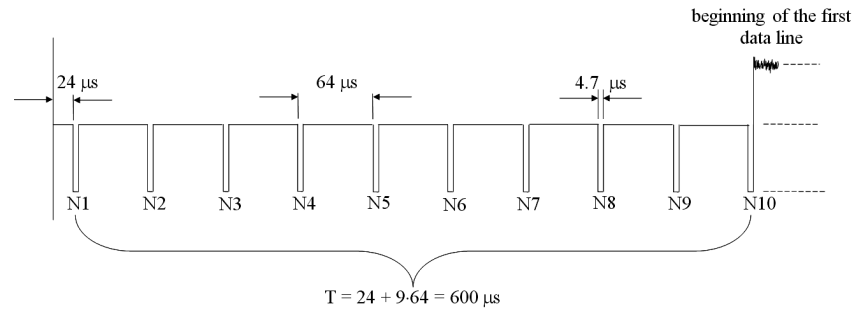
Figure 2.

Figure 3.

Accounting for the duration of the detected dead zone, the frame exposure time for the indicated mode is *19.9975 ms*. Thus, the time interval between the instant of the beginning of the previous frame's exposure and the instant of the beginning of the first whole data line of the corresponding video output signal is ($t + 19.9975$) *ms*, which makes *20.5952 ms*. If the frame exposure is reduced to the average instant of time, then the time interval between the average instant of the previous frame's exposure and the instant of the beginning of the first whole data line of the corresponding video output signal is $t + 19.9976/2$ (*ms*), which makes *10.59645 ms*.

The obtained time corrections are used to specify the instants of observations of artificial Earth satellites using theodolite KT-50. The video signal standards given in https://commons.wikimedia.org/wiki/File:BAS_Zeilensig nal_unmoduliert_1.svg were used to perform calculations. The time interval between the instant of the beginning of the first whole data line and the instant of the arrival of a timing signal from a GPS receiver is determined according to the methods specified in (Dragomiretsky et al., 2013; Research Report No 484, 2014].

References

Flohrer C. Mutual Validation of Satellite-Geodetic Techniques and Its Impact on GNSS Orbit Modeling. Volume 75. Swiss Geodetic Commission, Zurich, Switzerland, 2008. (http://www.sgc.ethz.ch/publications.html)

Shakun L.S., Koshkin N.I. Determination of Visible Coordinates of the Low-Orbit Space Objects and Their Photometry by the CCD Camera with the Analogue Output. Initial Image Processing. *Adv. in Space Res.*, **53**, Issue 12, 2014, 1834-1847.

Dragomiretsky V.V., Koshkin N.I., Korobeinikova E.A., Melikyants C.M., Ryabov A.V., Strakhova S.L., Terpan S.S., Shakun L.S. Timing of Satellite Observations for Telescope with TV CCD Camera. *Bulletin of Ukrainian Earth Orientation Parameters Laboratory*, 2013, **8**, 75-78.

Research Report No 365: Investigation of Drag-Free Motion of Artificial Earth Satellites and Asteroids as well as Ecological Problems in Near-Earth Space. Odessa, ONU, 2008, 111p. (Registration Number 0106U001670).

http://www.alldatasheet.com/datasheet-pdf/pdf/47009/SONY/CXD2463R.html

Video Signal Standards: BAS-Zeilensignal und Verzögertes Signal (https://commons.wikimedia.org/wiki/File:BAS_Zeilensignal_unmoduliert_1.svg)

Research Report No 484: The Study of Motion and Fragmentation of Meteor and Artificial Bodies in the Earth's Atmosphere and Interplanetary Space. Odessa, ONU, 2014, 167p. (Registration Number 0112U001749).

10 NEW VARIABLE STARS DETECTED BY CRTS

Andrey Galinskiy, Sergei Dubrouski, Igor Baluk

The Regional Centre of Technical Creativity of Children and Youth (RCTCCY),
Oktyabrya avenue, 36 A, Gomel, Belarus
andigall@yandex.ru, toliman@tut.by, balig@tut.by

ABSTRACT. 10 new variable stars were found by CRTS.

Key words: Stars: new variable stars.

The authors carried out investigation using the time series photometry data from the Catalina Real-Time Transient Survey (CRTS) in 2013-2015. About 3,000 new variable stars were found. The data for 10 the most recently discovered stars are presented in the journal Odessa Astronomical Publications.

SSS_J041936.0-502614

The star was discovered by I.I.Baluk.

The UCAC4 position of the star: RA = $04^h19^m35.937^s$, Dec = -50°26′51″.03.

The star's catalogue identifiers: the 2MASS identifier – J04193593-5026149; the USNO identifier – B1.0 0395-0035953; the UCAC4 identifier – 198-004300.

The star's variability type: EA, the peak brightness is 15.40^m; the minimum brightness is 16.07^m (in the C and V band); the secondary minimum brightness is 15.70^m (in the C and V band). The star's light ephemerides are plotted in Figure 1. D = 0.18.
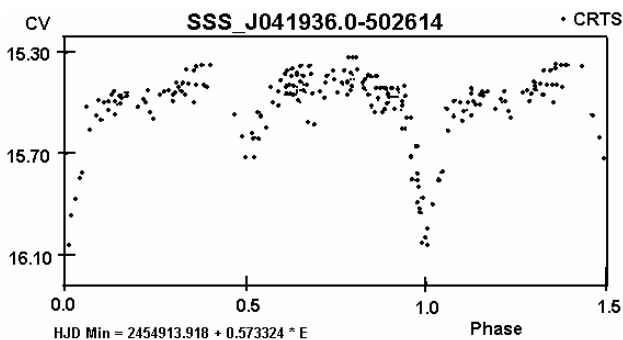
Figure 1

SSS_J065711.3-512110

The star was discovered by I.I.Baluk.
The UCAC4 position of the star: RA = $06^h57^m11.314^s$, Dec = -51°21′10″.47.

The star's catalogue identifiers: the 2MASS identifier – J06571131-5121104; the USNO identifier – B1.0 0386-0064392; the UCAC4 identifier – 194-009935.

The star's variability type: SRA, the peak brightness is 11.80^m; the minimum brightness is 12.70^m (in the C and V band). The star's light ephemerides are plotted in Figure 2. J-K = 1.35.
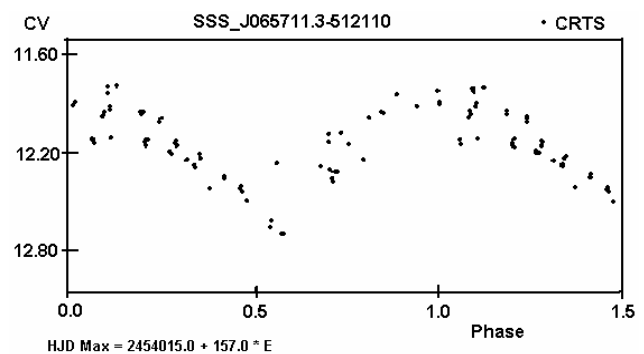
Figure 2

SSS_J195851.4-521601

The star was discovered by I.I.Baluk.

The PPMXL position of the star: RA = $19^h58^m51.384^s$, Dec = -52°16′01″.80.

The star's catalogue identifiers: the 2MASS identifier – J19585138-5216017; the USNO identifier – B1.0 0377-1050512.

The star's variability type: EW, the peak brightness is 17.10^m; the minimum brightness is 17.40^m (in the C and V band).

The star's light ephemerides are plotted in Figure 3.
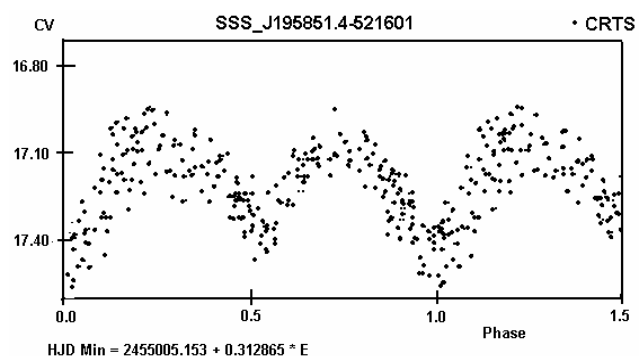
Figure 3

SSS_J020922.2-525228

The star was discovered by A.L.Galinskiy.

The UCAC4 position of the star: RA = $02^h09^m22.139^s$, Dec = -52°52′28″.37.

The star's catalogue identifiers: the 2MASS identifier – J02092213-5252284; the USNO identifier – B1.0 0371-0017475; the GSC identifier – 08483-00062; the UCAC4 identifier – 186-001925.

The star's variability type: SR, the peak brightness is 14.90^m; the minimum brightness is 15.29^m (in the C and V band). The star's light ephemerides are plotted in Figure 4. J-K = 1.18.
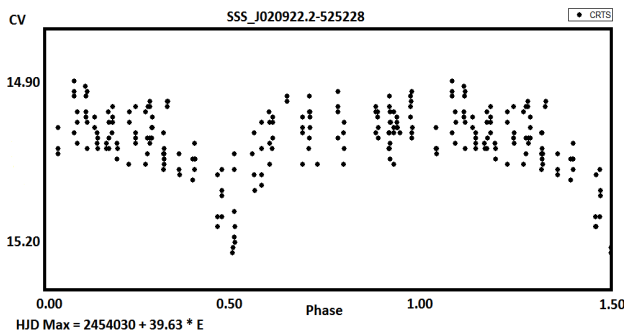
Figure 4

SSS_J035759.1-515819

The star was discovered by A.L.Galinskiy.

The PPMXL position of the star: RA = $03^h57^m59.139^s$, Dec = -51°58′19″.39.

The star's catalogue identifiers: the 2MASS identifier – J03575913-5158193; the USNO identifier – B1.0 0380-0047211; the GSC identifier – 08073-00336.

The star's variability type: SR, the peak brightness is 15.50^m; the minimum brightness is 15.98^m (in the C and V band). The star's light ephemerides are plotted in Figure 5. J-K = 1.21.
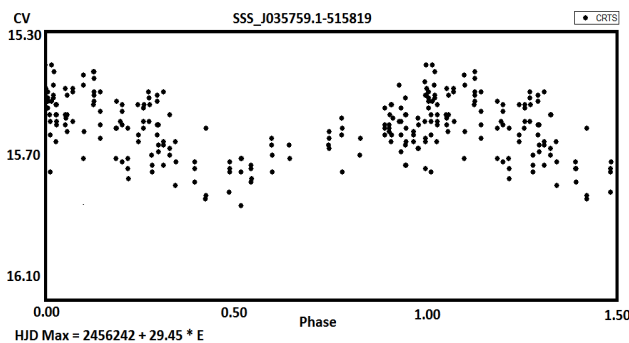
Figure 5

SSS_J073103.3-525443

The star was discovered by A.L.Galinskiy.

The UCAC4 position of the star: RA = $07^h31^m03.297^s$, Dec = -52°54′43″.63.

The star's catalogue identifiers: the 2MASS identifier – J07310329-5254436; the USNO identifier – B1.0 0370-0086299; the UCAC4 identifier – 186-012398.

The star's variability type: SR, the peak brightness is 12.10^m; the minimum brightness is 12.90^m (in the C and V band). The star's light ephemerides are plotted in Figure 6. J-K = 1.27.
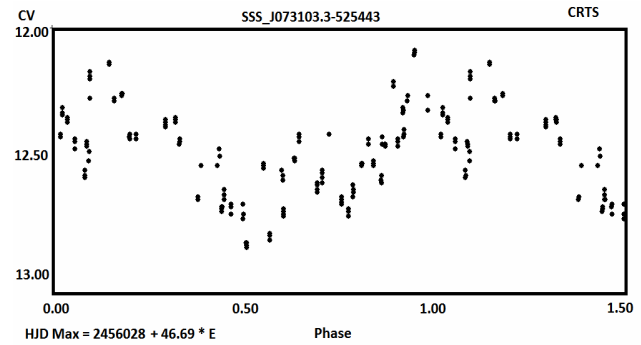
Figure 6

SSS_J100550.3-282525

The star was discovered by A.L.Galinskiy.

The UCAC4 position of the star: RA = $10^h05^m50.317^s$, Dec = -28°25′25″.14.

The star's catalogue identifiers: the 2MASS identifier – J10055031-2825251; the USNO identifier – B1.0 0615-0234047; the GSC identifier – 06629-01092; the UCAC4 identifier – 308-062711.

The star's variability type: EA, the peak brightness is 14.59^m; the minimum brightness is 14.90^m (in the C and V band); the secondary minimum brightness is 14.69^m (in the C and V band). The star's light ephemerides are plotted in Figure 7. D = 0.16.
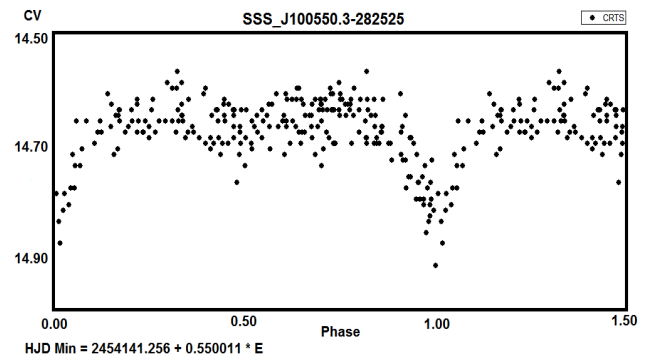
Figure 7

SSS_J101916.8-281924

The star was discovered by A.L.Galinskiy.

The UCAC4 position of the star: RA = $10^h19^m16.838^s$, Dec = -28°19′25″.02.

The star's catalogue identifiers: the 2MASS identifier – J10191683-2819250; the USNO identifier – B1.0 0616-0240796; the GSC identifier – 06630-00805; the UCAC4 identifier – 309-061750.

The star's variability type: EB, the peak brightness is 14.30^m; the minimum brightness is 14.60^m (in the C and V band); the secondary minimum brightness is 14.45^m (in the C and V band).

The star's light ephemerides are plotted in Figure 8.
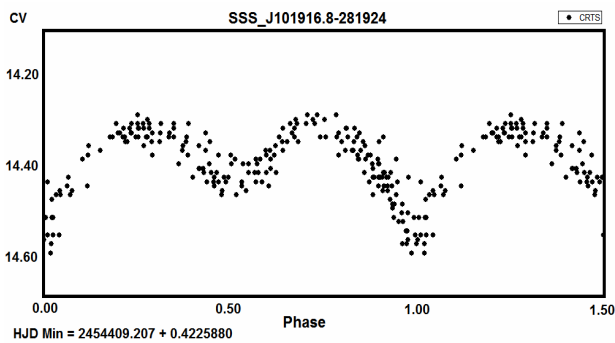
Figure 8

SSS_J073149.9-505012

The star was discovered by A.L.Galinskiy.

The UCAC4 position of the star: RA = 07^{h}31^{m}49.879^s, Dec = -50°50′12″.48.

The star's catalogue identifiers: the 2MASS identifier – J07314986-5050124; the USNO identifier – B1.0 0391-0077713; the GSC identifier – 08145-00452; the UCAC4 identifier – 196-013096.

The star's variability type: SRA, the peak brightness is 11.00^m; the minimum brightness is 12.10^m (in the C and V band). The star's light ephemerides are plotted in Figure 9. J-K = 1.36.
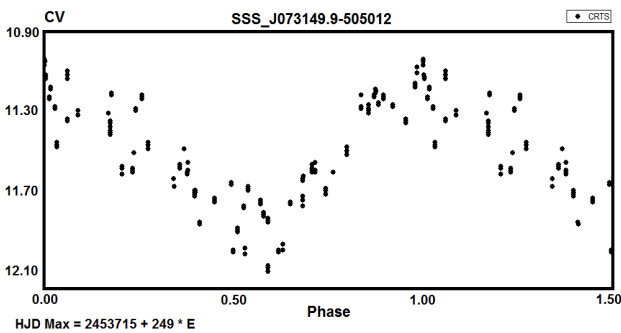
Figure 9

SSS_J200359.4-432015

The star was discovered by A.L.Galinskiy.

The UCAC4 position of the star: RA = 20^{h}03^{m}59.430^s, Dec = -43°20′15″.83.

The star's catalogue identifiers: the 2MASS identifier – J20035942-4320158; the USNO identifier – B1.0 0466-0733718; the GSC identifier – 07959-00363; the UCAC4 identifier – 234-176574.

The star's variability type: EB, the peak brightness is 13.85^m; the minimum brightness is 14.05^m; the secondary minimum brightness is 13.95^m (in the C and V band).

The star's light ephemerides are plotted in Figure 10.
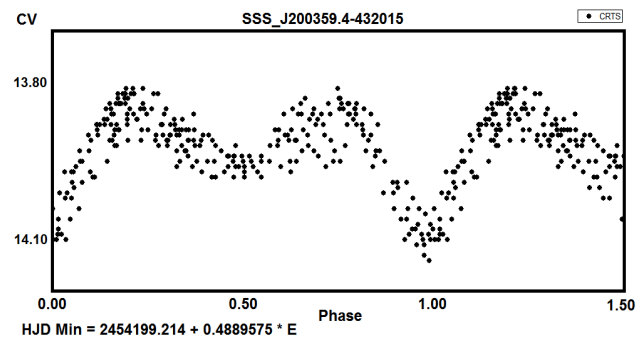
Figure 10

References

Catalina Real-time Transient Survey (A.J.Drake et al. 2009, *ApJ*, **696**, 870).

Lafler J., Kinman T. D.: 1965, *Ap. J. Suppl.*, **11**, 216.

THE QUANTITY AND QUALITY OF OBSERVATIONAL NIGHTS MONITORED WITH USING THE ASTRONOMICAL INSTRUMENTS AT THE SUBURBAN OBSERVATION STATIONS OF ASTRONOMICAL OBSERVATORY OF ODESSA NATIONAL UNIVERSITY

S.G. Kashuba[2], Yu.M. Gorbanev[2], S.M. Andrievsky[1,2], V.I. Marsakova[1], V.V. Troianskyi[1,2]

[1] Astronomy Department of I.I. Mechnikov Odessa National University
[2] Astronomical Observatory of I.I. Mechnikov Odessa National University

The Astronomical Observatory of Odessa National University named after I.I. Mechnikov is one of the four astronomical observatories which exist in classical universities.

The Observatory has a main office in the T.G. Shevchenko Park that located near historical center of Odessa. The Observatory also has several observation stations: in the Odessa suburb Mayaki and Kryzhanovka villages.

1. Statistics of the acceptable for observations nights at the Mayaki astronomical station

During about 60 years the sky patrol observations were carried out at the Mayaki astronomical station located at the distance of 40 km to the west from Odessa (geographical coordinates: φ=46.39679 deg of the northern latitude and λ=30.27274 deg of western longitude, MPC code Odessa–Mayaki is 583).

The station is a quite known place because there the third world collection of the astronomical negatives is stored. It consists of the 110000 astroplates collected in period 1909-1998 mainly with the help of 7-camera astrograph. The scanned astroplates of this collection will be the part of the Ukrainian Virtual Observatory project [1].

This station was built during the preparation to the International Geographical Year in 1957. Three telescopes were used for observations. Among them there are: 7-camera astrograph (operated during 1957-1998), Ritchey-Chretien telescope with main mirror diameter of 600 mm (RC-600, period from 2006-2012), and Odessa Multifunctional Telescope OMT-800 (the mirror diameter is 800 mm, entered into service in 2013) [2].

Having the detailed records made by observers in log book of each instrument (see left part of Fig. 2) one can get a useful information about the number of clear nights at Mayaki astronomical site. Below we present the Tables which show the result of monitoring of the number of clear nights based on the use of above mentioned three telescopes. Table 1 gives the number of clear nights as follows from the log book of 7-camera astrograph for the period from 1957 to 1998. The first record in log book was made on 19 June 1957.
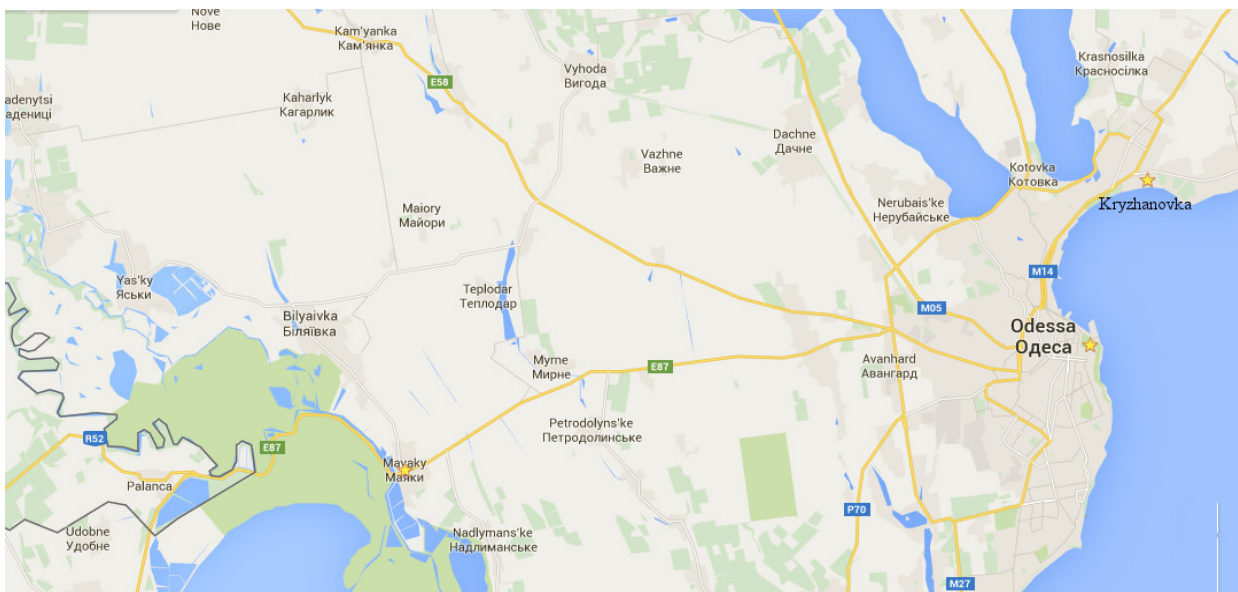
Figure 1: Observational stations of Astronomical observatory of Odessa National University at the map of Odessa region.
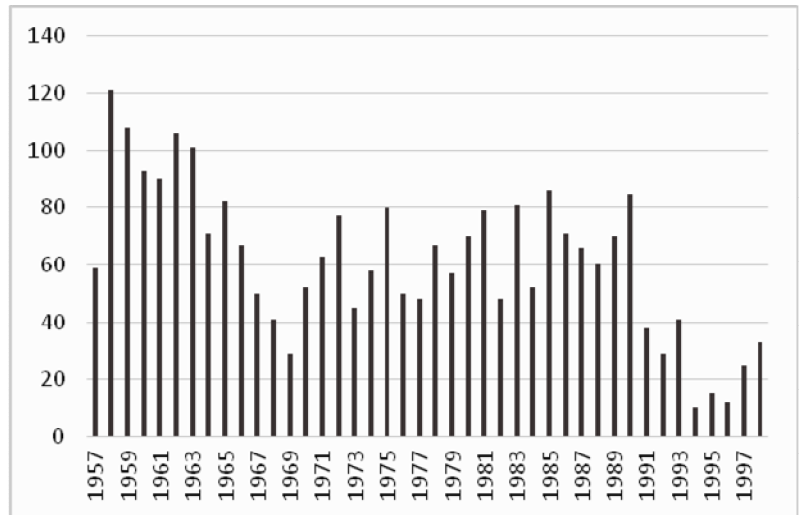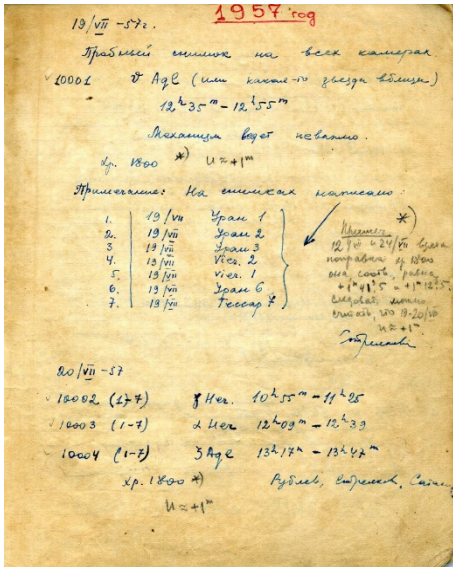
Figure 2: One page from the observational log book (left), and the number of clear nights as follows from the 7-camera astrograph data (right).
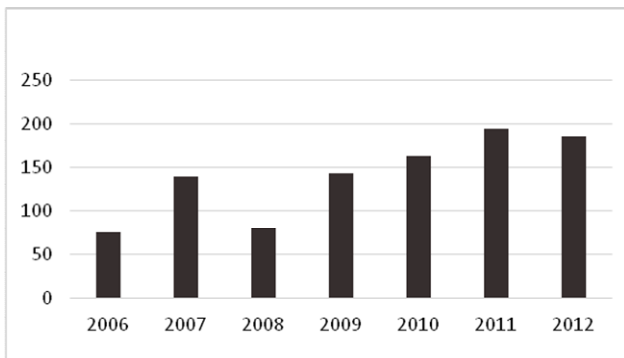
Figure 3: Number of clear nights from RC–600.

We consider the clear night as that one, when according to the log book records the observations were performed with any duration. In other words, even a part of the clear night covered by observations was considered as a fully clear night. The clear nights were not considered if a telescope spent the time for idle because of the technical reason or because of absent of observers at the telescope.

Starting from 1991 one can note the lower efficiency of 7-camera astrograph operation (see Table 1). This was not connected to a change in the weather condition. The main problem was a difficult economical situation in Ukraine at that time.

The telescope Ritchey-Chretien RC–600 started to produce significant astronomical data in April 2006. It was demounted for renovation in 2012. Statistical information based on this telescope observation is gathered in Table 2. Table 3 contains the data from OMT–800 telescope.

It should be noted that the number of clear nights counted at different telescopes and within the different observational programmes can be different from month to month. For instance, no observations were performed at the 7-camera astrograph in clear nights during the full Moon periods. At the same time the observations at RC–600 and OMT–800 were carried out even in the semi-clear nights and in the nights with the rather bad atmospheric transparency.

2. Statistics of the acceptable for observations nights at the Kryzhanovka astronomical station.

This statistics is based on observation material that was obtained with the help of meteor patrol at the Kryzhanovka astronomical station ($\varphi = 46^o$ 33' 38.6'', $\lambda = 30^o$ 48' 23.4', MPC code – A85'). The description of the meteor patrol and its technical possibilities can be found in [3].

Fig. 4 shows the histogram of the monthly number of the nights which are acceptable for observations for a period from 2003 to 2015. Initially, (in 2003), the observations were made using the Schmidt telescope. Later, the new equipment was included for the regular observations. Therefore, an initial stage of observations suffered from observational selection. For a period of 2004–2015 percentage of the clear nights, when observations were not carried out (for instance, due to a technical failure, power outage, etc), never exceeded 1%. In this sample the incomplete nights are also presented (as a rule the quality of the sky improves toward the second part of night, just after the midnight. This is a specific feature of the Kryzhanovka station, because it is located at the Black Sea shore). Presented time series shows that the shape of a distribution is repeated from year to year, although some variations are also seen.

Table 1: The number of clear nights based on 7-camera astrograph data.

Year / Month	1	2	3	4	5	6	7	8	9	10	11	12	sum
1957	-	-	-	-	-	-	9	16	15	9	5	5	59
1958	5	5	7	5	11	10	19	15	12	15	5	12	121
1959	8	8	6	7	9	13	15	10	14	11	4	3	108
1960	4	4	10	7	8	10	12	16	12	5	1	4	93
1961	2	3	7	9	6	12	11	13	11	7	5	4	90
1962	3	1	3	12	12	9	13	20	10	16	5	2	106
1963	1	4	5	6	8	11	14	16	20	8	4	4	101
1964	7	1	3	3	1	7	6	11	13	12	5	2	71
1965	-	5	3	4	7	9	12	12	14	12	2	2	82
1966	-	1	2	7	5	6	10	12	9	12	1	2	67
1967	2	-	-	2	7	3	4	15	11	6	-	-	50
1968	-	1	5	8	5	4	9	1	3	2	1	2	41
1969	1	-	-	1	2	5	4	2	5	8	1	-	29
1970	-	3	1	-	4	4	7	13	8	10	1	1	52
1971	5	-	3	3	7	4	9	12	6	11	2	1	63
1972	4	4	11	5	10	7	7	8	9	5	5	2	77
1973	3	1	7	3	2	4	7	10	5	3	-	-	45
1974	-	-	-	-	-	-	13	12	15	10	6	2	58
1975	5	2	3	4	3	8	9	15	13	10	2	6	80
1976	4	4	1	6	4	6	11	5	6	1	-	2	50
1977	3	2	3	2	-	4	7	6	7	11	-	3	48
1978	5	-	2	4	3	4	11	9	11	9	7	2	67
1979	2	2	3	1	8	7	4	8	10	4	3	5	57
1980	5	5	4	2	4	3	13	14	11	6	1	2	70
1981	3	4	9	-	9	8	9	10	11	10	2	4	79
1982	5	4	3	2	1	-	6	10	8	2	5	2	48
1983	3	3	7	5	8	7	8	12	14	8	2	4	81
1984	1	1	3	1	4	5	11	8	7	8	3	-	52
1985	7	5	5	4	8	5	11	16	11	7	7	-	86
1986	1	3	3	2	5	4	7	14	13	7	4	8	71
1987	3	5	2	3	5	6	9	12	10	6	-	5	66
1988	2	6	5	5	1	-	10	15	4	8	3	1	60
1989	2	7	5	6	2	5	10	7	5	5	9	7	70
1990	8	9	5	2	6	11	8	9	10	12	5	-	85
1991	1	1	4	-	4	3	7	3	9	5	1	-	38
1992	4	3	-	2	6	1	-	3	3	4	2	1	29
1993	4	6	3	3	1	2	7	5	6	3	-	1	41
1994	-	-	-	1	-	-	-	-	8	1	-	-	10
1995	-	1	-	-	3	3	3	3	-	2	-	-	15
1996	1	1	2	2	3	3	-	-	-	-	-	-	12
1997	-	-	2	5	2	1	1	-	5	7	2	-	25
1998	-	-	-	-	-	6	8	7	7	5	-	-	33
mean	3	3	4	3	5	5	8	10	9	7	3	2	62

Table 2. Number of clear nights from RC–600 data.

Year / Month	1	2	3	4	5	6	7	8	9	10	11	12	sum
2006	-	-	-	5	9	11	15	12	8	2	4	9	75
2007	1	1	22	12	16	17	26	18	13	9	5	-	140
2008	-	12	10	3	12	13	10	8	-	3	7	2	80
2009	2	1	-	12	17	21	22	28	19	12	8	2	144
2010	3	7	14	16	11	21	21	18	16	14	11	11	163
2011	4	6	18	12	18	20	22	27	24	19	19	9	195
2012	14	12	17	14	18	19	21	22	24	17	6	2	186
mean	3,4	5,6	11,6	10,6	14,4	17,4	19,6	19	14,9	10,9	8,6	5	140,4

Table 3. Number of clear nights from OMT–800.

Year / Month	1	2	3	4	5	6	7	8	9	10	11	12	sum
2013	3	4	8	9	12	12	18	18	8	15	11	14	132
2014	1	2	9	7	10	14	15	12	9	10	5	4	98
2015	2	7	6	11	11	13	13	11					
mean	2	4,3	7,7	9	11	13	15,3	13,7					

Fig. 5 presents a distribution of the annual number of the acceptable nights. If we ignore the nights not fully covered by observations in 2003 and 2015 years, then one can notice the following peculiarity: during the period from 2004 to 2008 the annual number of clear nights was about 100, but in 2009 it increased and reached a maximum value in 2011–2012 (226 clear nights in 2012). After it, in 2013–2014, an average value decreased up to 175. To make a forecast for the total number of clear nights in 2015, let us compare the numbers for corresponding intervals (from 1st January to 30 August): for 2014 – 116 clear nights, for 2015 – 123 nights. Thus, in 2015 the total number of clear nights should likely be comparable with that in 2014.

Fig. 6 presents a distribution of the monthly number of clear nights at the Kryzhanovka station. The season variations show that summer and autumn significantly prevail on the number of clear nights comparing with winter and spring (the factor is about 2–3).
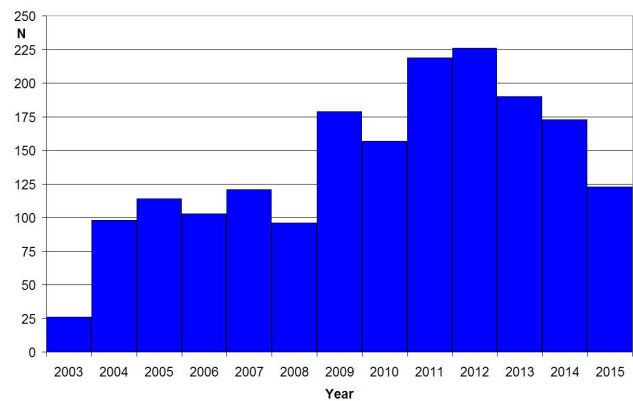
Figure 5: Annual number of acceptable nights from 2003 to 2015.
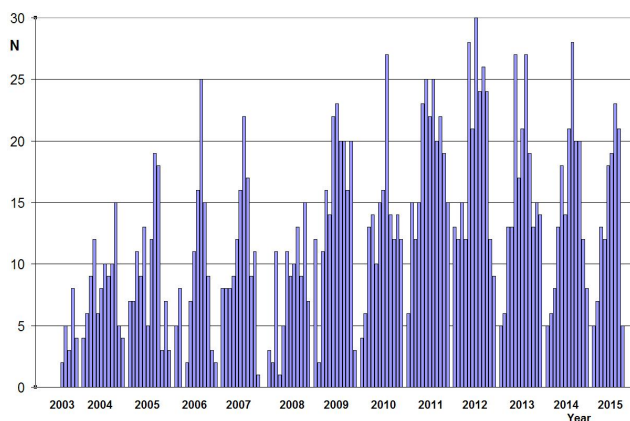
Figure 4: Monthly number of acceptable for observation nights starting from 2003 to 2015.
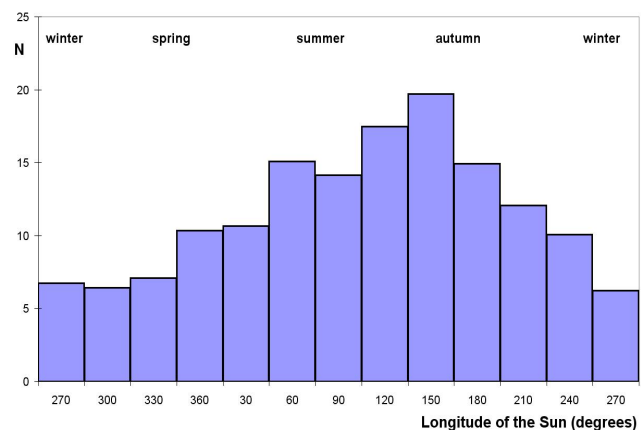
Figure 6: The mean seasonal number of clear nights for period 2003–2015.

Conclusions

It is interesting to note a quite significant decrease of the number of clear nights at the end of 60-s, as it follows from the 7-camera astrograph data (Mayaki station). It was hardly caused by the technical problems or by a non-effective work of observers. After that minimum the corresponding number of nights had more or less stable value during about 20 years.

After 2004 one can trace a tendency of an increase of a clear night number (Kryzhanovka meteor patrol data, Mayki RC–600 and OMT–800 data) up to 2011–2013. The future observations will show whether these variations really reflect the local climate and human activity changes.

References:

1. Vavilova I.B., Pakulyak L.K., Shlyapnikov A.A., Protsyuk Yu.I., Savanevich V.E., Andronov I.L. Andruk V.N., Kondrashova N.N., Baklanov A.V., Golovin A.V., Fedorov P.N., Akhmetov V.S., Isak I.I., Mazhaev A.E., Golovnya V.V., Virun N.V., Zolotukhina A.V., Kazantseva L.V., Virnina N.A., Breus V.V., Kashuba S.G., Chinarova L.L., Kudashkina L.S., Epishev V.P.: *Kinematics and Physics of Celestial Bodies*, **28(2)**, 85.
2. Andrievsky S.M., Molotov I.E., Fashchevsky N.N., Podlesnyak S.V., Zhukov V.V., Kouprianov V.V., Kashuba S.G., Kashuba V.I., Mel'nichenko V.F., Gorbanev Yu.M.: 2013, *Odessa Astron. Publ.*, **26**, 6.
3. Gorbanev Y.M.: 2009, *Odessa Astron. Publ.*, **22**, 60.

GRAVITATIONAL COLLAPSE OF STARS AND THE METHODS OF ITS OBSERVATIONS

V.G. Kryvdyk

Faculty of Physics, Taras Shevchenko National University of Kyiv,
Kyiv, Ukraine, *kryvdyk@gmail.com*

ABSTRACT. It is present a review of the models of the later stages of stellar evolution and the mechanisms of the generation of neutrinos, charged particles and electromagnetic radiation during the gravitational collapse of stars. The conclusion was made that the most likely method for the registration of the gravitational collapse of stars is the registration of the nonthermal electromagnetic radiation generating in the magnetospheres of stars during theirs gravitational collapse.

Key words: stellar evolution, radiation during collapse of stars, observation of stellar collapse, magnetospheres of collapsing stars

1. Models of stellar evolution

The evolutionary track of the star depends on its mass, chemical composition, magnetic field, as well as the presence or absence of the close neighboring stars. The evolution of single star significantly differs from the evolution of a star in the close binary system because in these systems of mass exchange is possible between components of the system. First, we consider the evolution of a single star. Theoretical study show that during the stellar evolution in core will be gradual burnout more and more heavy elements ($He^4, C^{12}, O^{16}, Ne^{20}, Si^{32}$). Depending on its mass, the star can evolve into one of the three objects such as the white dwarf, neutron star or black hole (Zeldovich and Novikov, 1977; Shapiro and Teukolsky, 1985; Arnett, 1979; Baiotti et al., 2008; Baumgarte and Shapiro, 2003; Bisnovatyi-Kogan, 2002; Ghezzi, 2005; Limongi and Chieffi, 2003; Liu et al., 2007; Shapiro, 2003; Shibata et al., 2006; Smartt, 2009; Stephens et al., 2007; Stephens et al., 2008).

White dwarfs formed because of the evolution of stars with initial masses $M < M_\odot$. (Zeldovich and Novikov, 1977; Shapiro and Teukolsky, 1985; Iben and Tutukov, 1985; Wickramasinghe et al, 2009). These objects have radius $R = 0.1R_\odot$, masses $M < 1.3M_\odot$ and average density $\rho \approx 10^7 g/m^{-3}$, the internal pressure which is supported by the degenerate electron gas (here $M_\odot$ and $R_\odot$ is the mass and radius of Sun). Magnetic field of the white dwarf reaches a magnitude $B \sim 10^8 Gs$. Calculations also show that the temperature inside the white dwarfs not exceeding the value $T \approx 8 \cdot 10^8 K$, by which begins burnout more heavy than carbon elements. Depending on the initial chemical composition of the cores, the massive white dwarfs may consist mostly with CO or ON. The formation of white dwarfs may be accompanied the ejection of a part stellar mass, which will be observed in the form of planetary nebulae.

By the evolution of more massive stars ($M > 8M_\odot$) on the final stages can be realized one with the following two scenarios. The first scenario realized when inside stars will burnout carbon $C^{12} + C^{12} \rightarrow Mg^{24}$. The later evolution can be in three ways 1) a bubbling inside the nucleus and its compression 2) the explosion and scattering of core, 3)a quick nuclear burnout, in which the future evolution of the stars in the currently is not evaluate. The second scenario will realized when the star loses mass, and by means of the pulsating processes star go to white dwarf. The even more massive stars ($8 < M/M_\odot < 25$) formed neutron stars or black holes (Cherepashchuk, 2003; Shapiro and Teukolsky, 1985; Baiotti et al., 2005; Baumgarte and Shapiro, 2003; Ghezzi, 2005; Limongi and Chieffi, 2003; Liu et al., 2007; Noble and Choptuik, 2008; Onken et al., 2004; Shapiro, 2003; Shibata, 2003; Shibata et al., 2006; Stephens et al., 2008). In cores these stars to go the gradual burnout elements ($He^4, C^{12}, O^{16}, Ne^{20}, Si^{32}$). This process continues 10^7 years and ends with the formation of the objects, the central core that consist mainly with nucleus Fe (nuclei with maximum energy on nucleon). Almost all calculations, regardless of the details, give similar results, indicating that the massive stars at the final stages of their evolution formed core with mass $M \approx 1.5M_\odot$ pressure which is supported by the degenerate neutron gas. This phenomenon is explain that due to a large temperature gradient in the core arise convectional flows, which will knead core and the tem-

perature in it become even (Arnett,1979). While the core becomes more-or-less homogeneous chemical composition. After the burnout of the silicon core the star approach to the stage of dynamic instability that leads to a gravitational collapse. It is associated with two physical processes: 1) the photodisociation of iron nuclei ($Fe + \gamma \rightarrow 13\alpha + 4n$) and the neutronization of core due to of the electrons capture by protons of kernels ($e^- + (Z, A) \rightarrow (Z-1, A) + \nu_e; e^- + p \rightarrow \nu_e + n$). Because of these processes the pressure in core fall, leading to his collapse. So begins the gravitational collapse. Calculations show that on some stages collapse go homological, i.e. its speed varies almost linearly with radius, and the instantaneous density profiles in different moments of time are similar in form, although the density grow (Goldreich and Weber, 1980). The collapse go very quickly and continues as long as the density in the heart core reaches the magnitude $\rho_n \approx 2.8.10^{14} g/m^3$. If the density in sometimes exceeds this value, the pressure in the core is growing so much that the collapse come to a stop. Inner part of core "bounces" from the Center, while its outer part continues to fall on the center. As a result, a shock wave arises, which spreads out. A characteristic energy of this shock wave is several times greater than $10^{51} Erg$. Coming out, it can change the direction of movement of a substance to the opposite, and the part of stellar matter can come off from star. We will observe this phenomenon how supernova explosion. Because of the supernovae explosion will formed neutron star, which can observed as pulsars. Neutron stars are objects with very small radius (10-20 km) and extremely strong magnetic fields ($10^{12} - 10^{14} Gs$). The core of neutron stars consists with of the degenerate neutron, which support the pressure in core. Is it always going to the stars explosion? The answer is ambiguous and is the subject of research. It all depends on whether the energy losses by the shock wave (radiation, neutrinos and the atomic nuclei dissipation) are compensated the kinetic energy inflow of the falling matter and diffusion neutrino up front shock wave (Shapiro and Teukolsky, 1985). Some authors (Henricsen et al., 1979), based on detailed hydrodynamic calculations collapse, conclude about small efficiency of shock wave in supernova explosion. Therefore, the question of whether all the stars evolve from throwing much of their mass is not clean. If a star with mass $M > 10 M_\odot$ evolves without exploding and discharge of the mass, on the final stage of evolution such a star forms a black hole. Even more massive stars (with $(25 - 30) < M/M_\odot < 150$) collapsed to black holes.

So far, we have considered the evolution model of the isolated, single stars. A somewhat different path evolving stars in close binary systems with the accretion of matter in compact objects (white dwarfs or neutron stars). In such systems the mass compact objects can significantly increase during a short time, and their evolution will be greatly different from the evolution of single objects of the same class (Baiotti et al, 2008). For example, the mass of white dwarfs in binary systems can increase as a result of accretion, and they can collapse to neutron stars (so-called induced collapse). (Cheng et al., 2009; Dermer and Atoyan, 2006; Dessart et al., 2007; Kiuchi et al., 2009; Nomoto and Kondo,1992; Nomoto and Kondo,1991: Van Paradijs J. et al., 1997; Wickramasinghe et al., 2009; Woosley and Baron, 1992; Woosley S.E. et al., 1992). Binary systems with massive stars ($M \geq (8-10) M_\odot$) on the final stages of their thermonuclear evolution will be formed neutron star or black holes. In Fig. 1 shows an evolutionary scenario of the formation neutron stars and black holes in close binary systems with massive stars (Postnov and Yungelson, 2006).
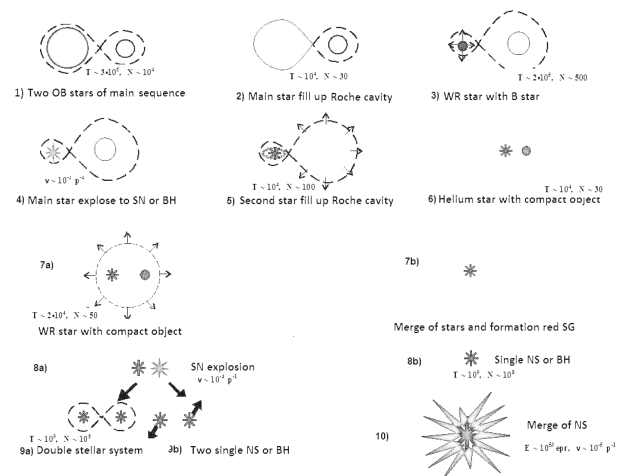
Figure 1: An evolutionary scenario of the formation neutron stars and black holes in close binary systems with massive stars (Postnov and Yungelson, 2006)

We consider in more detail the stages of evolution of stars in close binary systems.

Stages 1-2. In the initial stages two massive OB star's main sequence do not interact and are inside their cavities Roche. Due to centrifugal forces, a more massive star fills the Roche shell. Duration of this stage of evolution for the massive stars in the main sequence is a few million years. The number of stars in the Galaxy that can evolve this way, there are about 10 thousand.

Stages 2-3. After hydrogen burnout in the kernel of double-star system, the more massive stars coming off from the main sequence and it rapidly expand. When the radius approaches to cavities Roche, its mass will transfer to the second, less massive star, which is still in the main sequence. Mass transfer from the more massive star is going to as long as the majority of hydrogen the stars transfer to the less massive star, in consequence of more massive stars can rest only helium core. This core has be observed as Wolf-Rayet

stars with mass $(7-8)M_\odot$ and the intense stellar wind. The second double-star system has be observed as Be-star main sequence with fast rotation. Duration of this evolution stage is about 10^4 years.

Stages 4-5. Wolf-Rayet stars evolve quite quickly (about 2.10^4 years) due to the strong stellar wind, and at the end of their thermonuclear evolution they explode as supernovas Ib (or Ic) with the formation of the neutron star or black hole. If during the supernova explosion will be eject more than half of the original mass of the double system, then the double system can destroy, and after OB evolve as separate. If the double system is not destroyed during by supernova explosion, then the double system will consist with a young neutron star and Be star with rapid rotation. It is assumed that in this way formed the majority of double systems, observed as double Be x-ray systems. Duration of this stage collapse is determined by the duration of the burning of hydrogen in Be star and is approximately 10^4 years.

Stage 6. After that comes the so-called stage of evolution in the mutual shell, when Be star loses mass as a result of a powerful stellar wind, filling his matter of all the double system, exposing the helium core and the forming Wolf-Rayet stars. The system consists with two compact objects- neutron stars and Wolf-Raiet star, on which to occur the accretion of matter shell.

Stages 7-10. Further, the dual system can evolve according to two scenarios: a) or b). Scenario a). If in consesuquece of the mass accretion the Wolf-Raeyt star core rise to quantities, sufficient for the collapse and explosion of the star as a supernova Ib, then the dual system will consist with two relativistic objects (neutron stars or black holes). Neutron star can also collapsed to black holes, if its mass will increase because of the accretion to a mass of Chandrasekhara. Thus formed the system of two relativistic stars. Because of the merger of stars, which will be accompanied the intense gravity and electromagnetic radiation, can form a black hole (scenario 7a-10). Second scenario b) for the evolution of the double system will be realized when Wolf-Raiet star not exploding as the supernovae, and merge of the components of the dual system is in the earlier stages of evolution. As a result of this merger arise red supergggant with core in form a neutron star or black hole (objects Torn-Zitkova). When the supergigant losed its shell due to accretion, on the site of a double system is formed a single neutron star or black star.

Stars with the low mass in the compact binary systems evolv in different way (Abdikamalov et al, 2009; Baiotti et al., 2008). If the initial system consists with the two stars of the main sequence, the mass of which does not exceed $(2-2,5)M_\odot$, then by the evolution of a more massive star fills the entire shell Roche, and a helium white dwarf will form. The stars with mass $M > (2-2,5)M_\odot$ form the system with CO white dwarf. As a result of the accretion, mass of white dwarf can grow to the value, when it can collapsed and explode as a supernova (Fedorova et al., 2004; Hachisu and Kato, 2001; Han and Podsiadlowski, 2006; Han and Podsiadlowski, 2004; Lesaffre et al., 2006; Li and Heuvel, 1997; Yungelson and Livio, 1998). Thus, on the final stages of the stellar evolution in a binary stars system will form the various configurations of close binary systems, such as systems with white dwarf, neutron stars and black holes. These objects have a small size, a large density and the nonstationary strong magnetic fields. By such conditions, charged particles will accelerate, and they will generate of the electromagnetic radiation. Therefore, such systems are sources of the powerful electromagnetic radiation and cosmic rays.

2. Generation of high-energy particles in the magnetosphere of collapsing stars

In this section, we consider the mechanisms of the generation of high-energy particles in magnetosphere of collapsing stars. First in the magnetosphere will accelerate the initial protons and electrons due to the interaction with the magnetic field. These particles will lose its energy on the ionization and radiation. Interacting between themselves and the fields, these particles in later on will be generated secondary particles, such as electrons, protons, neutrons, mesons, neutrinos, antineutrinos and gamma photons. Because of these multiple interactions will be generated particles with which to consist the magnetosphere of collapsing star on the later stages of collapse. There are many the mechanisms of the particles generation during of stellar collapse (Leng, 1984; Bahcall and Wolf, 1965; Braaten and Segel, 1993; Bruenn, 1985; Canuto et al., 1970; Chiu, 1961; Chiu and Morrison, 1960; Chiu and Stabler, 1961; Dicus, 1972; Friman and Maxwell, 1979; Hansen, 1968; Itoh et al., 1989; Koers and Wijers, 2005; Lattimer et. al., 1991; Munakata et al., 1985; Qian and Woosley, 1996; Ratkovic S. at al., 2003; Reynoso et al., 2006; Yakovlev et al., 2001).

In author articles (Kryvdyk, 2014a; Kryvdyk, 2014b) was considered possible mechanisms of generation of high-energy particles and the nonthermal electromagnetic radiation in a magnetosphere of collapsing star, namely:

1. The formation of pi-mesons, mu-mesons, electrons, neutrinos and positrons by nuclear interactions in a magnetosphere of collapsing star.

2. The formation of electron-positron pair by interaction of gamma rays with nuclear.

3. The formation of electron-positron pair by a collision of charged particles.

4. The formation of electron-positron pair by a colli-

sion the two photons.

5. The formation of mu-mesons pairs by interaction of gamma rays with nuclear.

6. The formation of electron impact by a collision of charged particles.

7. The formation of neutrino in the magnetosphere of collapsing stars.

Because of these processes in the magnetosphere of collapsing star will generate neutrinos, photons, neutrons and charged particles, which, by interacting with the magnetospheric magnetic field, will in turn generate the nonthermal electromagnetic radiation.

3. Electromagnetic radiation of stars on the final stages of their evolution

In the previous sections, we have reviewed models of the evolution of the various types stars and the generation of particles and photons in theirs magnetospheres during the gravitational collapse. As you can see, stars undergo several stages of evolution, depending on their mass, chemical composition and the presence or absence of a close companion. One of these stages is the gravitational collapse of star, which begins when star loses its energy reserves and begin compress under their gravitational field. Depending on the mass of the core, star can collapse to one with the three objects, such as the white dwarf, neutron star or black hole. As follows from the theoretical calculations, during the gravitational collapse of stars the gravitational and electromagnetic radiation will generate. (Kryvdyk, 1998; Kryvdyk, 2008; Kryvdyk, 2009; Kryvdyk, 2010; Chau, and Zhang, 1992; Gunningam et al., 1978; Gunningam et al., 1979; Gunningam et al., 1980; Hanami, 1997; Henricsen et al., 1979; Mac-Fadyen and Woosley, 1999;, Mitsuda et al., 2005; Moncrief, 1980; Morley and Schmidt, 2002; Paranjape and Padmanabhan, 2009; Ruffini et al., 2005a; Ruffini et al, 2005b; Ruffini et al., 2007; Ruffini et al., 2003; Shibata and Taniguchi, 2006; Uzdensky, 2007), (Kryvdyk, 2014a; Kryvdyk, 2014b; Anchordoqui, 2009; Becker and Biermann, 2009; Blinnikov et al., 1988; Dutta et al., 2000a; Dutta et al., 2000b; Lu and Qian, 2007; Nakazato et al., 2007; Ryazhskaya, 2006; Vigorito et al., 2008; Yu et al., 2008).

The gravitational radiation, theoretically predictable by the collapse of stars, currently not registered. As regards the registration of electromagnetic radiation, the numerical calculations indicate that the collapsing star can be sources of the short giant x-ray and gamma-ray bursts observed on space-based telescopes. The only one case of the registration of neutrino was detected from supernovae SN 1978A (Alekseev et al., 1987; Davydkin et al., 1987; Bionta et al., 1987; Hirata et al., 1987).

In articles (Gunningam et al., 1978; Gunningam et al., 1979; Gunningam et al., 1980; Moncrief, 1980), based on the numerical calculation of wave equations, was obtained spectra and energy for gravitational and electromagnetic radiation, generating during the relativistic collapse of stars with magnetic fields. As follows from these calculations, the radiation does not depend on the dynamics of collapse inside star. The dipole radiation from the collapsing uniform spheroid with a constant rotation was calculated in work (Henricsen et al., 1979). It is shown, that during the collapse of the object with a mass of $1.4 M_\odot$, the initial density of $10^8 g/cm^{-3}$ and a magnetic field $10^8 Gs$ to black hole energy dipole radiation is about $2.4 \cdot 10^{40} Erg/sec$. However, the frequency of this radiation 1 kHz is wery low, and it can not be registered by means of modern telescopes. In paper (Ruffert and Janka, 1999) was calculated the formation of the accretional torus by merge of the two neutron stars, as a results of a compact remnant with mass $3 M_\odot$ formed, which then collapses into a black hole. The authors find that after a merge of neutron stars will form torus, and the neutrino was radiate with the total energy $10^{53} Erg/sec$. The contribution of radiation energy from the annihilation of neutrino-antineutrino in torus is $(3-5) 10^{50} Erg/sec$ with the duration radiation $0.02 - 0.1 sec$. It is show that neutrino-antineutrino annihilation by the accretion on black hole, which is formed after a merger of two neutron stars, could provide enough energy for low short periodical gamma-ray flares. In paper (MacFadyen et al., 2001) was investigated the evolution of helium stars with a mass $M > M_\odot$, in which by the collapse of an iron core are not formed enough of a powerful shock wave that can come out, but instead forms a black hole. The author's investigated the formation of the accretion disk and strong relativistic jets in polar regions. When these jets comes out through the surface of the star, the relativistic flows may experience. These flows have energy about $10^{51} Erg/sec$. By this the gamma-ray bursts with a duration less than a few seconds can generated. The generation of electromagnetic pulse during the stellar gravitational collapse was calculated in the article (Morley and Schmidt, 2002) as for star with the average magnitude core, in which to take place hydrodynamical rebound, and for star with massive core, which collapses to black hole. The authors show, that the two types of stars should exist, separating by the maximum permissible masses, those that collapse as a single star (with minimal dynamic mass) and those that collapse in binary systems and where possible accretion masses (with static mass of neutron stars). In article was calculated the energy of electromagnetic radiation for stellar objects with the rebound in core, which form a stable neutron star, and massive stellar objects that collapse directly into a black hole. The maximum of this radiation falls on very low frequency (wavelength is about 2 km). Such low frequency radiation will be absorbed in Earth at-

mosphere, and it not can be observed on radio telescopes. Evolution of the electromagnetic field of magnetic stars, which collapse to black holes, was resolved in the general theory of gravity in the article (Baumgarte and Shapiro, 2003). Author assumed that during collapse the mass of star has infinite conductivity and the magnetic field is dipolar. Evolution of the magnetic and electric fields was determined analytically for the matter inside the stars and numerically for external vacuum. Research has shown that during the collapse of the longitudinal magnetic field will transform into transverse electromagnetic waves. Part of the electromagnetic radiation is captured by black hole, and the rest is propagated outside on the large distance. Theoretical research with the purpose to explain gamma-ray bursts was analyzed in the works (Ruffini et al., 2005a; Ruffini et al., 2005b; Ruffini et al., 2007). Authors made conclusions that: (1) only the basic structure of gamma-ray burst is the unchanging characteristic for gamma-ray bursts and their afterglow; (2) the long periodical gamma-ray bursts are just the peaks of afterglow, and their variations can be explained because of the interstellar medium heterogeneity; (3) short bursts can be identified as the typical gamma-ray bursts, therefore the key information of the relativistic effects and the vacuum polarization is encoded in their spectrum and in the intensity variations with time. These gamma-ray bursts radiate because of processes of the vacuum polarization in dyosphere of black holes with the formation of optically thin electron-positron plasma, which is self-acceleration. Theoretical prediction of the electromagnetic radiation signal by the gravitational collapse of star core to black hole was examined in the paper (Ruffini et al., 2003). Final phase of gravitational collapse was investigated, which lead to the formation of black holes with the under critical electromagnetic field and the formation of the outgoing pulse initially fine e + e photon plasma. This impulse reaches the transparency for the Lorenz factor $102 - 104$. The authors find the clear signs of the formation of the electromagnetic signal during the gravitational collapse. The collapse of neutron stars to black holes in binary systems for the explainion of short gamma-ray busts are considered in the paper (Dermer and Atoyan, 2006). It is found, that the accretion of matter with mass $(0.1 - 1)M_\odot$ through Roche cavity on the neutron star from its companion or as a result of the merger of neutron stars with a white dwarf in a double system with a small mass will be sufficient to exceed the critical mass of neutron stars, and cause it to collapse to black holes, which causes the generation of short gamma-ray flashes. A two-dimensional axial-symmetric magnetohydrodynamical model of star collapse with a mass of $40M_\odot$ was calculated in work (Fujimoto et al., 2006) for the explanation of collapsar as a source of gamma-ray bursts. Author studied the formation of the accretionary disc arousing black

holes and the formation of jets near it. In the works (Uzdensky and MacFadyen, 2006; Uzdensky and MacFadyen, 2007) was proposed a magnetic mechanism for the collimating explosion of massive stars, which concerns the long periodical gamma-ray and x-ray bursts and asymmetric collapse the supernovae core. In this model the core of massive stars, that revolve, collapse to collapsar with black hole with the accretionary disk or millisecond magnetar. The collapse of gipermassive neutron stars as the source of short gamma-ray bursts was considered in the article (Shibata M. et al., 2005). These stars form after the merge of neutron star in double system. The authors find that gipermassive neutron star undergoes a "delayed" collapse to black holes with the rotation because of the transfer of angular moment due to magnetic braking and magneto-rotational instability. As a result, a black hole arise, surrounded a massive hot torus with collimated magnetic field. Torus fall on black hole with the quasi-constant speed $10M_\odot/s$. Lifetime this torus is 10 Ms. The temperature in torus reaches $10^{12}K$, which leads to the intense neutrino-antineutrino generation. This scenario of collapse is attractive for an explanation of the generation low-period giant gamma-ray bursts and accompanying their gravitational waves and neutrinos. In work (Dessart et al, 2007) made the two dimensional magnetohydrodynamical modeling for the accretion-induced collapse of a white dwarf with a mass $1.92M_\odot$ with rapid rotation. Authors identified the role of MHD process after the formation of the protoneutron star with the milisecond period, and they found that the magnetic tension could lead to a powerful blast with a energy in several Bethe and mass injection $0.1M_\odot$. Core will rotate after the rebound, and the energy of rotation that is extracted from core, turns into magnetic energy, which generates a strong magnetic collimated wind.

As you can see, for the all models of the collapse of stars is common the generation of the electromagnetic radiation pulse and the formation of relativistic jets. There are many models of the relativistic jets formation by the stellar collapse (Aloy et al., 2000; Beskin et al., 2008; Blandford and Payne 1982; Bucciantini et al., 2008; Couch et al., 2009; Fendt, 2009; Kato et al., 2004; Koide et al., 1998; Komissarov and Barkov, 2007; Kryvdyk, 2008; Kryvdyk, 2010; MacFadyen et al., 2001; Matsakos et al., 2008; Meliani et al., 2006; Mizuno, et al., 2004; Ono et al., 2009; Takiwaki et al., 2009; Uzdensky and MacFadyen, 2007; Zhang et al., 2003).

Blandford and Znajek (1977) considered the model in which the relativistic particles acceleration and jets formation going on at great distances from the black hole in a magnetized accretional disk of a rotating black hole. Model formation of relativistic jets in the accretion plasma disk, surrounding black hole, was considered in work (Koide et al.,1998). Jets arise by the in-

jection plasma with disk, bordering upon to the black hole. These jets are the two-level structure, which consists with the fast gas jets inside arising as a result of the pressure gradient, and the slow jets in other parts of the disk, that are associated with the poloidal magnetic field of disk. The jets are formed as a result of the strong increase of pressure and the shock wave formation in the disk through the fast accretion streams.

The formation of relativistic jets during the evolution of helium stars with mass $M > 10 M_\odot$, where the collapse of the iron core does not generate strong shock waves that can come out, and instead formed black hole, is considered in work (MacFadyen and Woosley, 1999). In this model relativistic jets are formed as result of the accretion in the polar regions and go outside. In article (MacFadyen et al., 2001) were analyzed MHD processes and the formation of supernova stars and high-energy transient during the collapse of massive stars with rotation. Relativistic jets in this model arise by mass accretion from the disk. The total relativistic 2.5- dimensional MHD model of the gravitational collapse of a massive magnetized star with the rotation is calculate in article (Mizuno et al., 2004). Simulation results show that during collapse formed a disk structures and the jets generated, wich formed during the rebound the shock wave from the core. These jets are accelerated by means of the magnetic pressure and centrifugal force.

4. Electromagnetic radiation from magnetospheres of collapsing stars

In view of the observations of the most interesting is the high-frequency radiation, which generate in a magnetosphere of collapsing star and it little is absorbed in the areas of their generation and in interstellar medium. Such radiation can reach the Earth and can be registered with modern telescopes in various ranges of electromagnetic radiation.

In author articles (Kryvdyk, 1998; Kryvdyk, 1999; Kryvdyk, 2009; Kryvdyk, 2010, Kryvdyk, 2014a; Kryvdyk, 2014b) was studied in detail the processes of charged particles acceleration in a magnetosphere of collapsing star, and the nonthermal radiation from these particles in a magnetic field was calculated. In these articles were calculated the synchrotron radiation flows from charged particles in a external magnetic field collapsing stars, that grows during the collapse and accelerate these particles by means of the betatron mechanism. Author considered the physical conditions and the charged particles dynamics in the magnetosphere, and the Stokes parameters calculated that characterize the radiation of these particles in the magnetosphere. It is shown that in a magnetosphere of collapsing star will be generated charged particles (protons, electrons, positrons, pi-mesons), neutrons and neutrinos. Neu-

trons and neutrinos do not interact with the magnetic fields, therefore they will be free to go with the magnetosphere, bringing a significant portion of energy. As a result, the star will cools.

Charged particles (protons, electrons and positrons), moving in the variable magnetic field, will generate a powerful impulse of the nonthermal electromagnetic radiation in a wide range of frequencies, from gamma to radio frequencies. In Table 1 are give the numerical calculations of the electromagnetic radiation flow in the magnetosphere of collapsing stars, generating by mowing of charged particles with a power spectrum in magnetic fields. In Table 2 gives the value of the flow of radiation at different frequencies for $R_* = 1000$ and $I_{\nu_0} = 10^{-25} W/m^2 Gz$. The value $\nu/\nu_0 = 1$ is chosen for frequency $\nu_0 = 10^{10} Gz$. As follows from calculation, the radiation flow reaches the largest values at low frequencies and decrease with a frequency by law $I_{\nu P} \sim \nu^{(1-\gamma)/2}$. For a power particles spectrum with $\gamma \approx 2.5$ the radiation flow depend from frequency as $I_{\nu P} \sim \nu^{-0,7}$. This is a typical frequency dependence for the cosmic nonthermal electromagnetic radiation of particles in the strong magnetic fields. As you can see, during the stellar collapse will generated a powerful radiation flow that can be registered by using the gamma and x-ray satellites (Kryvdyk, 2010). Such observations are extremely important, because so far we do not have the astrophysical observations, which would really confirm such the stage of evolution of stars as their gravitational collapse. Figure 2 shows the ratio between the flow of radiation $I_{\nu P}$ at some point collapse of star with radius R and the initial electromagnetic radiation flow $I_{\nu P0}$ stars from the original R_0. It is evident that the radiation flow increases during the collapse in the hundreds of millions of times in comparison with the original flow.

5. Conclusion

If from a theoretical point of view the stage of gravitational collapse (compression) for more than half a century been extremely detailed, then from the observational point of view we still not have the direct astrophysical data that would confirm this stage of the evolution of stars. Indeed, white dwarfs and neutron stars we observe how objects that were formed after the gravitational collapse, i.e. after compression. A supernova stars observed because of the collapse of the core of a star when it is already compress to nuclear density. Therefore these events are events after the fact, i.e. that occurred as a result of compression, and they are not the direct observational evidence of gravitational compression.

In order to confirm the existence of a gravitational collapse with the help of astrophysical observations, we must register the signals in the short period of time,
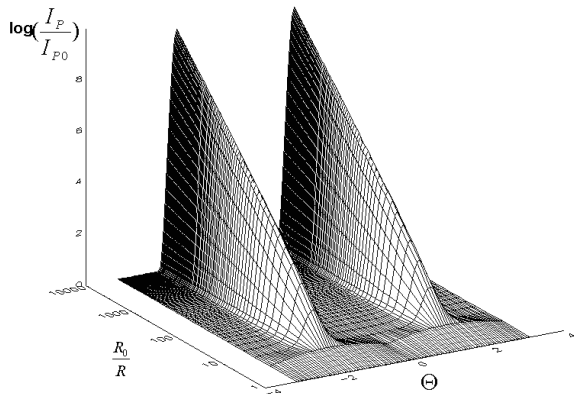
Figure 2: Pulses of nonthermal radiation from the magnetosphere of collapsing star with a power distribution of particles. Here I_{P0} is a initial radiation flow (when radius star is R_0), I_P is the radiation flow in a particular moment of collapse (when the radius of the star decreases to value R). (Kryvdyk, 2010)

Table 1: Flows radiation $I_{\nu P}(W/m^2 Hz$ for different $R_* = R/R_0$ and various index γ of a particles power spectrum $N(E) \sim E^{-\gamma}$ (Kryvdyk V, 1999)

γ	2.4	2.6	2.8
R_*	$I_{\nu P}$		
100	$2.57 \cdot 10^{-22}$	$2.14 \cdot 10^{-20}$	$1.81 \cdot 10^{-20}$
200	$1.37 \cdot 10^{-21}$	$1.65 \cdot 10^{-20}$	$2.00 \cdot 10^{-19}$
300	$3.72 \cdot 10^{-21}$	$5.52 \cdot 10^{-20}$	$8.31 \cdot 10^{-19}$
400	$7.57 \cdot 10^{-21}$	$1.31 \cdot 10^{-20}$	$2.29 \cdot 10^{-18}$
500	$1.32 \cdot 10^{-20}$	$2.56 \cdot 10^{-20}$	$5.05 \cdot 10^{-18}$
600	$2.08 \cdot 10^{-20}$	$4.45 \cdot 10^{-19}$	$9.66 \cdot 10^{-18}$
700	$3.05 \cdot 10^{-20}$	$7.09 \cdot 10^{-19}$	$1.67 \cdot 10^{-17}$
800	$4.27 \cdot 10^{-20}$	$1.06 \cdot 10^{-18}$	$2.69 \cdot 10^{-17}$
900	$5.74 \cdot 10^{-20}$	$1.52 \cdot 10^{-18}$	$4.09 \cdot 10^{-17}$
1000	$7.48 \cdot 10^{-20}$	$2.10 \cdot 10^{-18}$	$5.96 \cdot 10^{-17}$

Table 2: Values $I_{\nu P}$ for different frequence ν/ν_0 and different index γ for a particles with a power spectrum $N(E) \sim E^{-\gamma}$. Here $\nu_0 = 10^{10} Gz$. (Kryvdyk, 1999).

γ	2.4	2.6	2.8
$\log(\nu/\nu_0)$	$I_{\nu P}$		
-4	$4.72 \cdot 10^{-20}$	$3.32 \cdot 10^{-20}$	$2.37 \cdot 10^{-20}$
-2	$1.88 \cdot 10^{-20}$	$8.35 \cdot 10^{-20}$	$3.76 \cdot 10^{-20}$
0	$7.48 \cdot 10^{-20}$	$2.10 \cdot 10^{-20}$	$5.96 \cdot 10^{-20}$
2	$2.98 \cdot 10^{-20}$	$5.27 \cdot 10^{-20}$	$9.45 \cdot 10^{-20}$
4	$1.19 \cdot 10^{-20}$	$1.32 \cdot 10^{-20}$	$1.50 \cdot 10^{-20}$
6	$4.72 \cdot 10^{-20}$	$3.32 \cdot 10^{-20}$	$2.37 \cdot 10^{-20}$
8	$1.88 \cdot 10^{-20}$	$8.35 \cdot 10^{-20}$	$3.76 \cdot 10^{-20}$
10	$7.48 \cdot 10^{-20}$	$2.10 \cdot 10^{-20}$	$5.96 \cdot 10^{-20}$
12	$2.98 \cdot 10^{-20}$	$5.27 \cdot 10^{-20}$	$9.45 \cdot 10^{-20}$
14	$1.19 \cdot 10^{-20}$	$1.32 \cdot 10^{-20}$	$1.50 \cdot 10^{-20}$

when the star compress by its own gravitational field. These signals can be: 1) gravitational waves that will generate by collapse; 2) neutrino; 3) electromagnetic radiation that will generate by collapse. Registration of gravitational waves today is quite problematic issue, because this method of observation of gravitational collapse is the question of the future. Registration of neutrinos flow from space with sufficient space and time accuracy is also a problem in the future. Therefore the most likely and reliable method of the observation of the stars on the stage of its gravitational compression gives us the observation of electromagnetic radiation, that is generated during its gravitational collapse.

As we can see from Fig.1 and Table 1 and Table 2, during the collapse in the magnetosphere of collapsing stars a powerful pulses the nonthermal electromagnetic radiation will generate with amplitudes, enough to register on the gamma-ray and x-ray space telescopes, as well as ground-based radiotelescope. Such impulses to be found primarily among the single radio, gamma and x-ray bursts of an unknown nature, which are not associated with the regular astrophysical objects. Such bursts will register only once and not repeated. They can be observed as well as precursor of supernova stars, when the supernova precursor star compressed, and then explode as a supernova. If collapsing star not explodes as supernova and form a black hole, then we will observe the damping impulse, which disappears when the radius of the star becomes less than the Schwarzschild radius.

Thus, the existence of gravitational compression (collapse) stars still not confirmed by direct astrophysical observations. Therefore, an extremely important task in astrophysics is the development of the astrophysical observation, which direct confirm the stage of gravitational compression. Without this, the gravitational collapse will be the only subject of theoretical research, not confirmed astrophysical observations.

References

Abdikamalov E.B. et al.: 2009, *MNRAS,* **392**, 52.

Alekseev E.M. et al.: 1987, *Pisma JETP,* **45**, 461.

Aloy M.A. et al.: 2000, *Ap. J.L.* **531**, 119.

Anchordoqui L.A.: 2009, *MNRAS,* **396**, 1629.

Arnett W.D.: 1979, *"Sources of gravitational radiation"*. *Ed. Smarr. Gambridge.*

Bahcall J.N., Wolf R.A.: 1965, *Phys. Rev. B,* **140**, 1452.

Baiotti L. et al.: 2008, *Phys. Rev. D,* **78**, id. 084033.

Baiotti L. et al.: 2005, *Phys. Rev. D,* **71**, id. 024035.

Baumgarte T.W., Shapiro S.L.: 2003, *Ap. J.,* **585**, 930.

Becker J.K., Biermann P.L.: 2009, *Astropart. Phys.,* **31**, 138.

Beskin G. et al.: 2008, *Adv. Space Res.,* **42**, 523.

Bionta R.M. et al.: 1987, *Phys. Rev. Lett.,* **58**, 1494.

Bisnovatyi-Kogan G.S.: 2002, *Stellar Physics,* Berlin, Springer.

Blandford R.D., Znajek R.L.: 1977, *MNRAS*, **179**, 433.

Blandford R.D., Payne D.G.: 1982, *MNRAS,* **199**, 883.

Blinnikov S.I., Imshennik V.S., Nadyozhin D.K.: 1988, *Astropys. Space Sci.,* **150**, 273.

Braaten E., Segel D.: 1993, *Phys. Rev. D,* **48**, 1478.

Bruenn S.W.: 1985, *Ap. J. Sup. Ser.,* **58**, 771.

Bucciantini N., et al.: 2008, *MNRAS,* **383**, L25.

Canuto V., et al.: 1970, *Phys. Rev. D,* **2**, 281.

Chau, W.Y.; Zhang, J.L.: 1992, *Astrophys. Space Sci.,* **190**, 131.

Cheng K.S., et al.: 2009, *Journ. Cosmol. Astropart. Phys.,* **9**, 7.

Cherepashchuk A.M.: 2003, *Physics Uspekchi,* **46**, 335.

Chiu H.Y.:1961, *Phys. Rev.,* **123**, 1040.

Chiu H.Y., Morrison P.: 1960, *Phys. Rev. Lett.,* **5**, 573.

Chiu H.Y., Stabler R.C.: 1961, *Phys. Rev.,* **122**, 1317.

Couch S.M., Wheeler J.C., Milosavljevic M.: 2009, *Ap. J.,* **696**, 953.

Davydkin V.D., et al.: 1987, *Pisma JETP,* **45**, 464.

Dermer C.D., Atoyan A.: 2006, *Ap. J.,* **643**, L13.

Dessart L. et al.: 2007, *Ap. J.,* **669**, 585.

Dicus D.A.: 1972, *Phys. Rev. D,* **6**, 941.

Dutta G. et al.: 2000a, *Phys. Rev. D,* **61**, id. 013009.

Dutta G. et al.: 2000b, *Phys. Rev. D,* **62**, id.093014.

Fedorova A.V., Tutukov A.V., Yungelson L.R.: 2004, *Astron. Lett.,* **30**, 73.

Fendt C.: 2009,*Ap.J.,* **692**, 346.

Friman B.L., Maxwell O.V.: 1979, *Ap. J.,* **232**, 541.

Fujimoto S. et al.: 2006, *Ap. J.,* **644**, 1040.

Ghezzi C.R.: 2005, *Phys. Rev. D,* **72**, id. 104017.

Goldreich P., Weber S.: 1980, *Ap. J.,* **238**, 991.

Gunningam C.T., Price R.H., Moncrief V.: 1978, *Ap. J.,* **224**, 643.

Gunningam C.T., Price R.H., Moncrief V.: 1979, *Ap. J.,* **230**, 870.

Gunningam C.T., Price R.H., Moncrief V.: 1980, *Ap. J.,* **236**, 674.

Hachisu I., Kato M.: 2001, *Ap. J.,* **558**, 323.

Han Z., Podsiadlowski P.: 2006, *MNRAS,* **368**, 1095.

Han Z., Podsiadlowski P.: 2004, *MNRAS,* **350**, 1301.

Hanami. H.: 1997, *Ap. J.,* **491**, 687.

Hansen C.J. 1968, *Astrophys. Space Science,* **1**, 499.

Henricsen R.N., Chau W.Y., Chau K.L.: 1979, *Ap. J.,* **227**, 1013.

Hirata K. et al.: 1987, *Phys. Rev. Lett.,* **58**, 1490.

Iben Jr.I., Tutukov A.V.: 1985, *Ap. J. Sup. Ser.,* **58**, 661.

Itoh N. et al.: 1989, *Ap. J.,* **339**, 354.

Kato Y., Hayashi M.R., Matsumoto R.: 2004, *Ap. J.,* **600**, 338.

Kiuchi K. et al.: 2009, *Phys. Rev. D,* **80**, id. 064037.

Koers H.B.J., Wijers R.A.M.J.: 2005, *MNRAS,* **364**, 934.

Koide S., Shibata K., Kudoh T.: 1998, *Ap. J. L.,* **495**, L63.

Komissarov S.S., Barkov M.V.: 2007, *MNRAS,* **382**, 1029.

Kryvdyk V.: 2008, *Adv. Spac. Res.,* **42**, 533.

Kryvdyk V.: 1998, *Kinematica Fiz. Nebesn. Tel,* **14**, 475.

Kryvdyk V.: 2010, *Kinem. Phys. Cel. Bodies,* **25**, 277.

Kryvdyk V.: 1999, *MNRAS,* **309**, 593.

Kryvdyk V.: 2009, *Kinematica Fiz. Nebesn. Tel,* **25**, 415.

Kryvdyk V.: 2014a, *Europ. Pys. J. C. S.,* **70**, 56.

Kryvdyk V.: 2014b, *Odessa Astron. Publ.,* **27/2**, 119.

Lattimer J.M. et. al.: 1991, *Phys. Rev. Let.,* **66**, 2701.

Leng K.R.: 1984, *Astrophysical formulae, Mir, Moscow.*

Lesaffre P. et al.: 2006, *MNRAS,* **368**, 187.

Li X.-D., van den Heuvel P.J.: 1997, *Astron. Astrophys.,* **322**, L9.

Limongi M., Chieffi A.: 2003, *Ap. J.,* **592**, 404.

Liu Y.T., Shapiro S.L., Stephens B.C.: 2007, *Phys. Rev. D,* **76**, id. 084017.

Lu Y, Qian Y.-Z.: 2007, *Phys. Rev. D,* **76**, id. 103002.

MacFadyen A.I., Woosley S.E.: 1999, *Ap. J.,* **524**, 262.

MacFadyen A.I., Woosley S.E., Heger A.: 2001, *Ap. J.,* **550**, 410.

Matsakos T. et al.: 2008, *Astron. Astrophys.,* **477**, 521.

Meliani Z.V. et al.: 2006, *Astron. Astrophys.,* **447**, 797.

Mitsuda E., Yoshino H., Tomimatsu A.: 2005, *Phys. Rev. D,* **71**, id. 084033.

Mizuno Y., et al.: 2004, *Ap. J.,* **606**, 395.

Moncrief V.: 1980, *Ap. J.,* **238**, 333.

Morley P.D., Schmidt I.: 2002, *Astron. Astrophys.,* **384**, 899.

Munakata H., Kohyama Y., Itoh N., 1985, *Ap. J.,* **296**, 197.

Nakazato K., Sumiyoshi K., Yamada S.: 2007, *Ap. J.,* **666**, 1140.

Noble S. C., Choptuik M. W.: 2008, *Phys. Rev. D.,* **78**, id. 064059.

Nomoto K., Kondo Y.: 1992, *NATO ASI Ser. C.,* **377**, 189.

Nomoto K., Kondo Y.: 1991, *Ap. J. L.,* **367**, L19.

Onken C.A. et al.: 2004, *Ap. J.,* **615**, 645.

Ono M. et al.: 2009, *Progr. Theor. Phys.,* **122**, 755.

Paranjape A., Padmanabhan T.: 2009, *Phys. Rev. D.,* **80**, id. 044011.

Postnov K.A. Yungelson L.R.: 2006, *Living Rev. Relativity,* **9**, 1.

Qian Y.Z., Woosley S.E.: 1996, *Ap. J,* **471**, 331.

Ratkovic S., Dutta S.I., Prakash M.: 2003, *Phys. Rev. D.,* **67**, id. 123002.

Reynoso M.M., Romero G.E., Sampayo O.A.: 2006, *Astron. Astrophys.,* **454**, 11.

Ruffert M., Janka H.-Th.: 1999, *Astron. Astrophys.,* **344**—, 573.

Ruffini R. et al: 2003, *Amer. Inst. Phys. Conf. Proc.,* **668**, 16.

Ruffini R. et al.: 2005a, *Amer. Inst. Phys. Conf. Proc.,* **782**, 42.

Ruffini R. et al.: 2007, *Amer. Inst. Phys. Conf. Proc.,* **910**, 55.

Ruffini R. et al: 2005b, *Intern. J. Modern Phys. D.,* **14**, 131.

Ryazhskaya O. G.: 2006, *Physics Uspekhi,* **49**, 1017.

Shapiro S.L.: 2003, *Astron. Inter. Proc. Conf.,* **686**, 50.

Shapiro S.L., Teukolsky S.A.: 1985, *Black Holes, a White Dwarfs, and Neutron Stars. Mir, Moscow.*

Shibata M.: 2003, *Ap. J.,* **595**, 992.

Shibata M. et al.: 2005, *Phys. Rev. Let.,* **96**, id. 031102.

Shibata M. et al.: 2006, *Phys. Rev. D,* **74**, id. 104026.

Shibata M., Taniguchi K.: 2006, *Phys. Rev. D,* **73**, id. 064027.

Smartt S.J.: 2009, *Ann. Rev. Astron. Astrophys.,* **47**, 63.

Stephens B.C., et al.: 2007, *Classical and Quantum Gravity,* **24**, 207.

Stephens B.C., Shapiro S.L., Liu Y.T.: 2008, *Phys. Rev. D.,* **77**, id. 044001.

Takiwaki T., Kotake K., Sato K.: 2009, *Ap. J.,* **691**, 1360.

Uzdensky D.A., MacFadyen A.I.: 2006, *Ap. J.,* **647**, 1192.

Uzdensky D.A., MacFadyen A.I.: 2007, *Ap. J.,* **669**, 546.

Van Paradijs J. et al.: 1997, *Astron. Astrophys.,* **317**, L9.

Vigorito C. et al.: 2008, *J. Phys. Conf. Ser.,* **136**, id.042074.

Wickramasinghe D. T., et al.: 2009, *Journ. Phys. Conf. Ser.,* **172**, 12.

Woosley S.E., Baron E.: 1992, *Ap. J.,* **391**, 228.

Woosley S.E., Timmer F.X., Baron E.: 1992, *NATO ASI Ser. C,* **377**, 189.

Yakovlev D.G., et al.: 2001, *Phys. Rep.,* **354**, 1.

Yu Y.W., Dai Z.G., Zheng X.P.: 2008, *MNRAS,* **385**, 1461.

Yungelson L.R., Livio M.: 1998, *Ap. J,* **497**, 168.

Zeldovich J.B., Novikov I.D.: 1977, *Theory of gravity and stellar evolution. Nauka, Moscow.*

Zhang W., Woosley S.E., MacFadyen A.I.: 2003, *Ap. J.,* **586**, 356.

A STUDY OF MASS LOSS AND DUST FORMATION NEAR HOT STARS

K.S. Kuratov[1,2], A.S. Miroshnichenko[1,3], A.V. Kusakin[4], N.Sh. Alimgazinova[1,2],
A.Zh. Nuryzbaeva[1,2], A.B. Manapbaeva[1,2], A.K. Kuratova[1,2]

[1] National center of space exploration and technologies, Almaty, Kazakhstan,
kenes.kuratov@.mail.ru

[2] Faculty of Physics and Technology, Al-Farabi Kazakh National University,
Almaty, Kazakhstan

[3] Department of Physics and Astronomy, University of North Carolina
Greensboro, NC 27402-6170, USA, *a_mirosh@uncg.edu*

[4] Fessenkov Astrophysical Institute, Observatory 23, Almaty, Kazakhstan

ABSTRACT. At present dust formation is well studied only near cool stars, whose surface temperatures are close to those of dust sublimation. Hot stars need to supply large amounts of circumstellar material to allow dust formation around them. Such conditions naturally exist near supergiants with masses over 25 $M_\odot$. The theory of stellar evolution predicts that less massive stars do not provide enough matter for dust formation. Nevertheless, dust exists near dwarfs with the B[e] phenomenon and giants of A–G spectral types which do not belong to star formation regions.

A large group of objects with the B[e] phenomenon with extremely strong emission-line spectra that are neither young nor highly evolved has been recently identified. They are called FS CMa type objects. Their infrared excesses imply a large amount of recently created dust. Therefore, these objects can noticeably contribute to the Galactic dust content, but they have not been taken into consideration from this perspective.

Key words: - Stars: emission-line, Be - Stars: evolution - (Stars:) circumstellar matter - (Stars:) binaries: general

1. Introduction

The B[e] phenomenon is defined as the presence of forbidden emission lines and strong infrared excess due to radiation from circumstellar dust in the spectra of B–type stars. It was discovered nearly 40 years ago in 65 Galactic objects by Allen & Swings (1976). The phenomenon exists at different evolutionary stages of several stellar groups: pre-main-sequence Herbig Ae/Be stars, compact Planetary Nebulae, symbiotic binary systems, and some massive supergiants (Lamers et al., 1998). However, the nature of 30 objects out of these 65 was not determined, and they were called unclassified objects with the B[e] phenomenon.

Miroshnichenko (2007) analyzed properties of the unclassified objects and summarized them as follows:

1. early-B to early-A type optical continuum with strong emission lines of hydrogen, Fe II, [O I], and sometimes of [Fe II] and [O III] (absorption lines from the hot star atmosphere may be present as well, but they are frequently veiled by the circumstellar continuum);

2. a large IR excess that peaks at $\lambda \sim 10$–30 μm and sharply decreases toward longer wavelengths;

3. location outside of star-forming regions; and

4. a secondary companion (so far discovered in about one third of the group members) which can be a fainter and cooler normal star or a degenerate object.

The group was named FS CMa type objects using the variable star name of the most typical object with the B[e] phenomenon (FS CMa = HD 45677, Swings 2006). Miroshnichenko et al. (2007) expanded the group with 10 objects found in the IRAS catalog by cross-identification with catalogs of optical positions. Miroshnichenko et al. (2011) found 20 more group objects by cross-correlating the Hamburg catalog of emission-line stars (Kohoutek & Wehmeyer, 1999), IRAS (IPAC, 1986), and 2MASS (Cutri et al., 2003) catalogs. Property 2 listed above is crucial to separate FS CMa objects from other hot emission-line stars. This criterion was applied to objects detected by the IRAS satellite, which has had a low sensitivity

and reliably measured fluxes only from the brightest objects. Other photometric criteria to find more candidates to the FS CMa group are presented below.

2. Properties of the FS CMa group objects

One of the main problems with determining the nature and evolutionary state of the FS CMa objects are transition of absorption lines, which form in the atmosphere of the B-type star and serve as diagnostics for the star temperature and luminosity, into emission caused by the circumstellar matter. This matter also produces continuum emission that fills in or weakens the absorption lines. Such a situation hampers luminosity and distance determination, especially in the absence of high-quality data. This was the case for many relatively faint objects (visual brightness $V \geq 10$ mag) in 1980's and 1990's.

Another problem is a combination of features of stars of different masses or evolutionary stages in one object. For example, such a combination can be a strong IR excess, typical of pre-main-sequence stars, and an extremely strong emission-line spectrum, typical of evolved high-luminosity stars (supergiants).

We began systematic medium- and high-resolution spectroscopic and multicolor photometric observations of the group objects in the end of 1990's. Even single high-resolution spectra that we obtained for some newly found objects for the first time (e.g., Miroshnichenko et al., 2000) allowed us to estimate distances to them using kinematical (radial velocity) information and interstellar extinction laws in their directions. Effective temperatures of the underlying B–types stars were estimated from excitation of the emission lines and dereddned optical photometry. As a result, we placed a number of FS CMa objects in the Hertzsprung-Russell diagram (HRD, see Fig. 1 where positions of supergiants with the B[e] phenomenon is shown for comparison) and showed that they were not high-luminosity or high-mass stars.

FS CMa objects show very strong emission-line spectra, much stronger (Miroshnichenko, 2008) than those of other groups of objects in the same photospheric temperature range (10000–30000 K). This suggests a large amount of circumstellar gas around the stars. Theory of stellar evolution cannot explain such large amounts by mass loss from a single star of masses predicted by positions of FS CMa objects in HRD. This indirectly suggests that FS CMa objects can be binary systems, in which a strong mass transfer between the stellar components is responsible for both circumstellar gas and dust.

Another distinct feature of FS CMa objects is a fast decrease of their IR flux, which is caused by radiation of the circumstellar dust, towards longer wavelengths starting from a peak at $\lambda \sim 10-30\mu$m (see
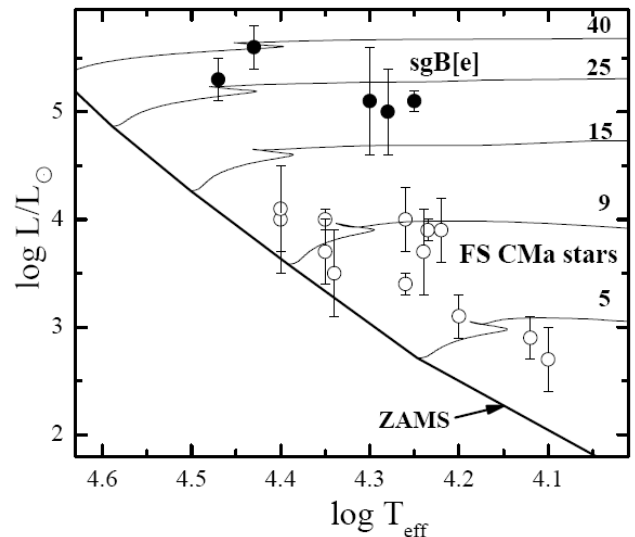
Figure 1: A Hertzsprung-Russell diagram for Galactic FS CMa stars and B[e] supergiants (B[e]sg) with known parameters (from Miroshnichenko 2007). Solid lines: the Zero-Age Main-Sequence (ZAMS) and evolutionary tracks for single rotating stars (Ekström et al. 2012) with initial masses in solar units indicated.

Fig. 2). Their IR color-indices are found in the same region of the IRAS color-color diagram as those of much cooler stars, which do not produce enough UV radiation to heat distant colder dust that radiates in the far-IR. This feature can be explained by compactness of the dust distribution near FS CMa objects and distinguishes them from pre-main-sequence Herbig Ae/Be stars, which have larger dusty disks and exhibit more far-IR radiation. Such an IR spectral energy distribution is also different from those of young Planetary Nebulae, whose envelopes contain much colder dust that produces mostly far-IR excess radiation and little or no near-IR excess.

Based on the described properties, we propose a model of FS CMa objects that includes a binary system, where mass transfer between the two stars led to the circumstellar envelope/disk formation. The gas responsible for emission lines is mostly located around the hot star, while the dust exists in the circumbinary area. So far only 12 objects from the FS CMa group have been recognized as binaries. This is due to weakness of the secondary components contribution to the total spectrum of the system. Typically the secondary components are 2–4 magnitudes fainter than the B–type primaries in the optical region of spectrum (e.g., Miroshnichenko, 2007; Miroshnichenko et al., 2015).

The HRD location of FS CMa objects imply intermediate masses (3–20 $M_\odot$) for the hot primary components, while the secondary components are probably less massive. This suggests that the number of such systems in the Galaxy can be large. Since they pro-
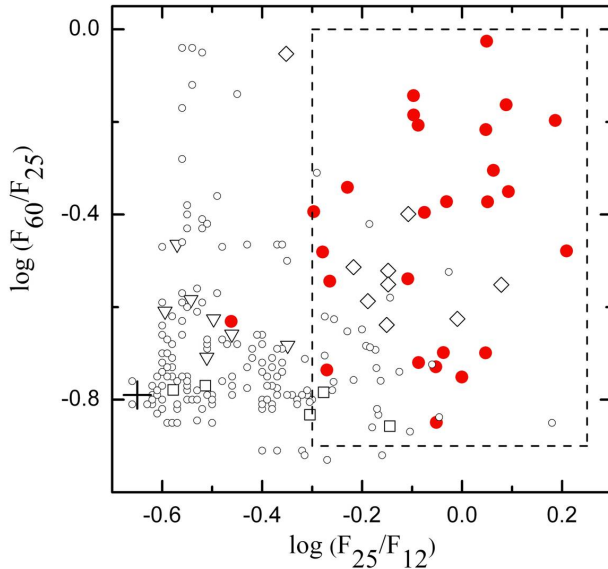
Figure 2: An IRAS color-color diagram for dusty objects. Symbols: FS CMa stars - red filled circles; symbiotic binaries – squares; carbon stars – triangles; AGB stars – circles; RV Tau stars (low-mass post-AGB objects) – diamonds. The dash-lined box shows location of the FS CMa stars. The large cross marks the stellar photospheric locus for all temperatures. F_{12}, F_{25}, and F_{60} are IRAS fluxes at the corresponding wavelengths.
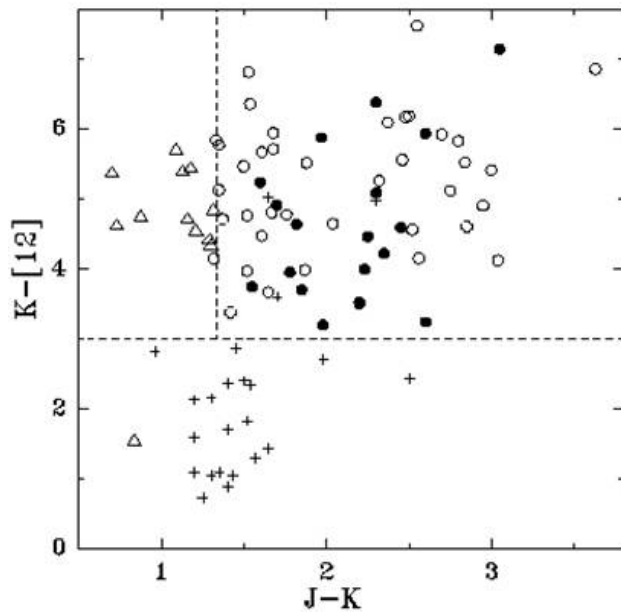
Figure 3: A photometric criterion that separates RV Tau stars (triangles), most cool stars (crosses), and FS CMa objects (groups members - filled circles, candidates to the group - open circles). [12] is the IRAS magnitude converted from the flux in the 12–μm photometric band.
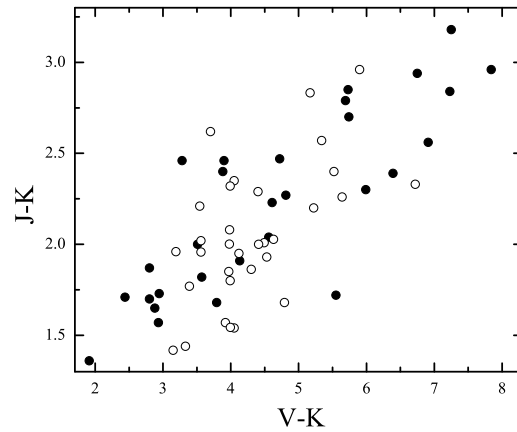
Figure 4: Optical-to-near-IR colors of the FS CMa group members and candidates. Symbols are the same as on the left panel.

duce dust, they can be important in the Galactic dusty budget. Therefore one could expect to find other such systems in the existing catalogs of photometric data or emission-line stars.

As photometric catalogs contain many more objects that spectroscopic ones and the IR spectral energy distribution can be used to separate FS CMa objects, we first looked in the IRAS catalog for new candidates to the group. However, the sensitivity of the IRAS photometric survey was low and allowed detection of only the brightest objects and those with the most dust. To expand the search opportunities, we analyzed other color-indices, including those in the near-IR and even the optical range. The goal was to compare the color-indices of FS CMa objects with those of other groups of objects with circumstellar dust. The results are shown in Figures 3 and 4.

3. Results

We collected optical and IR color-indices for representative samples of various objects showing the presence of circumstellar dust (e.g., pre-main-sequence Herbig Ae/Be stars, main-sequence Vega-type stars with debris dusty disks, Planetary Nebulae, symbiotic binaries, etc.) and proposed several criteria to search for FS CMa object candidates.

These criteria include the following:

1. m_B–$m_V \leq 1$ mag: separates out most cool stars but misses very reddened objects

2. $m_V - K \geq 2$ mag: separates out objects with no dust

3. $J - K \geq 1.4$ mag: separates out low-mass post-AGB objects

4. $K - [12] \geq 3$ mag: separates out most cool stars with no dust

In this list of criteria, m_B and m_V are the blue and visual magnitudes listed in the NOMAD catalog (Zacharias et al., 2004) are used, J and K are near-IR magnitudes at 1.25 and 2.2 μm, respectively; and [12] is the IRAS flux in 12-μm band converted into magnitudes.

The NOMAD catalog contains photometric data that includes 3 optical bands (not exactly coinciding with the standard BVR bands) and 3 near-IR bands from the 2MASS catalog. We started searching the entire sky for new candidates to the FS CMa group using the above criteria in NOMAD. This search is complemented by collecting information from other sources, such as IR surveys WISE (Wright et al., 2010) and AKARI (Murakami et al., 2007), and optical variability monitoring programs, such as ASAS (Pojmanski, 1997).

4. Conclusions

1. We found a new group of objects which create circumstellar dust and may be important for the dust production in the Galaxy. Currently the group has about 70 members and candidates. Most of them are fainter than $V \sim 11$ mag. The group is called the FS CMa type objects.

2. A current explanation for the group nature involves intermediate-mass binary systems at or after a stage of significant mass transfer due to a Roche lobe overflow by one of the stars in the system. This model is supported by calculations of binary evolution (van Rensbergen et al., 2008).

3. The FS CMa objects exhibit strong emission-line spectra indicative of a significant amount of circumstellar material in the system consistent with the assumption of mass transfer.

4. The secondary companion to the hot primary is typically a few times fainter that makes hard detecting them.

5. We continue a search for more group candidates, which will be identified using photometric criteria developed by us and observed spectroscopically to confirm the presence of the B[e] phenomenon. So far we have searched about one half of the sky and found over 100 candidates. Our previous experience shows that most candidates found using our criteria show the presence of the B[e] phenomenon.

References

Allen D.A. & Swings J.-P.: 1976, *A&A*, **47**, 293.

Cutri R.M., Skrutskie M.F., Van Dyk S. et al.: 2003, CDS/ADC Collection of Electronic Catalogues, 2246.

Ekström S., Georgy C., Eggenberger P. et al.: 2012, *A&A*, **537**, A146.

Kohoutek L. & Wehmeyer R.: 1999, *A&AS*, **134**, 255.

IPAC: 1986, IRAS catalogue of Point Sources, Version 2.0, Joint IRAS Science W.G. (Vizier Catalog II/125).

Lamers H.J.G.L.M., Zickgraf F.-J., de Winter D., Houziaux L., Zorec J.: 1998, *A&A*, **340**, 117.

Miroshnichenko A.S.: 2007, *ApJ*, **667**, 497.

Miroshnichenko A.S.: 2008, in "Mass Loss from Stars and the Evolution of Stellar Clusters", eds. A. de Koter, L.Smith, and L.B.F.M.Waters, *ASP Conf. Ser.*, **388**, 205.

Miroshnichenko A.S., Chentsov E.L., Klochkova V.G. et al.: 2000, *A&AS*, **147**, 5.

Miroshnichenko A.S., Manset N., Kusakin A.V. et al.: 2007, *ApJ*, **671**, 828.

Miroshnichenko A.S., Manset N., Polcaro V.F., Rossi C., Zharikov S.V.: 2011, In "Active OB stars: structure, evolution, mass loss and critical limits", *Proc. of the IAU Symposium*, **272**, 260.

Miroshnichenko A.S., Zharikov S.V., Danford S., Manset N., Korčáková D., Kříček R., Šlechta M., Omarov Ch.T., Kusakin A.V., Kuratov K.S., Grankin K.N.: 2015, *ApJ*, **809**, 129.

Murakami H., Baba H., Barthel P. et al.: 2007, *PASJ*, **59**, 369.

Pojmanski G.: 1997, *Acta Astronomica*, **47**, 467.

Swings J.-P.: 2006, In "Stars with the B[e] Phenomenon, eds. M.Kraus and A.S.Miroshnichenko, *ASP Conf. Ser.*, **355**, 3.

van Rensbergen W., De Greve J.P., De Loore C., Mennekens N.: 2008, *A&A*, **487**, 1129.

Wright E.L., Eisenhardt P.R.M., Mainzer A.K. et al.: 2010, *AJ*, **140**, 1868.

Zacharias N., Monet D.G., Levine S.E., Urban S.E., Gaume R., Wycoff G.L.: 2004, *Bull. American Astron.Soc.*, **36**, 1418, (Vizier Catalog I/297).

IRAS22150+6190: A POORLY STUDIED YOUNG STAR

K.S. Kuratov[1,2], O.V. Zakhozhay[3], A.S. Miroshnichenko[1,4], V.A. Zakhozhay[5]

[1] National center of space exploration and technologies, Almaty, Kazakhstan,
kenes.kuratov@.mail.ru

[2] Faculty of Physics and Technology, Al-Farabi Kazakh National University,
Almaty, Kazakhstan

[3] Main Astronomical Observatory, National Academy of Sciences of Ukraine, Kyiv 03680,
Ukraine

[4] Department of Physics and Astronomy, University of North Carolina
Greensboro, NC 27402-6170, USA, *a_mirosh@uncg.edu*

[5] V.N.Karazin Kharkiv National University, Kharkiv, Ukraine

ABSTRACT. Many young stellar objects have been discovered in the course of the InfraRed Astronomical Satellite (IRAS) mission, which observed almost the entire sky in four photometric bands between 12 and 100 microns in 1989. These discoveries led to constraining the evolution of stars of various masses and the material that was left from the proto-stellar clouds. Investigation of young stars are important because they allow us to learn more about star and planet formation modes as well as better understand processes of the proto-stellar debris dispersal. Nevertheless, not all optical counterparts of such objects have been revealed or studied in detail. We report our multicolor optical photometric observations of IRAS 22150+6109 obtained at the Tien-Shan Astronomical Observatory near Almaty, Kazakhstan, as well as preliminary results of our analysis of the spectral energy distribution. Fundamental parameters of the star are estimated under an assumption that it has a zero-age main-sequence luminosity and a spectral type of B3. Our plans on further observations and modeling of the object are outlined.

Key words: - Stars: emission-line, Be - Stars: evolution - Stars: pre-main sequence - (Stars:) circumstellar matter - (Stars:) individual: IRAS 22150+6109

1. Introduction

The subject of this study is the infrared source IRAS 22150+6109. We identified it with a $V = 11$ mag star found in the catalog of early-type emission-line objects by Wackerling (1970). The object is located in the direction of an active star-forming region L1188 in Cepheus at a distance of 910 pc from the Sun (Abraham et al., 1995). No emission from H_2O, OH, or CS molecules has been detected from the object (Wouterloot et al., 1993; Bronfman et al., 1996). Results on CO emission are controversial: negative detection by Wouterloot & Brand (1989) and positive detection by Kerton & Brunt (2003). Nevertheless, IRAS22150+6109 exhibits a strong infrared excess that is indicative of an intermediate-mass star in transition from the pre-main-sequence to main-sequence stage of evolution. The nearly main-sequence status is supported by a weak Hα emission detected by the Hamburg survey for emission-line stars (Kohoutek & Wehmeyer, 1999). It is included in a catalog of reflection nebulae Magakian (2003).

Our goal was to obtain an optical spectrum and optical multicolor photometry of the star to constrain its spectral energy distribution (SED), collect available infrared photometric data, and model the SED to derive the properties of the circumstellar dust.

2. Observations

The star was observed photometrically at the Tien-Shan Astronomical Observatory (near Almaty, Kazakhstan) in $UBVRI$–bands of the Johnson photometric system using the photometer FP3U (Bergner et al., 1988). Ten observations were obtained in 1997–1999. The photometry was published by Kuratov (2004). Additionally, a high-resolution spectrum ($R = 60000$) was obtained at the 2.7 m telescope of the McDonald Observatory (Texas, USA) in 2009 by one of us (A.M.).

Infrared photometric data were collected from different catalogs. Near-IR data in the JHK–bands were taken from the 2MASS catalog (Cutri et al., 2003), fluxes in four bands between 3.4 and 21 μm were taken
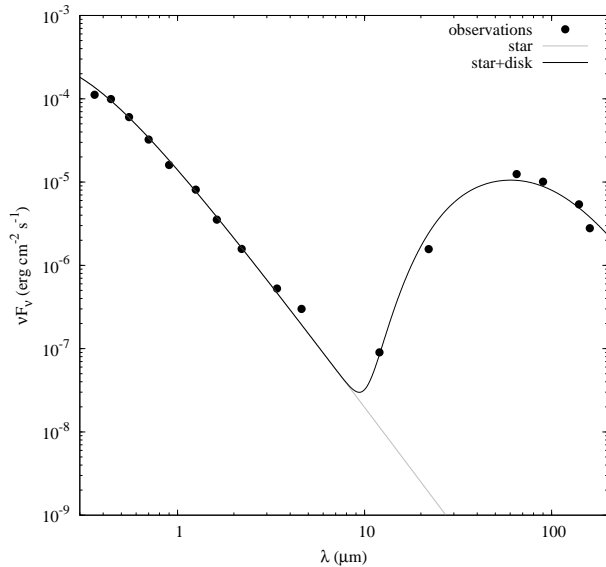
Figure 1: The observed photometric SED of IRAS 22150+6109 (black dots) is shown in comparison with the best-fit face-on disk model (black solid line). The model spectrum is shown with the gray solid line.

Figure 2: Best-fit SEDs for the star with T_* - solid line, $T_{*,min}$ - dotted line and $T_{*,max}$ - dashed line. The observed SED of IRAS 22150+6109 (black dots).

from the WISE catalog (Wright et al., 2010), and fluxes in five bands between 18 and 160 μm were taken from the AKARI catalog (Murakami et al., 2007).

Fluxes measured in magnitudes were converted into energy units using zero-magnitude fluxes adopted from the listed above sources of information. Optical magnitudes were converted into fluxes using the calibration from Straizhys (1977).

3. Data Analysis and Modeling

The spectrum we obtained has a low signal-to-noise ratio but is indicative of the stars properties. The absence of He I lines in emission implies a spectral type later than B2. The Hα line has a very weak single emission peak that points to a nearly face-on disk orientation.

The optical photometry obtained during nearly 2 years shows brightness variations of 0.2 magnitude with an average of $V = 10.82 \pm 0.07$ mag. The average color-indices suggest the stars spectral type of B3 and an extinction of $A_V = 2.0 \pm 0.1$ mag. The infrared photometry was obtained at different times from 2001 to 2010, but the fluxes seem to be consistent with each other (see Fig. 1). The observed SED was dereddened using a standard interstellar extinction law from Savage & Mathis (1979).

To model the SED of IRAS 22150+6109, we assumed that it consisted of a black-body emission from a dwarf star and a protoplanetary disk.

$$f_{\nu,*} = \varphi \pi R_*^2 B_\nu(T_*), \qquad (1)$$

where φ is a flux normalization constant, $B_\nu(T)$ is the Plank function, R_* and T_* are the stellar radius and effective temperature. For the calculations we used $R_* = (5 \pm 0.3) R_\odot$ and $T_* = 20000 \pm 1000 K$, which is typical for a B3 V star. To account for the excess radiation, which we assume to occur at wavelength $\lambda > 1\mu$m, we modeled a SED from a protoplanetary disk following the procedure described by Andrews & Williams (2005).

The flux density is given by

$$f_{\nu,disk} = \varphi \int_{R_{in}}^{R_{out}} B_\nu(T_r)Q_\nu 2\pi r dr, \qquad (2)$$

where R_{in} and R_{out} are disk inner and outer radii, respectively. Dust grain emission efficiency $Q_\nu = 1 - exp(-\tau)$ and τ is an optical thickness of the disk material, $\tau = \Sigma_r \kappa_\nu$.

The dust opacity is described as a power law in frequency

$$\kappa_\nu = \kappa_0 \left(\frac{\nu}{\nu_0}\right)^\beta, \qquad (3)$$

with index β and a normalization of $\kappa_0 = 0.1\,cm^2\,g^{-1}$ at $\nu_0 = 1000$ GHz (Beckwith et al., 1990). This value assumes a 100–to–1 mass gas–to–dust ratio.

The temperature T_r and surface density Σ_r distributions are assumed to be power law functions of the disk radius:

$$T_r = T_{sub} \left(\frac{r}{R_{sub}}\right)^q, \qquad (4)$$

$$\Sigma_r = \Sigma_{sub} \left(\frac{r}{R_{sub}}\right)^p, \qquad (5)$$
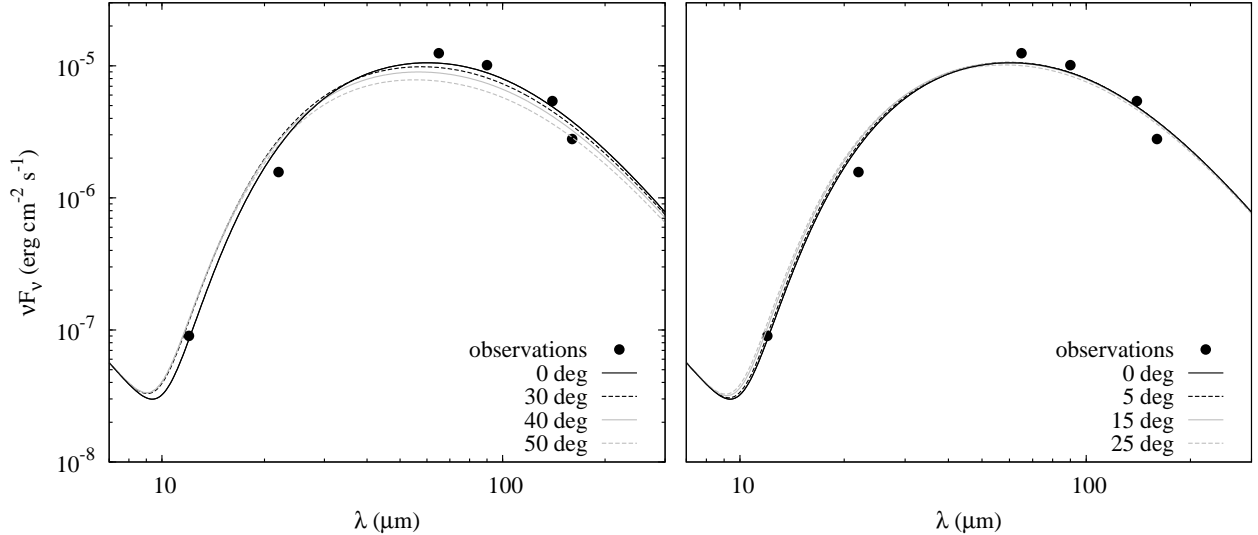
Figure 3: Model SEDs for the system (star+disk) inclined at $i = 30$–50 degrees (left panel) and for $i = 5$–25 degrees (right panel). The black solid line in each panel denotes the SED for the system with the disk oriented face-on ($i = 0$ degrees).

where R_{sub} is a disk radius at which it's temperature equals 1500 K - the sublimation temperature T_{sub} of the disk dust particles (Dullemond, Dominic & Natta, 2001). In our particular case $R_{sub} \approx 2$ AU. Σ_{sub} is a surface density at R_{sub}, that equals to 2000 $g\ cm^{-2}$ (Dullemond et al., 2001) and indices p and q are taken to be free parameters.

Based on the calculation algorithms described above, we simulated the SEDs of the disk with different sizes. We varied R_{in} between 2 and 200 AU with a step of 1 AU and R_{out} between 10 and 1500 AU with a step of 10 AU (excluding the cases when $R_{in} = R_{out}$). The surface density power law p we varied from -1.5 (as for the mass surface density of the current solar system, Carpenter et al., 2009) to 0 (constant surface density) with a step of 0.5. We varied β between 0 and 2 with a step of 1 (Beckwith et al., 1990) and q between -0.75 and -0.35 with a step of 0.05 Andrews & Williams (2005).

The best fit we found by minimizing

$$\chi^2 = \sum_{i=1}^{n} \left(\frac{F_{obs} - F_{mod}}{F_{mod}} \right)^2, \qquad (6)$$

where F_{obs} and F_{mod} are the observed and modeled fluxes (at the corresponding wavelength) respectively. We assume that disk emission excess only occurs at wavelengths $> 1\ \mu$m, and hence we consider disk model fits only in this region.

We found that the best fit ($\chi^2 = 0.596$) has a system with $R_{in} = 123$ AU, $R_{out} = 1030$ AU, $p = -1, q = -0.65$ and $\beta = 1$. Figure 1 shows the SED for the system with the best fit parameters (black line), the

observations (black filled circles), and SED from the star (gray line).

To investigate the modeling uncertainties due to those of the stellar parameters, we found a minimum of χ^2 assuming that T_* is $T_{*,min} = 19000$ K and $T_{*,max} = 21000$ K. Such a change of the stellar temperature causes mainly the differences in the disk inner and outer radii: R_{in} from 107 AU to 141 AU and R_{out} from 1180 AU to 770 AU, for $T_{*,min}$ and $T_{*,max}$, respectively. For the star with $T_{*,min}$, the best fit is found for the system with $\beta = 2$. All other parameters for $T_{*,min}$ and $T_{*,max}$ do not change comparing to the ones for T_*. Figure 2 illustrates the total SEDs for the best fit systems with different T_*.

We also analyzed the possibility that the dusty disk is tilted with respect to the line of sight. For this purpose we varied the disk parameters R_{in}, R_{out}, p and β in the same ranges and with the same steps as for the face-on disk. We did not vary q, because in all previous modeling (for different T_*) this parameter was always the same and equal to -0.65. Inclination i was an additional free parameter that we varied from 0 to 50 degrees with a step of 10 degrees. The geometry of an inclined disk was accounted for following the procedure described in Zakhozhay, del Burgo & Zakhozhay (2015), assuming that the inner and outer edges of the disk have a cut-off flat geometry and emit as black bodies with constant temperatures, equal to the temperatures at the inner and outer ages of the disk derived from the equation 4. We found that the minimum χ^2 has the system with the same parameters as those derived for $i = 0$. Figure 3 illustrates how the SED of the system (star+disk) changes with the
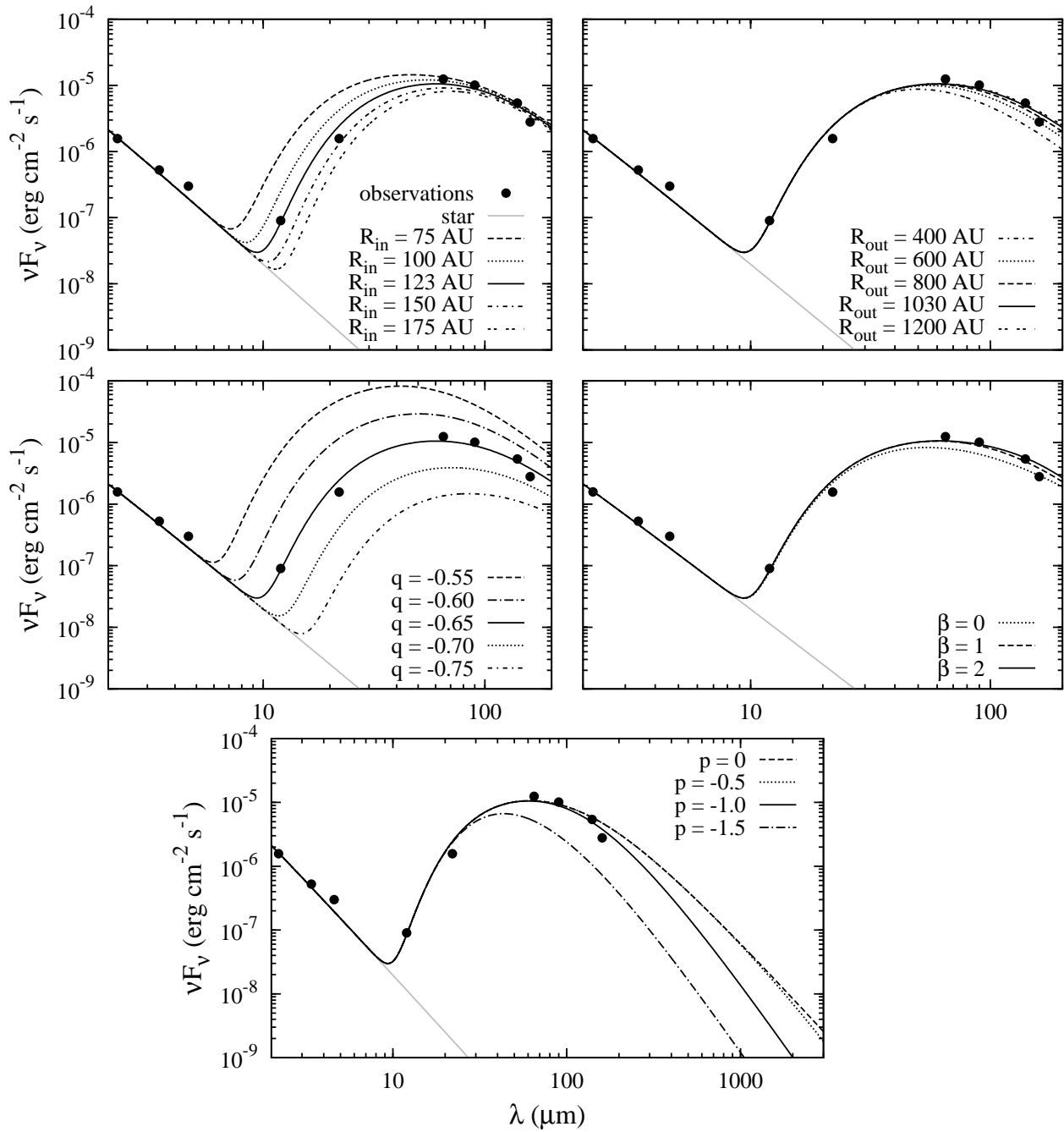
Figure 4: Effects of reasonable variations of the model parameters on the total system SED profile. The black solid line in each panel denotes the SED for the best fit system with $R_{in} = 123$ AU, $R_{out} = 1030$ AU, $p = -1, q = -0.65$ and $\beta = 1$. The parameter being varied from this fiducial set is indicated in each panel. The model spectra is shown with the gray solid line.

inclination increase for 30–50 degrees (left panel) and for 5–25 degrees (right panel). As one can see, the change of the SEDs shape is insignificant for the inclinations up to 10 degrees. In fact, the χ^2 increases only from 0.596 to 0.631. That is why we expect that disk should be oriented close to the face-on. Figure 4 illustrates how total system SEDs depend on the disk model free parameters.

4. Conclusions

From our modeling of the SED of IRAS 22150+6109, we found that the star is surrounded by a dusty disk that has been swept away to a distance of ~60 sublimation radii and is viewed face-on. The disk has a shallower density distribution that a typical accretion disk. The stars brightness corrected for the reddening is consistent with a typical luminosity of a zero-age main-sequence star of the spectral type B3 located at a distance of ~900 pc from the Sun. Our dusty disk modeling confirmed the nearly main-sequence status of the star. With the derived fundamental parameters (Teff, L), the star should have a mass of 6-7 M$_\odot$ and a very short pre-main-sequence lifetime (Palla & Stahler, 1993).

Higher signal-to-noise ratio optical spectra are needed to refine the fundamental parameters and check for binarity, because such stars are frequently born in pairs. We are also planning to model the SED with more realistic dust properties.

References

Abraham P., Dobashi K., Mizuno A., Fukui Y.: 1995, *A&A*, **300**, 525.
Andrews S.M., Williams J.P.: 2005, *ApJ*, **631**, 1134.
Beckwith S.V.W., Sargent A.I., Chini R.S., Güsten R.: 1990, *AJ*, **99**, 924.
Bergner Yu.K., Bondarenko S.L., Miroshnichenko A.S. et al.: 1988, *Izvestia GAO AN SSSR*, **205**, 142.
Bronfman L., Nyman L.-A., Mai J.: 1996, *A&AS*, **115**, 81.
Cutri R.M., Skrutskie M.F., Van Dyk S. et al.: 2003, CDS/ADC Collection of Electronic Catalogues, 2246.
Dullemond C.P., Dominik C., Natta A.: 2001, ApJ, **560**, 957.
Kerton C.R. & Brunt C.M.: 2003, *A&A*, **399**, 1083.
Kohoutek L. & Wehmeyer R.: 1999, *A&AS*, **134**, 255.
Kuratov K.S.: 2004, *Transactions of the National Academy of Kazakhstan*, **4**.
Magakian T.Y.: 2003, *A&A*, **399**, 141.
Murakami H., Baba H., Barthel P. et al.: 2007, *PASJ*, **59**, 369.
Palla F. & Stahler S.V.: 1993, *ApJ*, **418**, 414.
Savage B.D. & Mathis J.S.: 1979, *Annual Rev. A&A*, **17**, 73.
Straizhys V.: 1977, "Multicolor photometry of stars", Vilnis, Mokslas publ.
Wackerling L.R.: 1970, *Mem. Roy. Astr. Soc.*, **73**, 153.
Wouterloot G.A. & Brand J.: 1989, *A&AS*, **80**, 149.
Wouterloot G.A., Brand J., Fiegle K.: 1995, *A&AS*, **98**, 589.
Wright E.L., Eisenhardt P.R.M., Mainzer A.K. et al.: 2010, *AJ*, **140**, 1868.
Zakhozhay O.V., del Burgo C., Zakhozhay V.A.: 2015, *Advances in Astronomy and Space Physics*, (in press).

SPECTROSCOPIC VARIABILITY OF THE SUPERGIANTS HD21389 AND HD187982

Y.M.Maharramov, A.Sh.Baloglanov

Shamakhy Astrophysical Observatory named after N.Tusi, Azerbaijan National Academy of Sciences, Yu.Mammadaliyev Settlement, Shamakhy district, Azerbaijan
y_meherremov@rambler.ru

ABSTRACT. It has been revealed that absorption in the line of H_α has complex structure in the spectrum of the star HD21389 depending on the activity phase of the atmosphere. The profile of the line has inverse P Cyg type in the active phase of the star atmosphere. The emission components in the red and violet wing of the profile form and disappear. All the measured parameters of the H_α and H_β lines change. It is supposed that such variations may be due to non-stationary and strong flow substance in the atmosphere of these stars.

Appearance and disappearance of asymmetry in the profile of NaID doublet and formation of the H_α line type inverse P Cyg occurs synchronously in an active phase of the atmosphere of HD 21389. We assume that these changes are formed under the influence of the general mechanism which might be responsible for the observed variation is the growth of the envelope of the star with a following ejection of matter.

Our researches showed that the values of radial velocity of the FeII lines change with time. However, we found no correlation of these changes with the period of 7.7 days found by earlier authors.

Key words: stars, radial velocity, spectral parameters, stellar wind.

1. Introduction

The supergiant star HD21389 belongs to the stars with P Cyg type profile H_α line. According to (De Jager et al., 1988, Straizys et al., 2007, Takeda et al., 2000, Takeda et al., 1998, Verdugo et al., 1999), its spectral class is A0Ia, apparent magnitude is $m_v = 4^m.53$, mass is $M_*/M_\odot$=19.3, radius is $R_*/R_\odot$=97, luminosity is $\log (L_*/L_\odot)$ =4.87, effective temperature is T_{eff} = 10500K, acceleration of gravity at the surface is logg=1.70, and rotation speed is vsini = 53 km/s. It is believed that it belongs to the OB1 association.

However, according to other authors (Achmad et al., 1997; De Jager et al., 1988; Talavera et al., 1987; Verdugo et al., 1999), the stellar parameters are somewhat different, T_{eff}=11000K, 9730K and 10100K, $M_*/M_\odot$=14, $M_*/M_\odot$=16, $R_*/R_\odot$=104.2, $R_*/R_\odot$=99.

In (Zeinalov, 1997; Zeinalov, 2003; Zvereva et al., 1984; Rzaev et al., 1989; Takeda et al., 2000; Verdugo et al., 1999; Weaver et al., 1995; Zeinalov et al., 1990), the H_α, H_β, H_γ, H_δ, H_ϵ, HeI (4471, 4921, 6678 Å), SiII

(3853.6, 3856, 3862.5 Å), NaI (D1 and D2), MgII (4481 Å), DIB (5797, 5780, 5850, 6614 Å), OI (6156, 6157, 6158 Å), CII (4267 Å), FeII (4923.9, 6147.7, 6149.3 Å) lines observed in star spectra were investigated, their equivalent widths were measured, changes were considered, and contours of these lines were presented. It is revealed that the profile of the H_α line has difficult structure and following shapes were observed:

a) normal P Cyg profile;
b) inverse P Cyg profile;
c) pure absorption profile;
e) pure emission profile;
e) $H\alpha$ exhibiting a three-component shape: the emission profiles on both sides of central absorption component.

One of the interesting moments is that in the profiles of the DIB λ5797 Å line (Diffuse Interstellar Band) observed in the spectra of this star at different times structural changes are found (Galazutdinov et al., 2004). As strong change happens in the violet wing the equivalent width increases almost twice. Value of equivalent width changes from W (5797 Å) = (74±4) mÅ to (156±7) mÅ.

It is revealed that in the spectra of supergiant HD21389, the form, equivalent width, line depth, radial velocity and other parameters of the H_α line show strong change with time. Equivalent width changes from 0.09 Å to 0.45 Å, i.e. almost five times (Talavera et al., 1987; Weaver et al., 1995).

In addition, in (Zeinalov, 1997; Zeinalov, 2003; Zvereva et al., 1984; Rzaev et al., 1989; Burki, 1978; Denizman et al., 1988; Gray et al., 1987; Zeinalov et al., 1990) it was noted that the form of the profile of H_β line, and also other parameters of this line show strong change. They found even weak emission component in the H_β line profiles. On the basis of measurements of the radial velocity on optical depth authors researched the atmosphere of this star (Burki, 1978; Zeinalov et al., 1990). It appeared that the radial velocity determined by the lines H_α, H_β, HeI and SiII changes on optical depth. They explain these changes with pulsations of the atmosphere of this star.

HD187982 is a supergiant of spectral type A1Iab with the following parameters (Evans et al., 2003; Przybilla et al., 2010; Verdugo et al., 1999):

m_v=$5^m.58$, T_{eff} = (9300±250)K, $M_*/M_\odot$=15,

$R_*/R_\odot$=78, logg=1.60±0.15, vsini = (15±6) km/s.

The supergiant HD187982 belongs to the OB4 associations. In (Abt et al., 1995, Snell et al., 1981, Verdugo et al., 1999) the study of H_α, H_γ, MgII (4481 Å), and FeII (4924, 5018, 5169 Å) lines observed in the atmospheres of this supergiant is presented. It is noted that generally the profiles of the H_α line are observed in absorption. Sometimes in the red wing of the profile of H_α line is observed weak emission component. A more complete explanation of appearance and disappearance of these components require additional observations.

In the present paper, which can be considered a continuation of the above studies, we analyze variations of the H_α, H_β, HeI (5876 Å), NaID and FeII lines in the spectra of HD187982 with the aim to study their peculiarities.

We believe our results will be of interest for further studies of these remarkable stars.

2. Observation and processing

Spectral observations of the stars HD21389 and HD187982 in 2005-2014 were carried out using a CCD detector in the echelle spectrometer mounted at the Cassegrain focus of the 2-m telescope of the Shamakhy Astrophysical Observatory (Mikailov et al., 2005). The spectral resolution was R=15000, and the spectral range $\lambda\lambda 4700 \div 6700$Å. The signal-to-noise ratio was S/N=200.

Two spectra of the target stars were obtained on each night of observation. The average exposure was 600-900s, depending on the image quality. Note that, fast changes in the spectra during the night weren't found. Therefore the profiles observed in one night were averaged.

In addition to the observations of the target stars, we also obtained numerous spectra of standard stars, the day and night backgrounds, flat fields, and comparison stars, to enable analysis of the stability of the hardware and telescope-receiver complex.

The Echelle spectra were processed by the standard technique using the DECH20 and DECH20t software (Galazutdinov, 1992).

The errors in our equivalent widths (W) do not exceed 5%, and the errors in the radial velocities (Vr) are no larger than $\sim \pm 2$ km/s. Appropriate heliocentric corrections were included during data processing.

Profiles of the H_α, H_β, HeI, etc. lines in the spectra of supergiants HD21389 and HD187982 were investigated.

HD21389. The spectra obtained 2005, 2006 and 2014 were investigated. Structures of the profiles and value of radial velocities and spectral parameters of the H_α, H_β, HeI and the NaID doublet lines are presented.

The processing of H_α and H_β hydrogen lines in the HD21389 spectrum immediately revealed changes in profiles of the H_α line that occur with time. From fig. 1 it is visible that on 20.09.2005 in the spectrum of the supergiant HD21389 the profile of the H_α line is observed in pure absorption and on 11.11.2006 and 11.09.2014 the profile of the line is observed in the inverse and normal P Cyg profile, respectively (fig. 1).

Unfortunately, as insufficient observation materials we didn't manage to follow these interesting changes in detail.

Apparently from table 1, on 20.09.2005 the radial velocity determined by the H_α and H_β lines are equal -29 km/s and -14 km/s, respectively. However, on 11.11.2006 the radial velocity strongly differs from the values observed on 20.09.2005. In absorption the radial velocity of the H_α lines is 4 km/s, and in emission is -69 km/s. The radial velocities in absorption of the H_α line differ 7 – 12 times. Such strong changeability of the radial velocity shows about strong physical process this star occurring in the atmosphere.
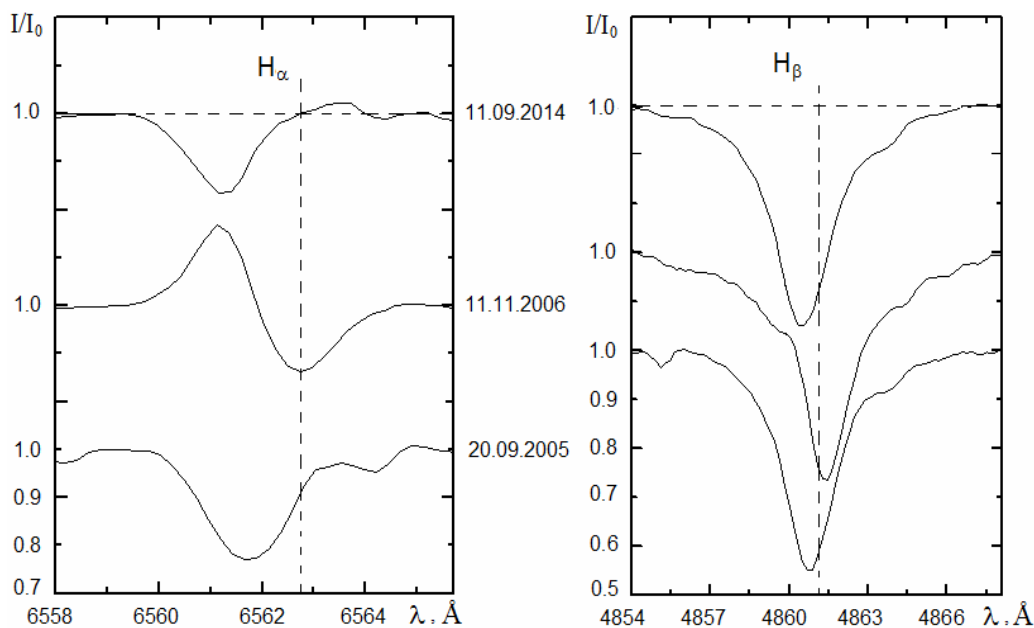
Figure 1: Profiles of the H_α and H_β lines of HD21389 on different dates.
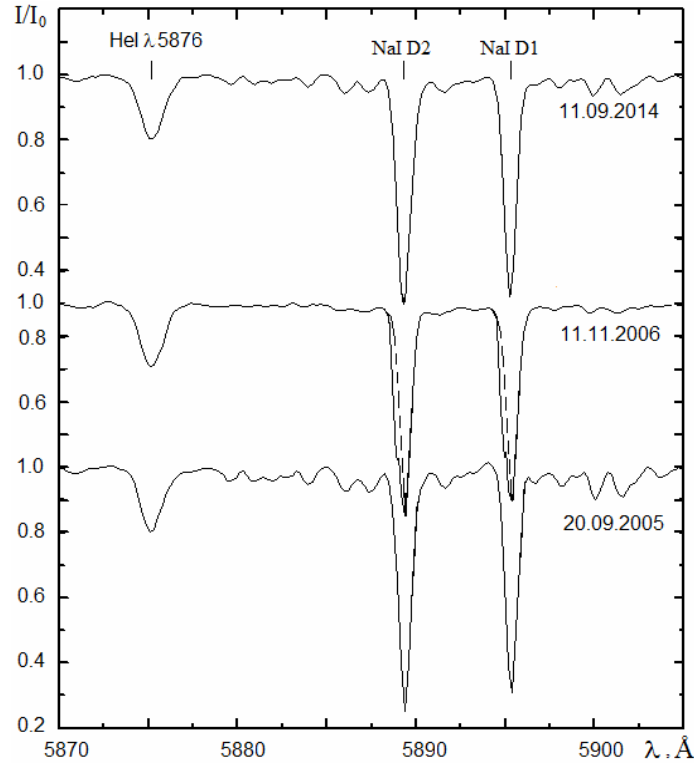
Figure 2: Profiles of the HeI and NaD lines of HD21389 on different dates.

Table 1: Results of measurements of spectral parameters of lines H_α, and H_β

Date	HD21389											
	H_α (abs)				H_α (em)				H_β			
	Vr (km/s)	W Å	$\Delta\lambda_{1/2}$ Å	r_v	Vr (km/s)	W Å	$\Delta\lambda_{1/2}$ Å	r_v	Vr (km/s)	W Å	$\Delta\lambda_{1/2}$ Å	r_v
20.09.2005	-29	0.48	1.7	0.77	-	-	-	-	-14	1.39	2.4	0.55
11.11.2006	4	0.19	1.3	0.86	-69	0.19	1.1	1.17	10	1.68	2.2	0.53
11.09.2014	-49	0.39	1.5	0.81	-	-	-	-	-30	1.55	2.7	0.55

Date	HD187982											
	H_α (abs)				H_α (em)				H_β			
	Vr (km/s)	W Å	$\Delta\lambda_{1/2}$ Å	r_v	Vr (km/s)	W Å	$\Delta\lambda_{1/2}$ Å	r_v	Vr (km/s)	W Å	$\Delta\lambda_{1/2}$ Å	r_v
01.09.2013	-29	0.89	2.5	0.72	79	0.02	0.58	1.04	-33	2.46	3.1	0.47
06.09.2013	-23	0.77	2.6	0.76	70	0.03	0.72	1.04	-33	2.26	3.2	0.48
02.10.2013	-18	1.29	2.9	0.69	-	-	-	-	-18	2.40	3.0	0.43
03.10.2013	-17	1.33	2.6	0.68	-	-	-	-	-19	2.42	3.2	0.45
21.06.2014	-11	1.06	2.3	0.67	-	-	-	-	-16	2.35	2.9	0.42
04.07.2014	-5	1.15	2.3	0.63	-	-	-	-	-9	2.53	2.7	0.39
11.07.2014	-6	1.10	2.1	0.63	-	-	-	-	-13	2.41	2.7	0.40
18.07.2014	-5	1.33	2.5	0.62	-	-	-	-	-8	2.57	3.0	0.38
24.07.2014	-12	1.36	2.4	0.59	-	-	-	-	-14	2.41	2.7	0.37
09.08.2014	-13	1.38	2.6	0.59	-	-	-	-	-12	2.80	3.2	0.39

As shown on 11.11.2006, we observed an inversion of the P Cyg profile of the H_α line. The inverse P-Cyg-profile may be explained by the high-velocity motion of wind matter away from the observer. This suggests that, as a result of a strong stellar wind, the absorption component of the H_α line is shifted to the red region of the profile while the emission component is blueshifted.

From fig. 1 and tab. 1 it is visible that when the H_α is observed inverse P Cyg, the structure of the profile of H_β changed a little and this line displaced to longer wavelength. It is interesting that when the H_α is observed inverse P Cyg, the profile of HeI (5876 Å) line does not change. It means that in this case, the deep layers of the HD21389 atmosphere are relatively stable.

In addition, from tab. 1 it is visible that during an inversion event, in the H_α line half-width ($\Delta\lambda_{1/2}$) and equivalent width decrease, and residual intensity grows. At the same time, in the H_β half-width decreased and the

residual intensity changed very little, at the same time equivalent width on the contrary increased. And from tab. 2 it is visible that in HeI the residual intensity, half-width and equivalent width didn't change.

The spectrum observed on 11.09.2014 shows that in the red wing of the H$_\alpha$ line are present weak emission component (fig. 1). When comparing it became clear that in this case, the H$_\alpha$ and H$_\beta$ lines were strongly displaced to the violet side of the spectrum and radial velocity became more than 11.11.2006 (fig. 1 and tab. 1). This time in the HeI lines (5876 Å) and NaID doublet any change hasn't occurred.

Unfortunately, as insufficient observation material we can't reveal certain regularity.

HD187982. Profile of the H$_\alpha$ line is P Cyg type. On the basis of the observed spectra the profiles of the H$_\alpha$, H$_\beta$, HeI (5876 Å), NaID doublet and FeII (4924, 5018, 5169 Å) lines were investigated. The radial velocities, residual intensities and half-widths of the studied lines are determined. In the spectra of HD187982 observed on 01.09 and on 06.09.2014 the profiles of the H$_\alpha$ lines consist of a strong absorption component and a weak emission component which is observed on the red wing of the H$_\alpha$ line (fig. 3). It is also interesting that from emission component of the H$_\alpha$ line to longer wavelength there is a weak absorption component again. But in the spectra of 02.10.2013 and 03.10.2013 the H$_\alpha$ line is visible only in absorption and there are no accompanying components.

Apparently from fig. 3 and 4, in all cases, in the profiles of the H$_\beta$ and NaI lines structural changes aren't observed. If we follow the radial velocities of H$_\alpha$, H$_\beta$, HeI and NaID doublet lines, we will see that the radial velocity of H$_\alpha$ line changes, but no significant variability was observed. In the HeI lines and the NaID doublet the changing of Vr is very weak.

It was revealed that change of the radial velocity in the H$_\beta$ line shows interesting similarity to the form of H$_\alpha$ profile. As it was underlined above, in the spectra of HD187982 star the profile of the H$_\alpha$ line is observed in two following forms:

a) the profile of the H$_\alpha$ line consists of a strong absorption component and a weak emission component which is observed on the red wing of the H$_\alpha$ line.

b) the profile of the H$_\alpha$ line is observed in pure absorption.

On 01.09.2013, 06.09.2013, 02.10.2013 and 03.10.2013 dates in the spectra of HD187982 star the radial velocity of the H$_\beta$ line there were -33 km/s, -33 km/s, -18 km/s and -19 km/s, respectively.

Apparently, upon transition of the H$_\alpha$ profile from a form a) to the b) case the H$_\beta$ line moves to the red side, and the radial velocity changes sharply, but in spectral parameters no significant variability was observed (tab. 1).

In addition, upon such transition the equivalent width of the H$_\alpha$ increases, but in half-width and in residual intensity no significant variability was observed. At the same time in the radial velocity and spectral parameters of the HeI and NaID doublet lines noticeable changes weren't observed. The further spectra of this star are observed between 21.06.2014 and 09.08.2014. In the spectra observed on 21.06 – 09.08.2014 dates the radial velocity of H$_\alpha$ and H$_\beta$ changed on average on ±4 km/s. But in the structure of profiles of these lines, and also in values of the radial velocities of HeI and NaID doublet lines, strong changes aren't revealed.

Table 2: Results of measurements of spectral parameters of lines HeI, and NaID

Date	HD21389							
	HeI (λ5876 Å)				NaI D1		NaI D2	
	Vr km/s	W Å	Δλ$_{1/2}$ Å	r$_v$	Vr km/s	W Å	Vr km/s	W Å
20.09.2005	-8.2	0.32	1.4	0.80	-8.3	0.58	-8.4	0.70
11.11.2006	-8.3	0.31	1.5	0.81	-10.8	0.58	-11.3	0.62
11.09.2014	-8.0	0.33	1.6	0.81	-10.6	0.61	-11.4	0.70

Date	HD187982								FeII λ4924 Å	FeII λ5018 Å	FeII λ5169 Å
	HeI (λ5876 Å)				NaI D1		NaI D2				
	Vr km/s	W Å	Δλ$_{1/2}$ Å	r$_v$	Vr km/s	W Å	Vr km/s	W Å	Vr km/s	Vr km/s	Vr km/s
01.09.2013	-1.0	0.22	1.3	0.86	-6.4	0.50	-8.0	0.51	-12.2	-10.4	-8.0
06.09.2013	-4.7	0.19	1.5	0.89	-12.1	0.52	-13.0	0.50	-19.3	-16.8	-13.5
02.10.2013	-2.3	0.17	1.3	0.89	-4.4	0.57	-6.5	0.58	-5.2	-7.0	-2.5
03.10.2013	-1.5	0.19	1.4	0.88	-2.5	0.58	-3.4	0.58	-8.3	-5.7	-2.3
21.06.2014	1.1	0.21	1.4	0.87	-10.1	0.56	-9.4	0.58	0.1	3.4	-5.6
04.07.2014	2.7	0.18	1.3	0.87	-8.1	0.50	-7.3	0.52	-0.4	1.0	-4.9
11.07.2014	4.1	0.21	1.5	0.87	-10.8	0.58	-9.5	0.59	-1.8	0.4	-7.8
18.07.2014	1.7	0.25	1.4	0.86	-8.7	0.59	-8.1	0.59	1.7	1.5	-6.2
24.07.2014	-0.4	0.21	1.4	0.88	-10.2	0.48	-9.7	0.50	-3.1	-0.5	-6.3
09.08.2014	2.6	0.21	1.4	0.87	-5.0	0.57	-4.5	0.59	5.1	-1.2	0.5
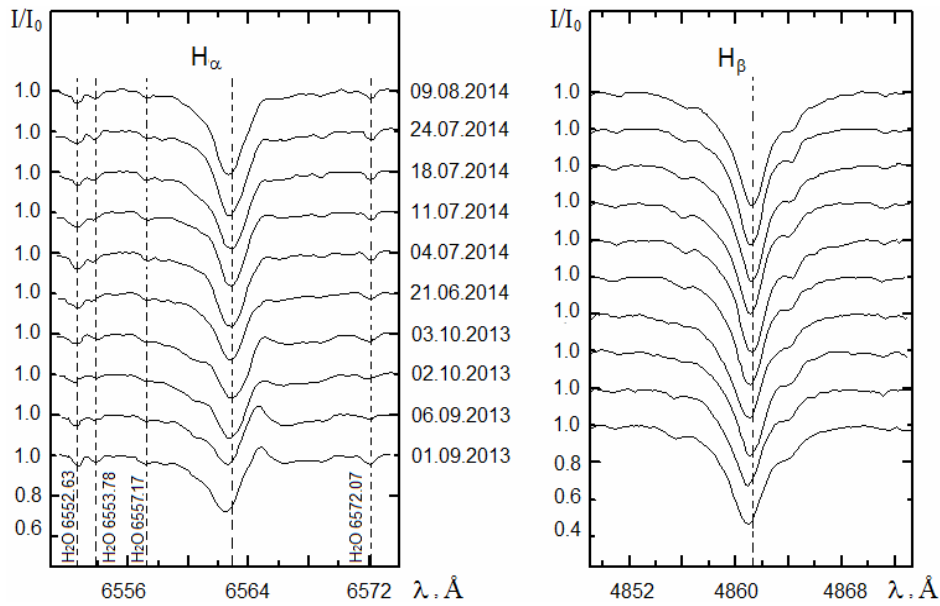
Figure 3: H$_\alpha$ and H$_\beta$ line profiles of the star HD187982 in 2013-2014.

On the other hand, changes of the radial velocity of the FeII line were also considered. Note that the FeII lines in the spectra of HD187982 were detailed investigated by White (1950), Abt (1957) and Hendry (1981). We tried to continue the works of these researchers and to compare the results. In Abt's (1957) work for the radial velocity it is found 7.7 days quasiperiodic change on the basis of the FeII lines (4508, 4515, 4520, 4522 Å). After Abt (1957) the measurements were carried out by Hendry (1981). He added to measurements of White (1950) and Abt's data and received same earlier found 7.7 days period.

On the basis of the spectrograms obtained by us, and also observational data of other authors taken from works White (1950), Abt (1957) and Hendry (1981) were constructed graphics of change of the radial velocity in the FeII lines. Our researches showed that the radial velocities of the FeII lines change with time. However, we didn't find periodicity in these changes. To reveal periodic processes additional observation materials is necessary.

NaI 5890 Å and 5896 Å. In the spectra of the stars HD 21389 and HD187982, except hydrogen and other lines, sodium doublet lines- NaI (5890 Å) and NaI (5896 Å) were also investigated.

It is known that generally the absorption of NaI (5890 Å and 5896 Å) lines are interstellar lines, i.e. are formed in the interstellar environment. Therefore the profiles of these lines have to be symmetric. Asymmetry of these profiles is argument in favor of the contribution of other sources to formation of these lines.

Investigation on optical spectra of these stars, and also other hot supergiants observed by us and other authors, specify that in formation of NaID doublet, except a star covers round these stars and the interstellar environment can make a contribution.

Unfortunately, as small resolution in the spectra, we couldn't reveal these components. However, on 11.11.2006 in the spectrum of HD 21389 in the profile of NaID doublet is observed asymmetry in violet wings of these lines. Therefore, for detection of asymmetry, we combined the red wing of these lines with a Gaussian

profile. In fig. 2 the dashed line showed combination of the red wing with a Gaussian profile.
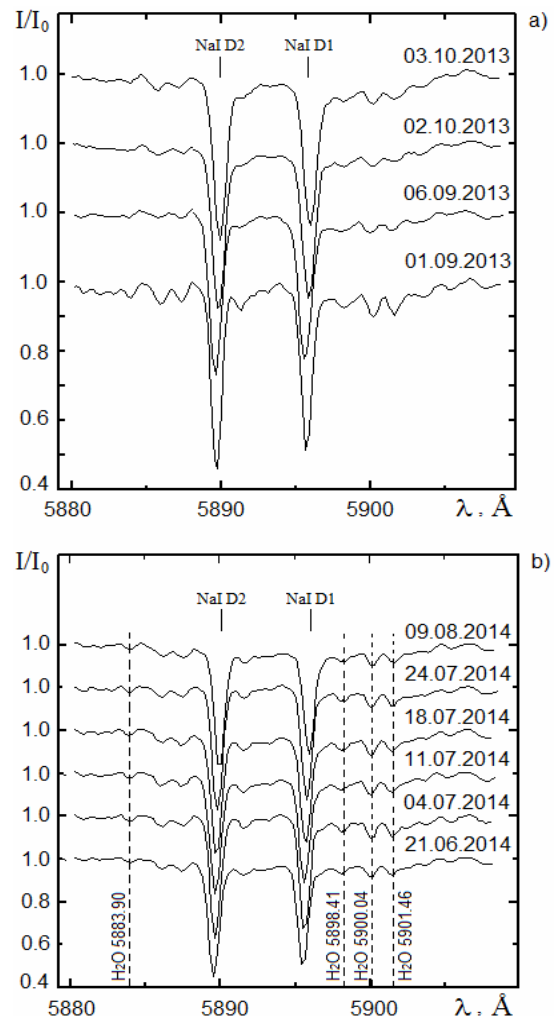
Figure 4: NaD line profiles of the star HD187982 in 2013-2014.

The radial velocities of studied lines are determined by combination of straight lines and mirror images of the specified lines of absorption in the level of the half-width Vr (R/2), and also Vr in the centers of the profiles. Laboratory lengths of waves (D2, D1) were accepted as 5889.953 Å and 5895.923 Å, respectively. The values of the radial velocities and equivalent width (W_λ) determined by us are given in table 2.

Apparently from table 2, in the spectra of HD187982 supergiant the equivalent width of the NaI (5890 Å) and NaI (5896 Å) lines determined by us significantly changes aren't observed. However, the radial velocities of these lines variability are observed.

In addition, only on 11.11.2006 in the spectra of the star HD 21389 the asymmetry is observed in the NaID doublet line. Appearance and disappearance of asymmetry in the profile of NaID doublet and formation of the H_α line type inverse P Cyg happens synchronously in an active phase of the atmosphere of HD 21389 (fig. 1, 2).

3. Discussion

The profile of the H_α line observed in the atmosphere of the HD21389 and HD187982 supergiants indicates variable structure. The analysis of the absorption and emission components of the H_α line shows that the radial velocities change with time. Our investigation shows that all the measured parameters of H_β line and its radial velocities vary with time.

It is known that the H_α and H_β lines form in the upper layers of the stellar atmosphere, in the region of generation of stellar wind (De Jager, 1984). The variable wind and its accelerated motion in supergiants is caused by the strong flux of radiation from the star. Outer atmospheres of supergiant stars are exposed to more intense changes than internal.

Thus, the stellar radiation flux and the variable stellar wind lead to corresponding changes in the outer layers of the atmosphere and the star envelope.

As a result, we observe variable absorption and emission components of different forms of the H_α line P Cyg-profile of the star HD21389 and HD187982.

As is known, the variable stellar wind in the supergiants is caused by the pulsation (Cox, 1983). If these changes in the stars HD21389 and HD187982 are associated with the pulsation, they should occur periodically. The amount of obtained data and their inconsistency in observation time does not make it possible to make such far-reaching conclusions in this paper.

Therefore, additional systematic spectral and photometric observations of these stars are planned at the Shamakhy Astrophysical Observatory in the near future.

In addition, as it is noted above, asymmetry of interstellar lines of NaI 5890 (D2) and NaI 5896 (D1) in the spectra of the supergiant HD 21389 (fig.2) is found. In all the specified lines an echelle spectrograms asymmetry observed by us it is found only in violet wings of these lines and only 11.11.2006, when absorption profiles the H_α line is observed in the form of inverse P Cyg. However, in 20.09.2005 and 11.09.2014 the asymmetry in the profile of a NaID doublet isn't observed. From fig. 1 it

is visible that in 20.09.2005 in the spectra of HD21389 supergiant the profile of the H_α line is observed in pure absorption, and in 11.09.2014 – normal P Cyg profile when on the red wing of H_α line very weak emission component is observed (fig. 1).

But the asymmetry in the profiles of NaID doublet isn't found by us in the spectra of other supergiant HD187982. This observational fact is additional argument in favor of reality of the asymmetry of the studied NaI 5890 (D2) and NaI 5896 (D1) lines revealed by us in the spectra of the star HD 21389.

We assume that the asymmetry of the specified absorption lines in the spectra of supergiant HD21389 found by us and change of the profile of H_α line are formed under the influence of the general mechanism which might be responsible for the observed variation is the growth of the envelope of the star with a following ejection of matter.

4. Conclusions

1. The absorption profile of the H_α line in the spectra of the star HD21389 depending on a phase of instability of the star atmosphere has difficult structure. In an active phase this line has inverse P Cyg profile. On the red and violet wings of the profile appear and disappear emission components. All measured parameters of the H_α line show variability. It is supposed that variability of the profiles, radial velocity and other parameters are connected with each other and also these changes may be a manifestation of complex motions in the atmosphere of HD21389.

2. Appearance and disappearance of asymmetry in the profile of NaID doublet and formation of the H_α line type inverse P Cyg occurs synchronously in an active phase of the atmosphere of HD 21389. We assume that these changes are formed under the influence of the general mechanism which might be responsible for the observed variation is the growth of the envelope of the star with a following ejection of matter.

3. Our researches showed that the values of radial velocity of the FeII lines change with time. However, we found no correlation of these changes with the period of 7.7 days found by earlier authors (Abt, 1957, Hendry, 1981).

These results can be used for the further analysis of a chemical composition and determination of fundamental parameters of the atmosphere, and also for creation of the theoretical model of this star.

References

Achmad L., Lamers H.J.G.L.M., L.Pasquini L.: 1997, *Astronomy & Astrophysics*, **320**, 196.
Burki G.: 1978, *Astronomy & Astrophysics*, **65**, 357.
Cox J.P.: 1983, *Theory of Stellar Pulsation*, Mir, Moscow.
De Jager C.: 1984, *The Brightest Stars,* Mir, Moscow.
De Jager C., Nieuwenhuijzen H., van der Hucht K.A.: 1988, *Astronomy & Astrophysics, Suppl. Ser.,* **72**, 259.

Denizman L., Hack M.: 1988, *Astronomy & Astrophysics*, **75**, 79.

Evans C.J., Howarth Ian D.: 2003, *MNRAS*, **345**, 1223.

Galazutdinov G.A.: 1992, *Prepr. SAO RAS*, **92**, 2.

Galazutdinov G.A., Manico G., Pirronello V., Krelowski J.: 2004, *MNRAS*, **355**, 169.

Gray R.O., Garisson R.F.: 1987, *Astrophysical Journal, Suppl. Ser.*, **65**, 581.

Helmut A.A., Nidia I.Morrell.: 1995, *Astrophysical Journal, Suppl. Ser.*, **99,** 135.

Helmut A.A.: 1957, *Astrophysical Journal*, **126**, 138.

Hendry E.M.: 1981, *The Astronomical Journal*, **86**, 1540.

Mikailov Kh.M., Khalilov V.M., Alekberov I.A.: 2005, *Tsirk. ShAO*, **109**, 21.

Przybilla N., Firnstein M., Nieva M.F., Meynet G., Maeder A.: 2010, *Astronomy & Astrophysics*, **517**, 1.

Rzaev A.Kh., Zeinalov S.K., Chentsov E.L.: 1989, *Kinematics and Physics of Selectial Bodies*, **5**, 81.

Snell R.L., Vanden Bout P.A.: 1981, *Astrophysical Journal*, **244**, 844.

Straizys V., Laugalys V.: 2007, *Baltic Atronomy*, **16**, 167.

Takeda Y., Takada-Hidai M.: 2000, *Japan Astronomical Society*, **52**, 113.

Takeda Y., Takada-Hidai M.: 1998, *Japan Astronomical Society*, **50**, 629.

Talavera A., de Castro A.I.Gomez.: 1987, *Astronomy & Astrophysics*, **181**, 300.

Verdugo E., Talavera A., de Castro A.I.Gomez.: 1999, *Astronomy & Astrophysics*, **346**, 819.

Verdugo E., Talavera A., de Castro A.I.Gomez.: 1999, *Astronomy & Astrophysics*, **137**, 351.

Weaver Wm. B., Torres-Dodgen Ana V.: 1995, *Astrophysical Journal*, **446**, 300.

White W.C.: 1950, *Astrophysical Journal*, **112**, 559.

Zeinalov S.K., Rzaev A.Kh.: 1990, *Astrophysics and Space Science*, **172**, 211.

Zeinalov S.K., Rzaev A.Kh.: 1990, *Astrophysics and Space Science*, **172**, 217.

Zeinalov S.K.: 1997, *Doctoral dissertation, The non-stationary phenomena in the atmosphere of O, B, A, F supergiants*, Tbilisi.

Zeinalov S.K.: 2003, *Tsirk. ShAO*, **106**, 22.

Zvereva E.B., Zeinalov S.K., Chentsov E.L.: 1984, *Izv. Spets. Astrophys. Obs.* **18**, 29.

THE ELEMENTS OF THE BASIC PHOTOMETRICAL CIRCLES ON THE SURFACE OF THE SPHERICAL PLANET AND DETERMINATION OF THEIR PLANETOCENTRIC POSITIONS

V.V. Mikhalchuk

Odessa National Maritime Academy,
Odessa, Ukraine, *vmihalchuk@mail.ru*

ABSTRACT. Formulae for determination of planetocentric positions of the basic photometrical circles on the surface of the spherical planet (the equator of intensity, an orthographic limb and orthographic terminator) from the elements of these circles specified to conditions of illumination of its visible disk are obtained. The planetocentric positions of the basic photometrical circles on visible disks of terrestrial planets from their physical ephemerides are calculated.

Key words: planets, phase, physical ephemerides, planetocentric coordinates.

1. Introduction

At photometrical observations of the surface of planets of the Solar system and their natural satellites there is a problem of determination of the position of features of the local albedo on images of their visible disks. For terrestrial planets which shape can be counted as a first approximation spherical, this problem becomes complicated influence of the phase. It is observed when the geometric planetary disk is illuminated by the Sun not completely, i.e. the phase angle Φ is distinct from zero. Thus the phase of the planet is considered in an orthographic approximation, i.e. it is supposed, that the Sun is the point source of the light, which is infinitely removed from the planet, hence, the orthographic terminator is the boundary of the illuminated part of the visible planetary disk.

At ground-based and near-earth observations it is possible to neglect radius of the planet in comparison with its geocentric distance. In this case we suppose, that the Earth is infinitely removed from the planet, therefore the initial image of the visible planetary disk represents an orthographic projection of its surface to the plane of the sky.

In contributions (Mikhalchuk, 2001b; Mikhalchuk, 2004a; Mikhalchuk, 2004b; Mikhalchuk, 2004c; Mikhalchuk, 2005a; Mikhalchuk, 2005b; Mikhalchuk, 2007a; Mikhalchuk, 2007b; Mikhalchuk, 2008a;

Mikhalchuk, 2008b) the rotating planetocentric coordinate system with a direction of the calculation of the longitude as in planetographic coordinate system RGS (Sveshnikov, 2004) was considered. This coordinate system also is applied in the present contribution. The base plane of this system is the plane of the equator of the planet, and the position of each point of planet's surface is set by means of the planetocentric latitude b and longitude l. At ground-based and near-earth observations of the planet its visible disk is observed in the orthographic projection, therefore the given coordinate system is observed also in the orthographic projection.

In contributions (Mikhalchuk, 2004a; Mikhalchuk, 2004b; Mikhalchuk, 2004c; Mikhalchuk, 2005a; Mikhalchuk, 2005b; Mikhalchuk, 2007a; Mikhalchuk, 2007b; Mikhalchuk, 2008a; Mikhalchuk, 2008b; Mikhalchuk, 2008c) for determination of planetocentric coordinates of the albedo features the auxiliary coordinate system, which also can be applied for photometrical observations, is entered. She the same, as photometric coordinate system, is nonrotating and is linked to equator of intensity, but differs from it by choice of the prime photometric meridian and the direction of the calculation of longitudes.

The position of some photometrical circles on the surface of the spherical planet in an orthographic approximation - the basic photometric meridians in the auxiliary coordinate system, their properties and connection with conditions of illumination of the planet were probed in contributions (Mikhalchuk, 2008b; Mikhalchuk, 2008c). It is shown, as conditions of illumination of the planet determine the shape of the illuminated part of its visible disk and the position of this part on the visible disk. However for binding the illuminated part of the visible planetary disk to the features of the local albedo observed on its surface, it is necessary to attract the planetocentric coordinate system. In turn, the conditions of illumination of the planet set positions of the basic photometrical circles on its surface in the planetocentric coordinate system

what are the following great circles: equator of intensity, an orthographic terminator and an orthographic limb.

Thus, there is a necessity for a realization a transition from the auxiliary coordinate system to the planetocentric coordinate system for determination of positions of the basic photometrical circles on the surface of the planet. The purpose of the present contribution is determination of elements of the basic photometrical circles, which single-valued setting their position in the planetocentric coordinate system, and deriving of the expressions bundling these elements with conditions of illumination of the planet.

2. The Basic Photometrical Circles on the Surface of the Planet

The basic photometrical circles are always clearly designated on the visible planetary disk owing to character of her illumination intensity. They determine the shape of an illuminated part of the visible disk and her position on the visible disk. The shape of an illuminated part of the visible planetary disc is determined by the phase, i.e. depends on the phase angle. The position of an illuminated part on the visible planetary disk relative to the circle of declinations is determined by an angle Q, which is the angle of the position of the point of the least illumination of the disk on the geocentric celestial sphere, and relative to the projection of the planet's axis of rotation to the geocentric picture plane is determined by an value $P - Q$, where P is the angle of the position of the planet's axis of rotation on the geocentric celestial sphere.

Let's consider the basic photometrical circles on surface of the spherical planet and their geometric characteristics in the planetocentric coordinate system. Let the visible disk of the spherical planet illuminated by the Sun under the arbitrary phase angle Φ (Figure 1). Let A is the north pole of the planet and B is the north orthographic cusp of the disk. The equator of the planet is intersected with its orthographic limb in points G and G'. The basic points of the diameter of intensity: O is the geometric center of the planetary disk (the subterral point), E is the subsolar point (the pole of illumination), L is the pole of phase, F is the point of the least illumination of the disk and T is the visible center of orthographic terminator.

The basic photometrical circles on the surface of the visible planetary disk: equator of intensity, an orthographic terminator and an orthographic limb. All of them are the great circles having the following geometrical meaning:
- for the observer, which is on equator of intensity, centers of the Earth and the Sun are always located on one vertical;
- for the observer, which is on an orthographic ter-
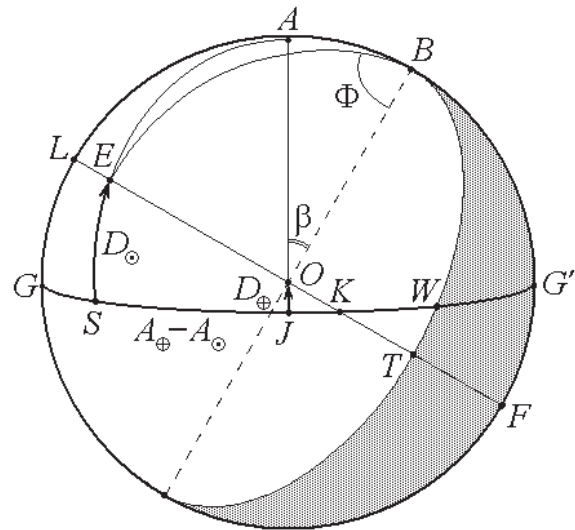
Figure 1: The basic photometrical circles on the visible disk of the spherical planet

minator, the center of the Sun always is in a horizon plane;
- for the observer, which is on an orthographic limb, the center of the Earth always is in a horizon plane.

As the base plane of the planetocentric coordinate system is the plane of equator of the planet planetocentric positions of all remaining photometrical circles should be determined concerning this plane. In the planetocentric coordinate system the basic reference point is the subterral point having planetocentric coordinates l_p and b_p, where l_p is longitude of the central meridian passing through the center of the geometric disk is measured from some zero meridian westward of the planet; b_p is the latitude of the center of the geometric disk is equal to the planetocentric declination of the Earth $D_\oplus$. The position of each photometrical circle in this coordinate system is single-valued set by two elements: the planetocentric longitude l_Ω of his ascending node on equator of the planet and the inclination i of his plane to the plane of the planet's equator. The ascending node of the photometrical circle on equator of the planet is meant as the point of his intersection with equator of the planet ($b = 0$), in the neighbourhood of that for any point of this circle carry out condition $\dfrac{db}{dl} > 0$.

3. The connection of planetocentric positions of the basic photometrical circles on the surface of the planet with conditions of its illumination

The equation of the photometrical circle in the planetocentric coordinate system has the form:

$$\tan b = \tan i \sin(l - l_\Omega). \tag{1}$$

Let P and Q are angles of the position of the planet's axis of rotation and the point of the least illumination of the disk on geocentric celestial sphere accordingly (Sveshnikov, 2004). We shall consider angle β between the projection of the axis of rotation of the planet on the plane of the sky and the line of cusps (Figure 1), connected with angles P and Q by the following expression (Mikhalchuk, 2004a):

$$\beta = \mp 90° + (P - Q). \tag{2}$$

The choice of a sign in the formula (2) is carried out by following rule (Mikhalchuk, 2004a): the upper sign concerns to the case, when $\sin(P - Q) > 0$, and the lower sign - when $\sin(P - Q) < 0$. This convention of signs is spread and further, to all subsequent expressions.

Then, using auxiliary angle β, it is possible to show, that

$$l_\Omega = l_p + u, \tag{3}$$

where the angle u and the inclination i of the plane of the photometrical circle to the plane of equator of the planet are determined from following expressions.

For the equator of intensity

$$\cos i = \cos D_\oplus |\sin(P - Q)|. \tag{4}$$

The point K of intersection of equator of intensity with equator of the planet, is located on its visible disk, will be called as the defining point of the equator of intensity. It is possible to show, that its planetocentric longitude l_K is expressed by the formula

$$\tan(l_K - l_p) = \sin D_\oplus \tan(P - Q). \tag{5}$$

The point K can prove to be as the ascending node of the equator of intensity on equator of the planet and as the descending node. To find longitude of the ascending node of the equator of intensity by formula (3), it is necessary to make use of expression (5), supposing what $u = l_K - l_p$, if $\tan(P - Q) < 0$. If $\tan(P - Q) > 0$ then the found value of the angle u ought to be changed on 180°.

For the orthographic terminator

$$i = 90° - |D_\odot|, \tag{6}$$

where $D_\odot$ is the planetocentric declination of the Sun.

The point W of intersection of orthographic terminator with equator of the planet, is located on its visible disk, will be called as the defining point of the orthographic terminator. It is possible to show, that its planetocentric longitude l_W is expressed by the formula

$$l_W - l_p = (A_\oplus - A_\odot) \mp 90°, \tag{7}$$

where $A_\oplus - A_\odot$ is the difference of planetocentric right ascensions of the Earth and the Sun accordingly.

The point W can prove to be as the ascending node of the orthographic terminator on equator of the planet and as the descending node. To find longitude of the ascending node of the orthographic terminator by formula (3), it is necessary to make use of expression (7), supposing what $u = l_W - l_p$, if $D_\odot > 0$. If $D_\odot < 0$ then the found value of the angle u ought to be changed on 180°.

For the orthographic limb

$$i = 90° - |D_\oplus|. \tag{8}$$

$$u = 90°. \tag{9}$$

In order to remove indeterminacy in calculation of longitude of the ascending node of the orthographic limb on equator of the planet, at $D_\oplus < 0$ the value of the angle u, found of the formula (9), ought to be changed on 180°.

Knowing elements l_Ω and i of the basic photometrical circles, it is possible to determine single-valued the planetocentric position of each of them on the surface of the planet, and from the equation (1) to find the planetocentric latitude b of his any point for the given planetocentric longitude l.

4. The planetocentric positions of the basic photometrical circles on the surface of the terrestrial planets

Let's consider the example of determination of planetocentric positions of the basic photometrical circles on the surface of the Mercury, Venus and Mars from their physical ephemerides on 0^h UT on January 8, 2004 (Glebova, 2003), which are listed in Table 1.

The planetocentric declination of the Sun for Mercury is equal zero, hence, the Sun is located in the plane of his equator. Then from the formula (6) follows, that for an orthographic terminator of Mercury $i = 90°$.

The elements of the basic photometrical circles, which are calculated by the formulae (3), (4), (6), (8) and (9), are submitted in Table 2.

The results of calculation, which are listed in Table 2, are completely accorded with the physical ephemerides of planets from Table 1.

Table 1: The physical ephemerides of planets on 0^h UT January 8, 2004

Planet	P	$D_\oplus$	$A_\oplus - A_\odot$	$D_\odot$	Φ	Q	l_p
Mercury	$7°.08$	$-7°.13$	$+105°.32$	$0°.00$	$105°.2$	$279°.03$	$261°.81$
Venus	342.18	+1.29	-50.70	+1.88	50.68	73.55	352.94
Mars	327.12	-25.12	-41.84	-12.38	41.42	67.12	154.90

Table 2: The elements of the basic photometrical circles of planets on 0^h UT January 8, 2004

Planet	Equator of intensity		Terminator		Limb	
	i	l_Ω	i	l_Ω	i	l_Ω
Mercury	$7°.39$	$7°.15$	$90°$	$277°.13$	$82°.87$	$171°.81$
Venus	1.88	216.21	88.12	32.24	88.71	82.94
Mars	26.92	267.46	77.62	23.06	64.88	64.90

The elements of the basic photometrical circles of planets allow compiling the equations of these circles in the planetocentric coordinate system, to build them on the surface of the planet and to determine the planetocentric coordinates of each point of the given circle.

By means of the program's batch (Mikhalchuk, 2001a) computer simulation of projection of the basic photometrical circles of planets on the plane of the sky was produced. The obtained computer models completely are accorded with the images of circles, which built on their elements from Table 2.

5. Conclusion

The main results obtained in this contribution:

1. The basic photometrical circles on the surface of the spherical planet are considered. The geometric meaning of these circles for the observer, which is on its, is shown.

2. The formulae, which allow calculating the elements of the basic photometrical circles on the surface of the spherical planet, are obtained.

3. The elements of the basic photometrical circles on the planet's surface depend on its orientation concerning the Earth and the Sun, and also are determined by conditions of illumination of the visible planetary disk.

References

Glebova N.I., Ed.: 2003, *Astronomical Year-Book for 2004.* St. Petersburg: IPA RAN.

Mikhalchuk V.V.: 2001a, *Odessa Astron. Publ.,* **14**, 261-264.

Mikhalchuk V.V.: 2001b, *Astron. Vestn.,* **35**, N 1, 89-96.

Mikhalchuk V.V.: 2004a, *Kinematics and Physics of Celestial Bodies,* **20**, N 1, 76-92.

Mikhalchuk V.V.: 2004b, *Abstract book of the Conf. VAK-2004 "Horizons of the Universe". Transact. SAI,* **75**, *Moscow (Russia)*, 234.

Mikhalchuk V.V.: 2004c, *Odessa Astron. Publ.,* **17**, 54-57.

Mikhalchuk V.V.: 2005a, *Kinematics and Physics of Celestial Bodies, Suppl. Ser.,* **5**, 557-560.

Mikhalchuk V.V.: 2005b, *Proc. VIII Conf. of Astron. Soc. and Int. Symp. "Astronomy-2005: Situation and Development Prospects". Transact. SAI,* **78**, *Moscow (Russia)*, 13.

Mikhalchuk V.V.: 2007a, *Odessa Astron. Publ.,* **20**, Part 2, 76-80.

Mikhalchuk V.V.: 2007b, *Transact. of the All-Russia Astronomical Conf. VAK-2007. Kazan (Russia),* 49-51.

Mikhalchuk V.V.: 2008a, *Radiophys. and radioastron.,* **13**, N 3, 134-139.

Mikhalchuk V.V.: 2008b, *Program and Abstracts of the VIII-th G.Gamow's Odessa Astronomical Summer School "Astronomy and beyond: Astrophysics, Radioastronomy, Cosmology and Astrobiology". Odessa (Ukraine)*, 21.

Mikhalchuk V.V.: 2008c, *Abstract Book of the International Conf. "The Solar System Bodies: from Optics to Geology". Kharkiv (Ukraine)*, 89-90.

Sveshnikov M.L.: 2004, *Tr. IPA RAN,* **10**: *Ephemeris Astronomy* /ed. Finkel'shtein A.M., St. Petersburg: IPA RAN, 349-375.

THE SULPHUR ABUNDANCE BEHAVIOUR IN THE GALACTIC DISC STARS

T. V. Mishenina, O. P. Paramonova

Astronomical Observatory, Odessa National University
Shevchenko Park, Odessa 65014, Ukraine
tmishenina@ukr.net

ABSTRACT. The sulphur abundances in the atmospheres of the F-G-K-type dwarf stars that belong to the thin and thick disc populations (in the metallicity range $-1.0 <$ [Fe/H] < 0.3) were determined. The observations were conducted using the 1.93 m telescope at Observatoire de Haute-Provence (OHP, France) equipped with the echelle-type spectrograph ELODIE (R = 40 000). The abundances were derived under the LTE approximation; the synthetic spectrum for the sulphur lines in the region of 6743-6762 ÅÅ was computed accounting for the hyperfine structure. The correlation between the abundances of some elements and metallicity [Fe/H] in the Galactic thin and thick disc stars was analyzed. To discuss the sources of sulphur production, the comparison between the sulphur abundance trend and current theoretical computations of the Galactic chemical evolution was made.

Key words: Stars: abundance – Stars: late-type

1. Introduction

The sulphur abundance in the Galactic disc can be a good diagnostic tool to determine the sources and conditions of the production of α-elements (e.g. Limongi & Chieffi, 2003).

The early studies of the sulphur abundance (Wallerstein & Conti 1964; Clegg et al. 1981; Francois 1988) reported a noticeable scatter of values with a potential trend on metallicity which is typical for α-elements. The further research in the sulphur abundance determination proved the presence of such a trend and drew attention to a series of issues, primarily to the presence of deviations from the LTE (e.g. Takada-Hidai et al., 2002) and complexity of the sulphur line measurements in the visible spectrum (Caffau et al., 2005a). In recent decades, an evident attention has been given to the sulphur abundance investigation in various space objects. For instance, the sulphur abundance was determined in metal-poor stars (Takada-Hidai et al., 2001; Israelian & Rebolo, 2001; Takeda et al., 2005; Ryde & Lambert, 2004; etc.); in metal-rich stars (Chen et al., 2002); in stars with planets (Ecuvillon et al. 2004); in the stars in globular and open clusters (Caffau et al., 2005b; Sbordone et al., 2009; Caffau et al., 2014; etc.), and in the disc's giants (Matrozis et al., 2013). The last study highlighted the necessity of applying of a uniform method for determination of atmospheric parameters, which the sulphur abundance is sensitive to.

The elements resulted from the α-particle capture – the so-called α-elements – are produced in massive core-collapse supernovae (CCSN) both at the pre-supernova stage and in the processes of explosive nucleosynthesis. According to Limongi & Chieffi (2003), Mg is produced by the carbon-burning process in the convective regions while the oxygen-burning process yields Si, S and Ca. In the explosive nucleosynthesis Mg is produced in the explosive neon and carbon burning processes (Thielemann & Arnett, 1985) while Si, S and Ca are produced in the explosive oxygen burning (Thielemann & Arnett, 1985; Woosley & Weaver, 1995) with the yield of elements depending on different factors from the relevant reaction cross-sections to the treatment of semi-convection. Therefore, due to the distinction in the production of Mg and Si, S and Ca, the difference in behaviour of the Mg abundance and those of Si, S and Ca can be expected. Iron and iron-peak elements result from the equilibrium process with at least two sources of production, such as CCSN and less massive supernovae SNe Ia (Timmes, Woosley & Weaver, 1995).

To determine the sulphur production sources, Chen et al. (2002) made a comparison between the sulphur and silicon abundances in the disc stars. They found a correlation between [S/H] and [Si/H], as well as reported the absence of any dependence of the S and Si abundances on the metallicity at [Fe/H] > -1.0. The obtained results are indicative of the same nucleosynthetic origin for the two elements and sustain existing models of the chemical evolution of the Galactic disc (Goswami & Prantzos (2000), Timmes et al. (1995).In these models, sulphur is synthesised predominantly by the oxygen burning in massive stars, and is ejected into the interstellar medium in the Type II supernovae explosions).

Further studies by Nissen et al. (2004), including the halo stars, showed that for the disc stars with [Fe/H] > -1, [S/Fe] decreases with increasing [Fe/H]. Hence, sulphur behaves like other typical α-capture elements, Mg, Si and Ca. In the meantime, it is reported for zinc, which is an iron-peak element, that there is some evidence for a small systematic Zn overabundance ([Zn/Fe] $\sim$ +0.1) among metal-poor disc stars and halo stars with [Fe/H] < -2.0.

On the other hand, the comparison between the abundance of sulphur as a volatile element and refractory element abundance can reflect one of the hypotheses of the planets' existence around stars (e.g. Ecuvillon et al., 2004).

The investigation of planet-hosting stars revealed that those stars are on average metal richer than normal stars of the disc (e.g. Gonzalez, 1997; Santos et al., 2001). It was assumed on the one of the hypotheses (Gonzalez, 1997) that it is accreted materials (rocky planetesimals) which are responsible for the metal overabundance while volatile elements (with low condensation temperatures) should be deficient due to high temperatures of circumstellar matter. Hence, the self-enrichment scenario should result in relative overabundance of refractory materials, such as α-elements Si, Mg, Ca, Ti and iron-group elements comparing to volatile elements, such as CNO, S and Zn. In further studies, any significant difference in behaviour of the abundances of those elements for normal and planet-hosting stars was not found (e.g. Santos et al., 2000; Gonzalez et al., 2001; Ecuvillon et al., 2004). That could be due to the small number of stars, for which the determination of parameters and elemental abundances was performed by a uniform method; and that highlighted the importance of elemental abundance determination for a larger number of stars with and without known planetary systems. The alternative was the hypothesis of increased metal enrichment of protoplanetary (pre-stellar) cloud (Santos et al., 2000; 2001). That hypothesis did not state any differences in the abundances of refractory metals and volatile elements between planet-hosting and normal stars.

Thus, the sulphur abundance is a good test for 1) the nucleosynthesis of α-elements (S, Si and Ca vs. Mg); and 2) the self-enrichment hypothesis in the case of planet-hosting stars (S and Zn vs. Si, Mg and Ca).

The aim of this study is 1) to determine the sulphur abundance for a large set of the disc's stars, for which reliable atmospheric parameters and abundances of a series of elements had been obtained earlier; 2) to compare the sulphur, silicon and magnesium behaviour to study dissimilar conditions of the synthesis of α-elements; 3) to compare the behaviour of volatile elements, namely sulphur and zinc, with that one of refractory materials for normal and planet-hosting stars (or for the stars with [Fe/H]>–0.5 dex) to estimate the potential of demonstration or influence of the chemical composition on planet-hosting stars.

2. Observations, spectra processing and parameter determination

The present paper continues a series of earlier studies of the Galactic thick and thin disc and is based on the spectral material obtained at Observatoire de Haute-Provence (France). The spectra of 175 stars were obtained in the wavelength region 4400-6800 ÅÅ with S/N about 100-350 using the 1.93 m telescope at the Observatoire de Haute-Provence (OHP, France), equipped with the echelle-type spectrograph ELODIE (Barrane et al., 1996) with the resolving power R = 42000. The primary processing of images is available online immediately after the exposure. The spectra have been treated to correct the blaze efficiency, cosmic and telluric lines as per Katz et al. 1998.The next processing of the studied spectra (including the continuous spectrum level installation, the construction of the dispersion curve, the measurement of

equivalent widths EW, etc.) was performed with the DECH20 software package (Galazutdinov 1992).

The parameters of the investigated stars were taken from Mishenina et al. (2013). The effective temperatures Teff were estimated using the line-depth ratio method (Kovtyukh et al., 2004). The surface gravities lg g were computed by two methods, namely the iron ionization balance and the parallax. The results of application of these two methods are in good agreement. The microturbulent velocity Vt was derived considering that the iron abundance log A(Fe) obtained from the given Fe I line was not correlated with the equivalent width EW of that line. The iron abundance determined from the iron Fe I lines was taken as the metallicity [Fe/H].

3. The sulphur abundance determination

The sulphur abundances were obtained under the LTE approximations by the synthetic spectrum method accounting for the hyperfine structure (HFS) and the oscillator strengths of lines from Korotin (2009). The Kurucz atmospheric models (Kurucz, 1993) and a new version of the STARSP code by Tsymbal (1996) were applied. We used the sulphur lines in the region of 6743-6762 ÅÅ available in our spectra. The adopted sulphur solar abundance is $\log A(S)_\odot = 4.84$ in the scale where $\log A(H) = 12.00$. The NLTE corrections for those lines are small and do not exceed 0.1 dex (Korotin, 2009). An example of the fitting of the computed synthetic and observed spectrum in the sulphur line region is shown in Fig. 1.
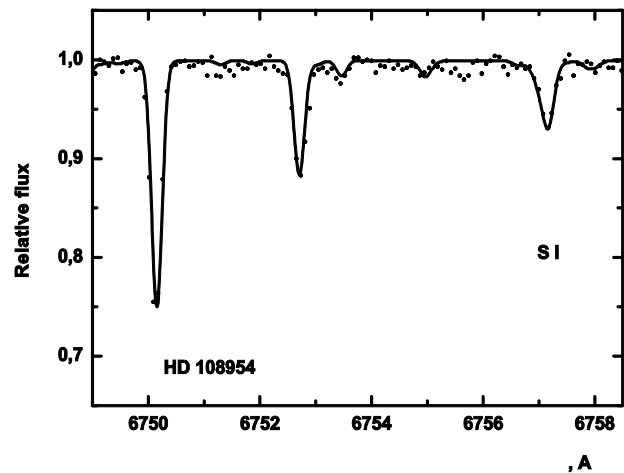
Figure 1: An example of the fitting of the observed and synthetic spectrum in the sulphur line region

4. The comparison with the results of other authors

The comparison of the data obtained by us with those from the studies by Chen et al. (2002) for one common star HD 9826 and Ecuvillon et al. (2004) for 12 common stars, including HD 9826, was made.

Table 1: The comparison of parameters and S abundance in star HD 9826

Teff	log g	[Fe/H]	[S/Fe]	References
6119	4.12	0.12	0.04	Chen et al. (2002)
6212	4.26	0.13	−0.33	Ecuvillon et al. (2004)
6074	4.00	0.10	−0.12	Our study

For star HD 9826 (50 And), we can see (in Table 1) that our determined parameters and sulphur abundances are in good agreement with the results by Chen et al. (2004) within the determination errors while the comparison with the data obtained by Ecuvillon et al. (2004) shows the difference in temperature and sulphur abundance. At that, the data for 12 common stars received in the same study (Ecuvillon et al. 2004, Ec04) are in good agreement with our data:

$$\Delta \text{Teff}_{(our-Ec04)} = -4 \pm 73 \text{ K}, \quad \Delta \log g_{(our-Ec04)} = 0.11 \pm 0.12,$$
$$\Delta[\text{Fe/H}]_{(our-Ec04)} = 0.05 \pm 0.04, \quad \Delta[\text{S/Fe}]_{(our-Ec04)} = -0.03 \pm 0.11.$$

Therefore, we can conclude that our determinations are in good agreement with those in the literature within the determination errors.

To calculate errors in the sulphur abundance determinations, we supposed the accuracy of effective temperature determination is $\delta \text{Teff} = \pm 100$ K, the surface gravity log g – $\delta \log g = \pm 0.2$ dex, $\delta Vt = \pm 0.2$ km/s ; and also the uncertainty of 0.03 dex in the computed spectrum fitting (Table 2). These estimations of the accuracy in the parameter determination and spectral fitting are in good correspondence with those from Mishenina et al. (2013), as well as with our estimations given above.

For sulphur the variation in parameters by $\delta \text{Teff} = -100$ K, $\delta \log g = +0.2$, $\delta Vt = +0.2$ km/s is given in columns 1, 2 and 3, respectively. The total error is given in column 4 supposing that the uncertainty in the spectrum fitting is 0.03 dex.

Table 2: Influence of stellar parameters on S abundance determination

El	1	2	3	4
[S/H]	−0.11	−0.03	0.02	0.12

As can be seen from Table 2, the total error is about 0.12 dex.

5. Results and discussion

Sulphur is an important element which can serve as a good test of the nucleosynthesis theory and various conditions of the synthesis of α-elements, on the one hand, and potentially different enrichment of chemical elements in stars with and without planets, on the other hand.

To test the nucleosynthesis theories, let us make a comparison between the sulphur behaviour in stars of the Galactic thin and thick discs (Fig. 2) and the Si and Mg behaviour in those stars (see Fig. 5 in Mishenina et al., 2013). The probability of each star's belonging to the thin or thick discs was determined by the method of Soubiran & Girard (2005).
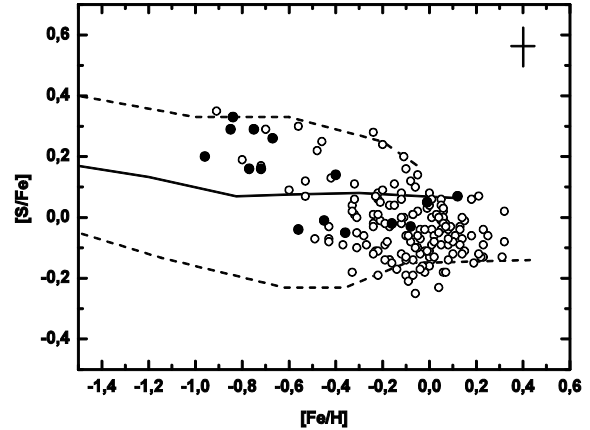
Figure 2: The correlation between the sulphur abundance and metallicity in the stars of the thin (marked with blank circles) and thick (marked with solid circles) discs. The comparison with the computations made by the chemical evolution models (Timmes et al., 1995) with twofold iron yield in supernovae SN Ia.

As is seen from these figures, there is a correlation between all those α-process elements and metallicity: the elemental abundances are higher at lower metallicities. At that, the observed correlations for sulphur and silicon are practically similar with those for magnesium. That can be a good argument in favour of modern computations of nucleosynthesis where core-collapse supernovae (CCSN) are reckoned as the main contributors of α-elements and are responsible for the production of magnesium, sulphur and silicon. The obtained trends are similar within our determination errors and do not enable to distinguish the behaviour of magnesium, sulphur and silicon. Hence, based on our data, we can not discuss the observed demonstration of different behaviour of the carbon combustion products, on the one hand, and oxygen and neon, on the other hand, in massive supernovae.

It is also interesting to compare the obtained sulphur abundances with the computations of the Galactic chemical evolution. Fig. 2 shows the comparison with the models by Timmes et al. (1995) with different iron yield in supernovae SN Ia. In general, the computations specify the observation data. Therefore, we can substantiate that the adopted characteristic parameters of the chemical evolution (the Galaxy structure, the star formation and mass functions) and yield of elements (in our case, the sulphur production in the neon and oxygen burning processes) correspond to the observed reality.

To estimate the effects of the planet formation on the chemical composition of a star, we considered the abundances of refractory metals (Mg and Ni) and volatile elements (S and Zn). The Mg, Ni and Zn abundances were adopted from our earlier studies of the dwarfs with temperatures in the range of 5500 − 6200 K and metallicities from -0.5 dex. The metallicity range was extended to -0.5 dex as there is also a possibility of planet formation for metallicities lower than the solar one as reported by Adibekyan et al. (2012). The stars with planets were selected from the catalogue by Schneider et al. (2011).
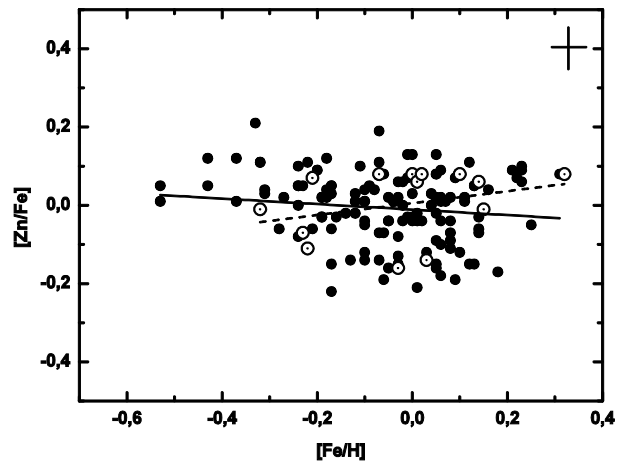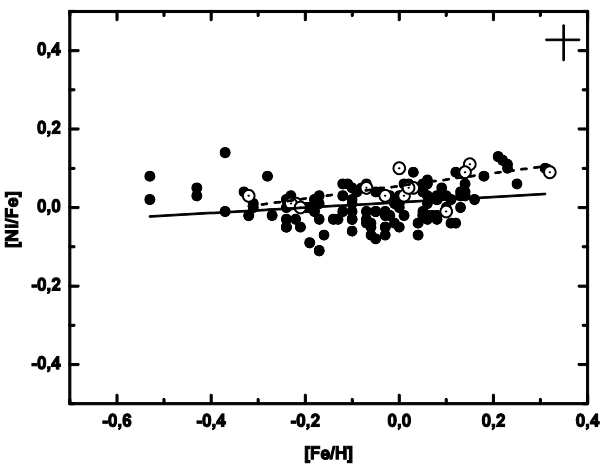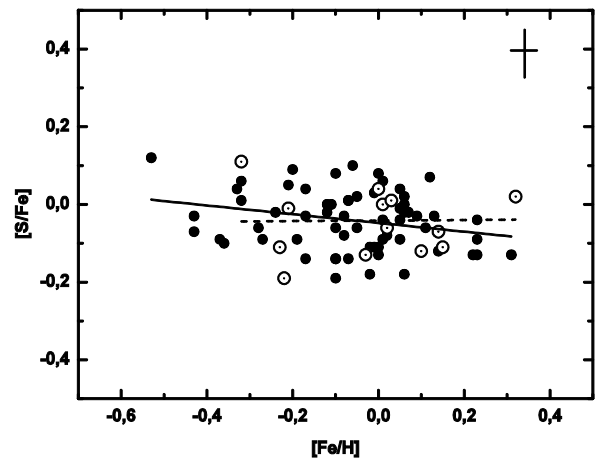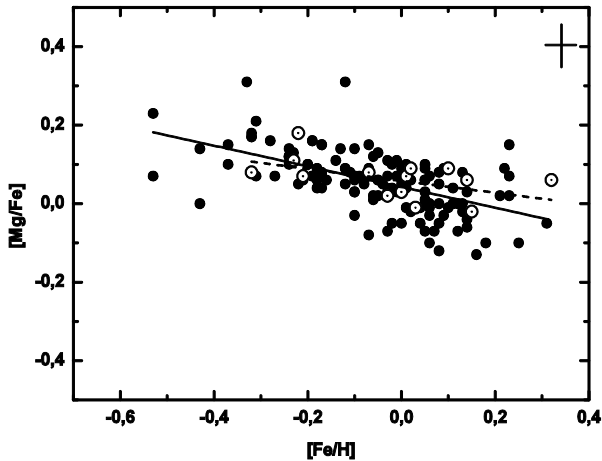
Figures 3, 4: The dependence of the magnesium and nickel (refractory elements) abundances on [Fe/H] in planet-hosting stars (marked with circled dots) and stars without planets around them (marked with solid circles).

Figures 5, 6: The dependence of the sulphur and zinc (volatile elements) abundances on the metallicity in planet-hosting stars (marked with circled dots) and stars without planets around them (marked with solid circles).

As is seen from the presented figures (Figs. 3-6), there are neither differences in the abundances nor trends exceeding the determination errors for either stars with or without planets.

6. Conclusions

Based on the high-resolution spectra and computed synthetic spectra accounting for the hyperfine structure, we determined the sulphur abundance for 175 dwarfs of the thin and thick discs. We found the following:
1) Sulphur behaves as a typical alpha-element showing no difference comparing to the behaviour of other α-elements. The comparison with the theories of nucleosynthesis and chemical evolution of the Galaxy counts in favour of the hypothesis that the primary source of the sulphur production is the oxygen and neon burning both at the pre-supernova stage and in the explosive burning processes in massive core-collapse supernovae.
2) As a volatile element sulphur does not exhibit any difference in behaviour for either stars with or without planets discovered around.

References

Adibekyan V.Zh., Delgado Mena, Sousa S.G. et al.: 2012, *Astron. Astrophys.*, **547**, 36A.
Baranne A., Queloz D., Mayor M. et al.: 1996, *Astron. and Astrophys. Suppl. Ser.*, **119**, 373.
Caffau E., Bonifacio P., Faraggiana R. et al.: 2005a, *Astron. Astrophys.*, **441**, 533.
Caffau E., Bonifacio P., Faraggiana R. et al.: 2005b, *Astron. Astrophys.*, **436**, L9.
Caffau E., Monaco L., Spite M. et al.: 2014, *Astron. Astrophys.*, **568**, 29.
Chen Y.Q., Nissen P.E., Zhao G. et al.: 2002, *Astron. Astrophys.*, **390**, 225.
Clegg R.E.S., Tomkin J., Lambert D.L.: 1981, *Astrophys. J.*, **250**, 262.
Ecuvillon A., Israelian G., Santos N.C. et al.: 2004, *Astron. Astrophys.*, **426**, 619.
Francois P.: 1988, *Astron. Astrophys.*, **195**, 226.
Galazutdinov G.A.: 1992, *Prepr.SAO RAS*, **92**, 28.

Gonzalez G.: 1997, *Mon.Not. Royal. Astron.Soc.*, **285**, 403.

Gonzalez G., Laws C., Tyagi S. et al.: 2001, *Astron. J.*, **121**, 432.

Goswami A., Prantzos N.: 2000, *Astron. Astrophys.*, **359,** 191.

Israelian G., Rebolo R.: 2001, *Astrophys. J.*, **557**, L43.

Katz D., Soubiran C., Cayrel R. et al.: 1998, *Astron. Astrophys.*, **338**, 151.

Kobayashi C., Nomoto K.: 2009, *Astrophys. J.*, **707**, 1466.

Kovtyukh V.V., Soubiran C., Belik S.I.: 2004, *Astron. Astrophys.*, **427**, 923.

Korotin S.A.: 2009, *Astron. Rep.*, **53**, 651.

Kupka F., Piskunov N.E., Ryabchikova T.A. et al.: 1999, *Astron. and Astrophys. Suppl. Ser.*, **138,** 119.

Kurucz R.L., Furenlid I., Brault J. et al.: 1984, Solar Flux Atlas.

Kurucz R.L.: 1993, CD ROM n13.

Limongi M., Chieffi A.: 2003, *Mem. Soc. Astron. It. Suppl.*, **3**, 58.

Matrozis E., Ryde N., Dupree A.K.: 2013, *Astron. Astrophys.*, **559**, A115.

Mishenina T.V., Pignatari M., Korotin S.A. et al.: 2013, *Astron. Astrophys.*, **552**, A128.

Nissen P.E., Chen Y.Q., Asplund M. et al.: 2004, *Astron. Astrophys.*, **415**, 993.

Ryde N. & Lambert D.L.: 2004, *Astron. Astrophys.*, **415**, 559.

Santos N.C., Israelian G., Mayor M.: 2000, *Astron. Astrophys.*, **363**, 228.

Santos N.C., Israelian G., Mayor M.: 2001, *Astron. Astrophys.*, **373**, 1019.

Sbordone L., Limongi M., Chieffi A. et al.: 2009, *Astron. Astrophys.*, **503**, 121.

Schneider J., Dedieu C., Le Sidaner P. et al.: 2011, *Astron. Astrophys.*, **532**, 79.

Soubiran C., Girard F.: 2005, *Astron. Astrophys.*, **438**, 139.

Takada-Hidai M., Takeda Y., Sato S. et al.: 2002, *Astrophys. J.*, **573**, 614.

Takeda Y., Hashimoto O., Tagushi H. et al.: 2005, *Publ. Astron. Soc. Japan*, **57**, 751.

Timmes F.X., Woosley S.E., Weaver T.A.: 1995, *Astrophys. J. Suppl. Ser.*, **98**, 617.

Thielemann F.-K. & Arnett W. D.: 1985, *Astrophys. J.*, **295**, 589.

Tsymbal V.V.: 1996, *ASP Conf. Ser.*, **108**, 198.

Wallerstein G. & Conti P.: 1964, *Astrophys. J.*, **140**, 858.

Woosley S.E. & Weaver T.A.: 1995, *Astrophys. J. Suppl. Ser.*, **101**, 181.

ATMOSPHERIC OZONE PROFILES DURING
VASYLKIV OIL BURNING   EPISODE

A.Shavrina[1], A.Veles[1], G.Milinevsky[1,2], A.Grytsai[2], A.Liptuga[3], V.Kyslyi[3], Ya.Romanyuk[1]

[1] Main Astronomical Observatory of National Academy of Scienses of Ukraine,
Kyiv, Ukraine
[2] Taras Shevchenko National University of Kyiv, Kyiv, Ukraine
[3] V.E.Lashkaryov Institute of Semiconductor Physics of National Academy of Scienses
of Ukraine, Kyiv, Ukraine

ABSTRACT. Ground-based Fourier Transform Infrared spectrometer (FTIR) observations have been used for study stratosphere/troposphere ozone vertical distribution during Vasylkiv (near Kyiv, Ukraine) incident of petroleum storage burning in June 8–14, 2015.

1. Introduction

The study of fire-oil incidents influence on atmospheric ozone is important because the ozone content in the Earth's atmosphere is of critical importance. The stratospheric ozone layer protects all living organisms on Earth from the harmful effects of excessive ultraviolet solar irradiation. Scientists consider organic compounds contained bromine, chlorine as substances that destroy the ozone layer. The ozone depleting potential (ODP) is the paremeter which allow estimate the harmful properties for ozone quantitatively. The higher the ODP of a certain substance, the more dangerous it is to the ozone layer. The highest ODP, reaching 12, have gallons, organic gases, which are used, for example, for fire extinguishing. On the contrary, high concentrations of ozone in the lower part of the atmosphere, the troposphere, ozone acts as health hazardous air pollutant.Tropospheric ozone is very toxic to air breathing organisms like humans and corrosive to the leaf surfaces of plants.

Total ozone column (TOC) is a parameter which characterizes total number of ozone molecules in the atmospheric column over observation site. This atmospheric parameter is traditionally measured in Dobson Units (DU): 1 DU corresponds to gas layer with thickness in 0.01 mm under standard atmospheric pressure and temperature. TOC is determined by many photochemical and dynamical processes both of stratospheric and tropospheric origin.

Ozone levels in the middle latitudes of the Northern Hemisphere are strongly dependent on the Brewer–Dobson circulation (Butchart, 2014), which causes air transport from tropic regions. Time of the seasonal ozone maximum is changed with longitude (Peters et al., 2008). Over Ukraine, the maximum is usually registered during early spring with total ozone values being equal 400–450 DU (Evtushevsky et al., 2014). During the next months, the TOC levels decrease with a minimum existing in October-November when total ozone could be only 280–290 DU or even lower. Short-term total ozone variations are also observed. In particular, a TOC decrease is frequently registered under anticyclone conditions with high pressure and, respectively, TOC rises during cyclone activity with low pressure.

Total ozone could be changed due to tropospheric influence of the anthropogenic origin. It is known about TOC variations during Persian Gulf War in 1991 (Herring and Hobbs, 1992). The changes were caused by oil fires in Kuwait (Herring et al., 1996). The effect is described as a complicated phenomenon. In these events additional tropospheric was created close to the fire regions. On the contrary, at the edge of the fire area the total ozone values were lower than usually.

In June 8, 2015, significant oil burning began near Vasylkiv city (48.98°N, 31.32°E**)** close to Kyiv (Ukraine**)**. It is continued during a week with penetrating large number of smoke particles into the atmosphere. Correspondingly, a question on a possible influence of the fire onto ozone levels over the surrounding area is matter of interest. The methods of analysis and the picture of the phenomenon are briefly described in the next parts of the paper.

2. Spectral modeling and analysis

The estimates of total ozone columns in the Earth's atmosphere were obtained using a simulation of the ozone absorption spectrum at 9.6 μ with the radiative transfer code MODTRAN4.3 (Bernstein et al., 1996). The program calculates the transmission of electromagnetic radiation of solar origin through the modelled atmosphere and its subsequent reflection on the surface in the frequency range from 1 to 50000 cm^{-1}. The program employs a two-parameter (temperature and pressure) model of molecular spectral absorption, which is calculated with the molecular database HITRAN (http://www.cfa.harvard.edu/hitran/) containing molecular spectral absorption lines. To calcu-

late the band model, data for 12 light gaseous molecules (H_2O, CO_2, O_3, CO, CH_4, O_2, NO, SO_2, NO_2, N_2O, NH_4 and HNO_3) from the HITRAN database were used, and for heavy molecules – CFC (9 molecules) and $CLONO_2$, HNO_4, $CCl4$ and N_2O_5 the calculated absorption cross section (see [Bernstein et al., 1996]) were applied. The calculations were performed in the approximation of local thermodynamic equilibrium (LTE) for the moderate spectral resolution of 2 cm^{-1} which corresponds almost exactly to our observed spectra. The model parameters have been calculated by us using the database HITRAN–2004 (Rothman et al., 2005). To construct the *apriori* atmospheric profiles of ozone, temperature and water vapor were employed here (i) the observation of surface ozone concentrations as measured by the ground based ultraviolet ozonometer TEI-49i that is located near to the Fourier spectrometer detecting breathing-level ozone, (ii) data of the NASA Atmospheric Infrared Sounder (AIRS) satellite instrument (http://avdc.gsfc.nasa.gov/Data/AIRS/) onboard of the NASA EOS-Aqua satellite. A detailed description of our method for determining tropospheric and stratospheric concentrations of ozone can be found in (Shavrina et al., 2007, Shavrina et al., 2008). The result of the analysis is the best fit of the model spectrum to the observed spectra of the ozone band, from which we obtained the best estimates of the tropospheric vertical profiles of ozone, the total column amount of ozone in the troposphere and finally the total column amount of ozone in the atmosphere.

Figure 1: Smoke from oil burning near Vasylkiv on the evening of June 8, 2015.

3. Results

Total ozone is measured in Kyiv-Goloseyev station located at Main Astronomical Observatory (50.36° N, 30.50° E, altitude 206 m) in the southern part of Kyiv. Total ozone measurements are carried out with Dobson spectrophotometer every day. To retrieve ozone vertical profiles, ground-based Fourier Transform Infrared spectrometer (FTIR) observations are realized under good weather conditions. The FTIR observations have been used to study the stratosphere and troposphere ozone vertical distribution during Vasylkiv incident with petroleum

storage burning in June 8–14, 2015 (Fig. 1). The MODTRAN4 modeling of O_3 (9.6 μ) absorption band profile and FTIR measurements allow to analyze the ozone profiles. A noticeable decrease of total ozone (to values below 300 DU) was registered 13 June at Kyiv-Goloseyev GAW station 498 (Milinevsky et al. 2012) after the wind was directed from Vasylkiv to Kyiv (Fig. 2). A distance between the burning point and the observational station is equal to 25 km.

Aura-OMI data for June 2015 have also exhibited ozone decrease in June 12–13 with a minimum near 310 DU (Fig. 3). Earlier, in June 5–10, total ozone values reached 340–350 DU. In the following days, high ozone conditions recovered and were observed till June 25. Wind directions on different heights are evident from back trajectories NOAA ARL HYSPLIT data (Draxler and Rolph 2015). For example, maps for June 13 when air mass with products of oil-burning arrived to Kyiv site from south-west are presented in Fig. 4.

In that day, almost the same low total ozone values were registered by Aqua-AIRS on a vast area (~200x800km) to south-east from Kyiv (50.36° N, 30.50° E). The corresponding pattern is shown in Fig. 5. One of the possible causes for the observed ozone destruction could be in elevation of the oil burning products and organic gases which were used for fire extinguishing.

4. Conclusions

Total ozone content and ozone vertical profiles over Kyiv and neighboring area were studied for June 2015. Ozone decrease in June, 13 is indicated with the ground-based (Dobson, FTIR) and satellite (AIRS, OMI) data series. Analysis of back trajectories has demonstrated a change in the predominant wind direction in the troposphere in June 13. The ozone decrease could be partly connected with strong oil burning which lasted near Vasylkiv in June 8-14.

References

Bernstein L.S., Berk A., Acharya P.K., Robertson D.C., Anderson G.P., Chetwynd J.H., Kimball L.M.: 1996, *J. Atmosph. Sci.,* **53**, 2887.

Butchart N.: 2014*, Reviews of Geophysics*, **52**, 157 .

Draxler R.R. & Rolph G.D.: 2015. HYSPLIT (HYbrid Single-Particle Lagrangian Integrated Trajectory) Model access via NOAA ARL READY (http://ready.arl.noaa.gov/HYSPLIT.php). NOAA Air Resources Laboratory, Silver Spring, MD.

Evtushevsky O., Grytsai A., Milinevsky G.: 2014*, Remote Sensing Letters*, **5**, 205.

Herring J.A., Ferek R.J., Hobbs P.V.: 1996, *J. Geophys. Research*, **101**, 14451.
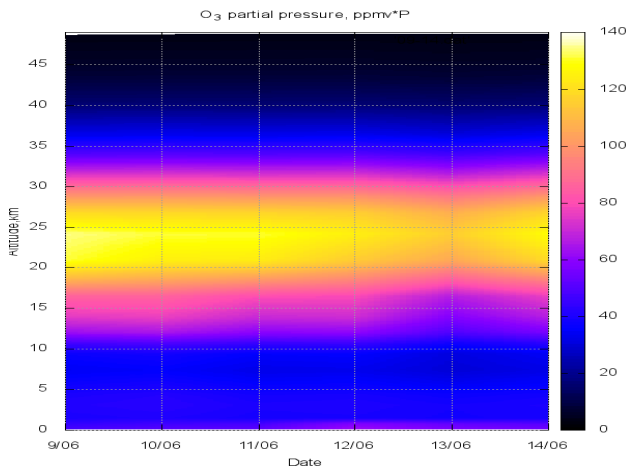
Figure 2: Ozone vertical distribution from FTIR observations, June 9–14, 2015.
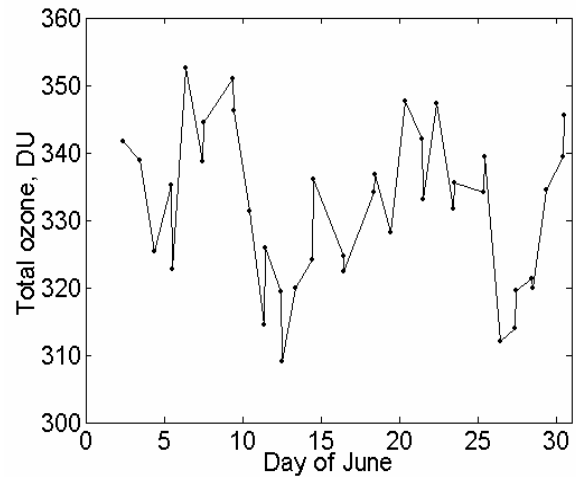
Figure 3: Total ozone over Kyiv-Goloseyev station in June 2015 from Aura-OMI observations.
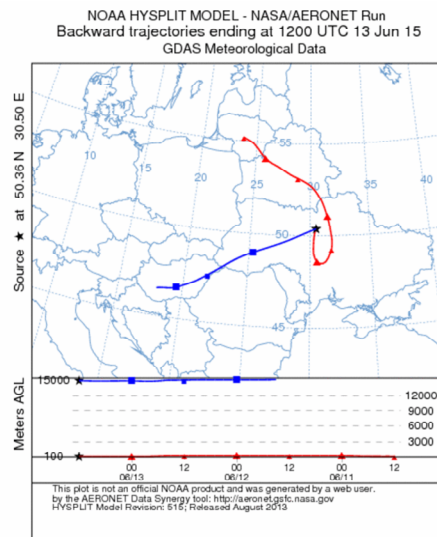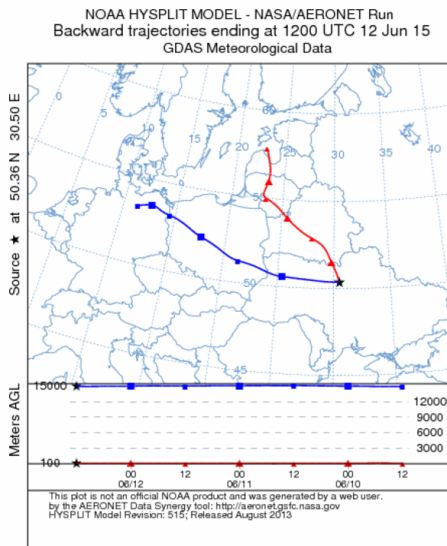
Figure 4: Back trajectories at 12 UTC of both 12 June (left panel) and 13 June (right panel) at the heights of 500 m (red curve) and 15 km (blue curve).
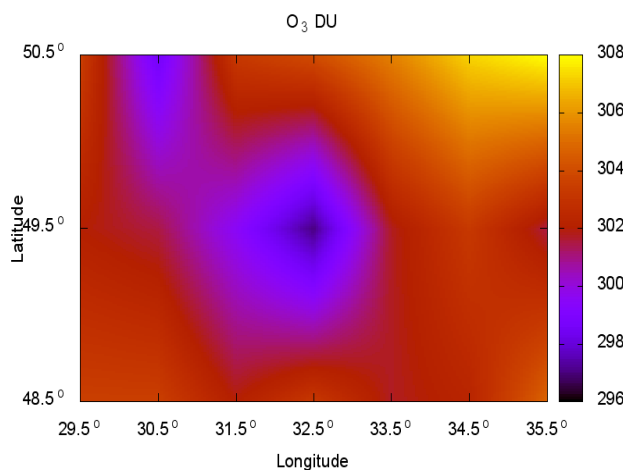
Figure 5: AIRS ozone distribution in June 13, 2015. Total ozone values correspond to the color bar presented in the right part of the figure.

Herring J.A. & Hobbs P.V.: 1992, *J. Geophys. Res.*, **97**, 14507.

Milinevsky G.P., Danylevsky V.O., Grytsai A.V., Evtushevsky O.M., Kravchenko V.O., Bovchaliuk A.P., Bovchaliuk V.P., Sosonkin M.G., Goloub Ph., Savitska L.Y., Udodov E.V., Voytenko V.P.: 2012, *Advanced in Astronomy and Space Physics*, **2**, 114.

Rothman L. S., Jasqumart D., et al.: 2005, *J. of Quantitative Spectroscopy & Radiative Transfer*. **96**, 139.

Peters, D.H.W., Gabriel A., Entzian G.: 2008, *Annales Geophysicae*, 2008, **26**, 1275.

Shavrina A.V., Pavlenko Ya.V., Veles A. et al.: 2007, *J. of Geophys. Res.*, **112,** D24S45, doi:10.1029/2007JD008787.

Shavrina A.V., Pavlenko Ya.V., Veles A., Sheminova V.A., Syniavskyi I., Sosonkin M.G., Romanyuk Ya.O., Eremenko N.A., Ivanov Yu.C., Monsar O.A., Kroon M.: 2008, *Kosmichna nauka i tekhnologiya*, 2008, **14**, N 5, 85-94 (in Russian).

ABOUT THE NATURE OF METEOR FLARES

V.A.Smirnov

National Academy of Communications, Odessa, Ukraine
smirnovw@tm.odessa.ua

ABSTRACT. Whereas at development of the meteoric phenomenon there are processes in different temporary scales (more slow processes heat conductivity, mechanical rotation, destruction) and considerably faster (fluctuations of brightness of radiating plasma is like gas-dynamical laser), the observable flares of meteors differ in nature, and in appearance caused by character of radiation.

Continuing development of the meteoric phenomena in the Earth's atmosphere has been described by Astapovich I.S. (Astapovich I.S. 1958). The classification of meteor flashes which depends on the physical nature of the phenomenon is given below and the formulas of a physical theory representing these processes while moving the meteor are presented here.

Key words: Flares, Meteor stream, Gas-dynamical laser, Ambipolar diffusion, Kinetics of meteor plasma.

1. Introduction

Analyzing the flares of fast meteors of Perseid, Orionid, Leonid meteoric streams and similar to those flares with identical radiation character are allocated in meteors of the same streams. Some flares, like for example double flares at the end of meteor path, are difficult to explain with regular methods of meteoroid's mechanical destruction, as mechanical changes proceed incomparably more slowly than the processes of changing of observable meteoric plasma radiation (Smirnov, 1994, 2007).

The flares of slow bolides, rather slow massive meteors flying with speed less than 60 km/s form radiation simultaneously in all so-called "spectral lines" of the meteor spectral image – "lines" are monochromatic images of a meteor and cannot be used for constructing growth curves or self-absorption calculation. - V.S. – . These meteor flares can be recurring with the frequency of a meteor body rotation while dumping the fused layers of a meteor body and other similar mechanical phenomena.

Fast alternation of flares in this case characterizes discarding of a meteor separate boiling luminous layers in process of penetration of a meteoric body deep into atmosphere with the appropriate boiling point of a substance (for iron 2735^0C). The "mechanical" flare spectral lines light up at once simultaneously for the whole spectrum.

During the penetration of a meteoroid into the more dense atmospheric layers, formed meteor plasma interacts both with the meteor body and environment – continuously increasing in density atmospheric gas.

In the above shower meteors the shock waves formed during the meteor body flight, along with the ambipolar diffusion, considerably accelerate and strengthen thermal ionization and thereby formation of the meteor plasma, plasma "clot".

At over 60 km/s speed of the shower meteors, meteor plasma moves along with meteoroid with over 60 km/s speed and causes immediate radiation intensity transformations (Smirnov, 2000, 2003).

Penetration of the meteor into the denser atmospheric layers entails emerging plasma that may often appear as a plasma formation with radiation similar to that of a gas-dynamical laser. The flares with almost complete loss of the meteor mass by evaporation appear during the inevitable dissipation of the meteor plasma into void. The process is identical to a gas-dynamical laser radiation.

The first to light up in the "lines", according to the Wien law, is the higher wavelength spectrum part followed by the whole set of spectral "lines". These "laser" flares were called type A.

In this shown way experiments with the observed gas-dynamical laser luminescence can be done. The experiments should simulate expansion of plasma into void as a function of the time-related medium density enhancement that corresponds to air density from zero to a 60-70 km height atmosphere density. In this case attention should be paid to presence or absence of the flares similar to meteor ones.

In work (Shinsuke Abe at al., 2007) on Fig 1 is shown spectrum of Leonid fireball, in which imposing both types of flares most likely is shown (see Fig.1).

2. Ambipolar diffusion

For understanding the plasmoid formation mechanism while the fast meteor`s movement belongs as a rule to the meteor shower, we should recall the formulas defining the phenomenon of the ambipolar diffusion.

Flying meteors are known to be surrounded with ionized air columns. Thus ambipolar diffusion occurs continuously with the resulting plasma-like meteor clot. Ambipolar diffusion is the primary process in relation to excitation and radiation of the meteor ionized trace.

During diffusion the stream of particles j is proportional to a gradient of concentration:

$$j = -D\nabla N, \tag{1}$$

where D is diffusion coefficient proportional to a V particle characteristic velocity and the length of free path λ. According to the Einstein ratio the diffusivity is proportional to mobility of b particles and gas temperature T:

$$D=bT/e, \tag{2}$$

where e is the elementary charge.

During diffusion of charged particles, the streams of electrons and ions are composed both of diffusional and directional ones in electrical field:

$$j_e = -D_e\nabla N_e - b_e N_e E,$$
$$j_j = -D_j\nabla N_i + b_i N_i E, \tag{3}$$

where E is the intensity of the field resulting from separation of charges; b_e, b_i are the mobilities of electrons and ions; D_e, D_i are diffusivities of plasma electrons and ions; N_e, N_i are concentrations of electrons and positive ions.

Let's mark mass of an electron m_e and mass of positive heavy ion, m_i. From the ratio

$$\frac{D_e}{D_i} \approx \frac{V_e}{V_i} \cong \sqrt{\frac{m_i}{m_e}} \tag{4}$$

it is seen that the drift velocity of an electron is 2-3 orders higher than the velocity of positive ions. If an ionized "electronic" trace formation time is 10^{-3} s, then the time of filling this cylindrical trace with positive ions will be no less than 0.4 s. The same mechanism is involved in plasma clot formation as well.

3. Scattering kinetics of meteoric plasma

Thus, considering the meteoric phenomenon development in real-time mode we can guess that by the end of the meteoroid particles evaporation and sublimation process the originated as a meteoric coma plasma clot loses its source of radiating particles replenishment.

As reference data suggest, at 90 km height an average length of air particles free run is 2.4 cm, at 80 km height – 0.4 cm. So geometric meteor measures correspond to the ones of radiating meteoroid, and only these physical conditions give start to the process of heating and subsequent intensive luminescence of the meteoroid (Astapovich, 1958).

Heat conductivity according to the researched soil data at densit ρ=0.5 g/cm³ and 90% porosity is $0.48 \cdot 10^{-4}$ Joule/mm.s.K (Chudnovsky, 1976). The slow process of heat conductivity is responsible for meteoric body inertness preservation during flight and accounts for physical distinction between flares, such as types A and B.

During the meteor body radiating particles source disappearance the overall brightness of the meteor declines to full disappearance of solid mass. As was shown (Smirnov, 1994, 2007), a visible spectrum radiation is possible when radiating plasma velocity is decelerated

down to 2-3 km/s is. If the velocity of meteor plasma would actually stay equal to the Leonids, Orionids, or Perseids streams meteor velocity, the maximum in the spectrum energy distribution would be displaced into X-ray part of the spectrum, which fact was never observed.

The extension of the terminal plasma clot into void can be described according to the law:

$$\rho = \frac{m}{\frac{4}{3}\pi R^3} = \rho_0\left(\frac{t_0}{t}\right)^3, \tag{5}$$

Hence, the expression for a time scale is determined as

$$t_0 = \left(\frac{m}{\rho_0 \frac{4}{3}\pi V^3}\right)^{1/3} \tag{6}$$

In (5) and (6) ρ_0 is the initial density of a plasma clot and m is mass of a meteoroid; the radius of a full sphere formed by plasma with density ρ is determined according to formula: R=Vt. So: during the about 0,3 s average time the scattering of plasma occurs, it filling the sphere with R radius; attenuation of the meteoroid's brightness preceding a final bright flare occurs.

The kinetics equation for extending plasma (Smirnov, 1994, 2000, 2002; Biberman et al., 1982) related to ionization level

$$x = \frac{N_e}{N},$$

where N_e is concentration of electrons, and N is concentration of colliding particles, looks like:

$$\frac{dx}{dt} = -\alpha N^2 x^3, \tag{7}$$

where α is a recombination coefficient, $\alpha = A T_e^{-9/2}$.

In the above expression A is constant, T_e - electronic temperature.

If degree of ionization is $x=x_0$ at t_0, then the equation solution can be represented as:

$$x = x_0\left[1 + 2Ax_0^2\int_{t_0}^{t}\frac{N^2(t)dt}{T_e^{3/2}(t)}\right]^{-1/2} \tag{8}$$

Thus, as is seen from (8), the number of particles N under radiation source impact will increase within one second, with constant volume preserved. Actually while scattering, however, the volume increases proportionally to R³, and electronic temperature, as well as concentration of particles accordingly decrease. Numerical examples are cited in (Smirnov, 1994).
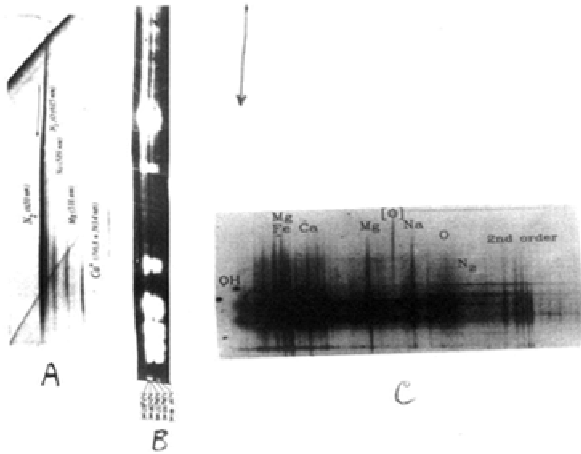
Figure 1:
A – type flare spectrum of Leonids, November 17/18, 1965, photographed by the author. Final flare shows the «laser» radiation behavior.
B – the fireball spectrum with flares caused by rotation of a meteoric body moving in atmosphere, «mechanical» radiation behavior.
C – a Leonids spectrum from Japan (Abe et al., 2007). Radiation behavior suggests superimposed flares of A and B types.
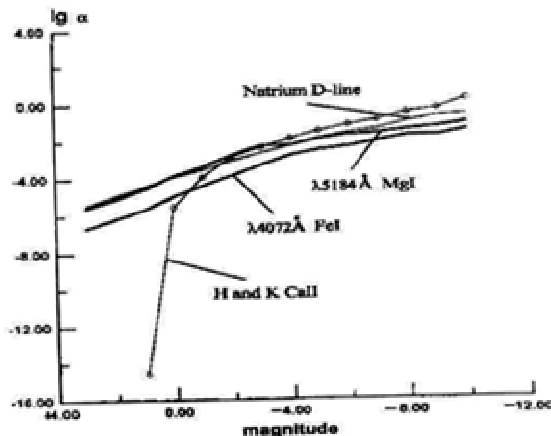
Figure 2: Coefficient of radiation intensification (on logarithmic scale) related to the meteor's stellar magnitude.

4. Conclusion: the mechanism of the Perseid', Orionid', Leonid' streams meteor characteristic flare

At an early stage of the meteor plasma clot scattering all relaxation processes are fast, and gas can be suggested to preserve a thermodynamic equilibrium.

Without the meteoroid's radiating mass replenishment which fact can be basically verified experimentally, in meteor plasma expanding through ambipolar diffusion the degree of particles excitation will increase through a shock wave due to recombination stream from above.

Populated in plasma particles are the levels nearing the edge of the continuous spectrum. A specific inversion is formed, followed by the maximum induced radiation.

With meteoric plasma disintegration, the excitation degrees of other atomic power levels should also increase until downward stream from every level due to spontaneous transitions and deactivation becomes predominating over a stream from continuous spectrum which will eventually decrease with particles concentration decrease.

The significant enough factors of radiation intensification due to such "macroquantum" effect are found only for fast stream meteors. As the meteor plasma is a mixture of various elements, hence excitation of the basic element brings forth intensification of others, as the experiments show (Smirnov, 1994).

If we admit that radiation from a final flare is produced by particles resulting from the inversed population of the particle levels, we can calculate coefficient of possible luminescence intensification with the help of a method often used for definition of the laser effect.

Let at first approximation the Doppler widening of spectral lines predominate over other widening mechanisms at low pressure. Width of a spectral line can be obtained according to the formula:

$$\Delta \nu = \frac{2}{\lambda}\sqrt{\frac{2\ln kT}{m}},\qquad (9)$$

where λ is the length of a wave in meters, m is the atom mass in kilograms, T is the Kelvin absolute temperature, k is the Boltzmann constant. Coefficient of radiation intensification $a(\nu)$ due to inversion can be computed by the formula:

$$a(\nu) = \frac{1}{4}\lambda^2 g_k a_{ki}\left[\frac{N_k}{g_k} - \frac{N_i}{g_i}\right],\qquad (10)$$

Where g_k and g_i are statistical weights of levels with populations N_k and N_i, respectively. If the frequency corresponding to a given spectral line is ν_0, spectral density a_{ki}, the first factor of the Einstein coefficient A_{ki}, then a_{ki} is equal :

$$a_{ki} = A_{ki}(\sqrt{\pi}\Delta\nu)^{-1}\exp\left[-\frac{(\nu-\nu_0)^2}{\Delta\nu^2}\right].\qquad (11)$$

The computed data for radiation intensification coefficient in m^{-1} units for the Fe1 spectral line center $\lambda = 4072\,\text{Å}$, MgI $\lambda = 5184\,\text{Å}$, sodium D-lines, and CaII lines H and K are shown in Fig. 2 as a function of stellar magnitude.

Thus, for a A-meteor from Fig.1 from a stream of Leonids photographed by the author on November 17, 1965 radiation intensification due to the above effect was about 150 per each kilometer. The numerical examples are shown in (Smirnov, 2000).

Hence, the meteor phenomena are accompanied by the following processes in different time scales:

1. Relatively slow processes of heat conductivity, mechanical rotation, splitting, and

2. Considerably faster brightness fluctuations in the emerged clot of meteor radiating plasma, similar to gas-dynamical laser radiation.

The flares caused by the first and second reasons differ both in nature and appearance depending on the character of radiation.

As was specified above, let's name "mechanical" flares type B and "laser" ones type A.

In Fig.2 on the next page (Smirnov, 2007) the flares of B type are shown for rather slow fireballs when the plasma component of the meteor phenomenon does not show itself, as velocity is insufficient for its formation. The flares are formed due to mechanics of a meteor body rotation accompanied by fusion of its outside layers and discarding the fused substance into atmosphere. In Fig.1 (Smirnov, 2007) the A type flare for Leonids radiation with prevalence of a meteor plasma luminescence according to the Wien law with final flare is shown.

In (Abe et al., 2007) Fig. 1 features the bright Leonid's spectrum in which both types of flares are most likely inter-imposed. The topmost bright flare can be supposed to result from the A and B flares superimposition; a flare at the meteor path end and with the meteor complete disintegration corresponds to type A. In this way the figure shows the "laser" radiation factor at the meteor spectrogram.

Fig. 1 of this work shows all three meteor spectrograms discussed above. Comparison of spectrograms shows their correspondence to the above-said. Fig. 2 presents radiation intensification coefficients (on logarithmical scale) related to the meteor stellar magnitude (Smirnov, 2000).

References

Abe S., Ebizuka N., Yano H., Watanabe J., Borovicka J.: 2007, *Adv. Space Res.*, **39**, 4, 538-543.

Astapovich I.S. Meteor Phenomena in the Land Atmosphere. Fizmatgiz, Moscow, 1958.

Biberman L.M., Vorobjov V.S., Jakubov I.T. The Kinetics of Non-equilibrium Low-temperature plasma. Science. Moscow, 1982.

Chudnovsky A.F. Heat-physics of Soils. Science, Moscow, 1976.

Smirnov V.A.: 2007, *Adv. Space Res.*, **39**, 4, 526-532.

Smirnov V.A. The Spectra of Transient Atmospheric Luminous Phenomena: Meteors. Physico-Mathematical Literature, Moscow, 1994.

Smirnov V.A.: 2000, *Proc. of IMC Frasso Sabino, International Meteor Organization*, 59-71.

Smirnov V.A.: 2003, in: *Proc. of IMC Frombork* /eds. Olech A., Zloczewski K., Mularczyk K., Poland 26 - 29 September 2002. International Meteor Organization, 119 – 124.

THE PHYSICAL MEANING OF THE TITIUS-BODE FORMULA

V.A.Smirnov

National Academy of Communications, Odessa, Ukraine
smirnovw@tm.odessa.ua

ABSTRACT. It is proposed an special hypothesis of the formation of symmetric objects in space with the help of the interference of standing waves which act in the process of evolution of the primordial gas-dust cloud including the formation of the Solar system, that may be revealed by 11-year cycle of Solar activity in particular.

It is used the idea of J.Kepler of the construction of the Solar system, viewed as inscribed and circumscribed Platonic figures, a common measure of which, according to the author, is the length of the standing waves generated by the variable energy sources of the primary cloud. This explains the physical meaning of the Titius-Bode formula.

In 1968 S.F.Dermott revealed the foundation of Titius-Bode empiric formula, basing on Theory of Resonance. But in addition to direct statement of existing resonance mechanism of formula $T(n)=T(0) \cdot C^n$, n=1,2,3,4, physical sense does not come to light. I tried to explain the formation of symmetric figures and space constructions with evident experience of formation of Chladni E. figures, offering the calculation, confirmed by experience of appearance of new space bodies in the nodes of standing waves of primary gas-dust cloud. The interference of standings waves is surely promotes the formation of different figures – such as symmetric galaxies, hexagon vortex at Saturn, and others. Unlike Dermott's theory, our explanation of symmetric formation of planets is a common solution of task for multi bodies interaction, and proposes the version of solution in case with more than two bodies.

Key words: Standing Waves, Chladni Experiments, Nodes

The process of evolution of the solar system means the development of the structure of gas-dust cloud after the initial impulse by way of the impact in most cases of a supernova explosion. Thus the wave motions are practically excluded from consideration. As the experience shows at the time of the formation of standing waves with the observed acoustic resonance the wave motions at the nodal points can accumulate clumps of matter that make up the primary cloud. A similar pattern is observed in the experiments of Chladni E. (Smirnov, 1999).

J.Kepler's plan of the solar system, which took into account the distribution of the planets according to their distance to the Sun, was built as a series of inscribed and circumscribed Platonic figures (Kepler, 1939). According to his scheme the average distances of the planets to the Sun could be obtained in the form of the radiuses of the circumscribed spheres (Fig. 1). This fact indicates the existence of a common measure of the Platonic figures constructed in such a way.
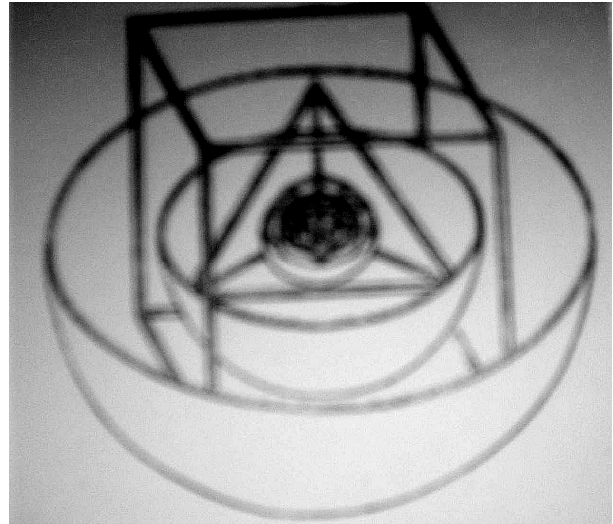
Figure 1: In the work of Johannes Kepler "Welt-Harmonik" the great scientist builds a plan of a distribution of planets in the solar system in the form of inscribed and described Platonic figures (see page 287). Using since the time of Huygens the well – known concept of wavelength and frequency fluctuations in the standing wave one can build a plan of the solar system taking into account these concepts which duplicate dimensions in the formula Titius – Bode.

In the time of Kepler the concepts of the wavelength were not yet used. That's why Kepler could come to the conclusion that the length of a standing wave λ, emitted by the central formation of the Solar system that forms waves of energy into space, which are shaping with the reflected waves from the interface of more dense environmental conditions of the gaseous nebula and less dense environmental conditions of the surrounding space, could serve as a common measure for measuring distances of the planets to the Sun. If the standing wave in the one-dimensional case of the reflection from a less dense medium is formed in the Y axis direction with the displacement X, the wave equation can be written as:

$$X = a \cos \frac{2\pi}{\lambda} Y \cos \frac{2\pi}{T} t$$

The planets are being formed in the nodes generated in the wave where the oscillation amplitude is zero. In astronomical units the distances to the Sun are determined at the points along the axis $Y = \frac{2n+1}{4} . \lambda$, wherein n = 0 , 1, 2 ...

The comparison of the observed and calculated distances to the planets to the Sun and the distances of the satellites to the planets according to the proposed wave principle one can find in the author's work (Smirnov, 2001) .

Using this technique, we present the tables of calculated and measured distances of the planets to the Sun, Jupiter's satellites to the central planets and satellites of Saturn and Uranus to the central planets. Taking a common measure of the Platonic figures or the length of the standing wave λ, which forms the Solar system, $\lambda = 0,52$ AU , and taking an active place of the primary Sun which forms standing waves as the first term in the calculation formulas that determine the distances of the planets to the Sun through the position of the nodes of standing waves in the primary gas-dust cloud, we obtain table 1.

Table 1: Distances of the planets to the Sun expressed across the nodes of standing wave λ

Planet	True distance the planets to the Sun (AU)	Calculated the distance of planet to the Sun (AU)
Mercury	0,39	
Venus	0,72	$0,39 + 0,50\lambda = 0,65$
Earth	1,00	$0,39 + 1,50\lambda = 1,17$
Mars	1,52	$1,00 + 1,00\lambda = 1,52$
Main asteroid belt	2,90	$1,00 + 4,00\lambda = 3,08$
Jupiter	5,20	$1,00 + 8,00\lambda = 5,16$
Saturn	9,54	$1,00 + 16,0\lambda = 9,32$
Uranus	19,20	$1,00 + 35,0\lambda = 19,20$
Neptune	30,10	$1,00 + 56,0\lambda = 30,12$
Pluto	39,50	$1,00 + 74,0\lambda = 39,48$

Taking into account the length of the standing wave to be $\lambda = 240.10^3$ km for the system of satellites of Jupiter, we can derive the result similarly, as shown below:

Table 2.

Satellites of Jupiter	True distance to Jupiter (10^3km)	Calculated distance to Jupiter (10^3km)
5	181	
Io	422	$181 + \lambda = 422$
Europa	671	$181 + 2\lambda = 661$
Ganymede	1070	$181 + 4\lambda = 1141$
Callisto	1883	$181 + 7\lambda = 1861$
6	11476	$181 + 47\lambda = 11461$
10	11700	$181 + 48\lambda = 11701$
7	11737	$181 + 48\lambda = 11701$
12	21200	$181 + 88\lambda = 21301$
11	22600	$181 + 93\lambda = 22501$
8	23500	$181 + 97\lambda = 23461$
9	23600	$181 + 98\lambda = 23701$

From the Table of Jupiter satellites we notice that the 6th, 10th and 7th satellite, apparently, formed in the same node of the standing wave creating them. The same thing can be noticed concerning the 8th and 9th satellite. Between Calisto and the 6th satellite, probably, unnoticed masses of substances exist.

If we take as the "common measure" the length of characteristic standing wave for Saturn, $\lambda = 27.10^3$ km, then the distances of the Saturnian system of satellites displays the same wave regularity (Table 3).

If we take $\lambda = 62.10^3$ km as the effective wave length for the system of Uranian satellites were formed (Table 4).

Table 3.

Saturnian Satellite	True distance to Saturn (10^3km)	Calculated distance to Saturn (10^3 km)
Janus	159	
Mimas	186	$159 + \lambda = 186$
Enceladus	238	$159 + 3\lambda = 240$
Tethys	295	$159 + 5\lambda = 294$
Dione	377	$159 + 8\lambda = 375$
Rhea	527	$159 + 14\lambda = 537$
Titan	1222	$159 + 39\lambda = 1212$
Hyperion	1483	$159 + 49\lambda = 1482$
Iapetus	3560	$159 + 126\lambda = 3561$
Phoebe	12950	$159 + 474\lambda = 12957$

The error in most cases one sees almost complete coincidence of the calculated and experimental distances of planets to the Sun. As can be seen, in the basis of existence lies the universal wave principle and the space-time frames of the "golden section".

Table 4.

Uranian Satellite	True distance to Uranus (10^3km)	Calculated distance to Uranus (10^3km)
Miranda	130	
Ariel	192	$130 + \lambda = 192$
Umbriel	267	$130 + 2\lambda = 254$
Titania	438	$130 + 5\lambda = 440$
Oberon	586	$130 + 7\lambda = 564$

Figure 2: The whirlwind of the regular hexagonal structure in the northern hemisphere of Saturn, photographed by Cassini mission November 28, 2013 at a distance of 610.4 km. Formation diameter is 25,000 km.
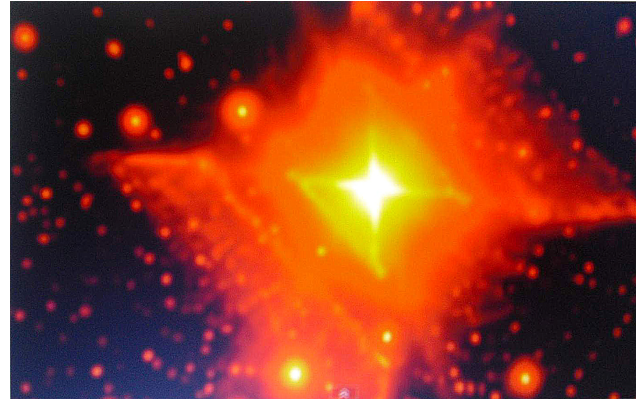
Figure 3: The Nebula MWC 922, formed in the shape of symmetrically arranged figures during the interference of standing waves.

The above formula for the distances of the planets to the Sun and the distances of the planets to their satellites, reveals the physical meaning of the well-known formula, composed empirically by Bode – Titius:

$$Y = 0,4 + 0,3.2^{n}, \text{ wherein } n = -\infty, 1,2,4, 5 \ldots$$

Note that in some cases the standing waves are responsible for the formation of symmetrical shapes of galaxies by cosmic objects that resemble the inscribed and circumscribed Platonic figures and the vortex formation in the form of hexagon on Saturn recently shown on the Internet.

According to the observations, the elementary calculation shows that the hexagon vortex is formed by a standing wave with a wavelength λ = 12500km (Fig. 2).

According to the reports of the Hubble telescope's observations in outer space, the energy waves are observed in the substance of the outer space while the evolution of galaxies and other objects, and the length of these energy waves reaches λ hundreds of light years.

Generally it is obvious that the discovery made with the help of the Hubble telescope of symmetrically constructed shapes of galaxies which echo the view of the Kepler-

figures showing the plan of the solar system can be explained only through the formation of the giant-scale energetic standing waves. For only in such cases of the formation of standing waves the distances between nodes and antinodes positions remain unchanged in time. This fact can explain the shape of the nebula MWC 922 (Fig. 3) Similarly, the appearance in the walls of the fixed giant vortex on Saturn as a hexagon explains the formation of its standing wave in the wall. Another explanation of these phenomena can hardly be found.

References

Dermott S.F.: 1968, *Mon. Not. RAS*, **141**, 363.
Dermott S.F.: 1969, *Mon. Not. RAS*, **142**, 143.
Kepler J., Welt-Harmonik, Verlag R.Oldenbourg, Munchen-Berlin, 1939, 403 p.
Smirnov V.A.: 1999, *Astronomical and Astrophysical Transaction*, **18**, 521.
Smirnov V.A.: 2001, in: *Proc of the International Meteor Conf.*, Cerkno, Slovenia, 20-23 September 2001, 64.

IDENTIFICATION OF GEOSTATIONARY SATELLITES BY THEIR PHOTOMETRIC AND DYNAMIC FEATURES, SOME PROBLEMS

P.P.Sukhov, K.P.Sukhov

Astronomical Observatory, Odessa National University
Shevchenko Park, 65014, Odessa, Ukraine
psukhov@ukr.net

ABSTRACT. It is possible to identify certain characteristics of geostationary satellites by studying their photometry. This paper reviews some of the technical problems and methodologies concerning photometry of satellites, as well as their identification by photometric characteristics. The existing methods of identifying geostationary satellites using photometry are also summarized. The present Database of photometric and dynamic characteristics of the GSS, additional information, simplifying the input of the inverse problem − all this allows modern methods to identify unknown GSS with a probability up to 80%.

Key words: geostationary satellite, GSS, photometrical features, identification, phase angle, effective reflective area, inverse problem.

1. Introduction

For geostationary satellites (GSS) identification, often enough orbital characteristics. This six Keplerian elements and the orbital plane position relative to the equatorial plane or Laplacian plane. However, as referred to in [1], in some cases, the identification of a compact groups GSS by its orbital parameters within an orbital slot or by coincidence of the orbital planes of explosion fragments results in erroneous identification. The non-coordinate information, such as photometrical, polarisation and spectral data, can play a crucial part in identification of the type of satellite and its purpose of use in the following cases: 1. The GSS redeployment, manoeuvres (which are quite frequent) or changeover of the temporarily deactivated satellite back to the active status. 2. Highly elliptical orbits are poorly monitored by ground-based radar and optical aids of space control services. 3. As a result of evolution, due to perturbations by the Moon, Sun, Earth, or light pressure, the GSS orbital plane oscillates relative to the Laplacian plane with a period of 54 years and an amplitude of about 15^0 [1]. Old passive GSS will enter the equatorial plane by 2017. And it will be difficult to distinguish a new GSS from an old one, which was launched 54 years ago, by orbital parameters.

The following methods for space object (SO) identification are known: 1. Identification by orbital parameters.

2. Identification by the image obtained with long focal-length optical telescopes. 3. Identification by the space object (SO) image during its passage across the Moon's or Sun's disc. 4. Identification using orbital satellites which monitor and take photographs of the satellite of interest. 5. Identification by analysing telemetry and radio data transmitted from SO. 6. Identification using a set of reflective characteristics in the radio and optical wavelengths (photometrical, polarization, spectral), which is typical for this class of satellites.

The physical characteristics, obtained from photometrical observations of GSS, used for identification are as follows:

Photometric characteristics. 1. The effective reflecting area ($S_{\gamma\lambda}$); 2. The spectral reflectance index (γ_λ). 3. The phase coefficient *β, (Δm/deg)*); 4. Colour-indices *(CI), (B-V, V-R)*. 5. The magnitude *m* reduced to a standard distance and phase angle (usually to $\psi = 0^0$ or $\psi = 25^0$).

Opto-geometric characteristics. The GSS linear dimensions. The prevailing shape of an object.

Dynamic characteristics. The period of rotation about the centre of mass or one of the axes. Instantaneous orientation in space, which is defined by the normal to the GSS reflective surface that produces flashes.

Physical characteristics of satellite platforms and payloads are not always known, but they can be determined from photometric observations. Problems with GSS photometry and the use of photometric data for the identification of GSS can be divided into two groups: technical and methodological.

2. Technical problems

1. Faint light of GSS: at the phase angle $\psi > 30^0$, the GSS is rather faint as its brightness is around 10^m -15^m. Therefore, it is advisable to use telescopes with the primary mirror diameter of at least 1 meter. Traditionally, to determine the GSS reflectance profile, it is necessary to conduct observations over a long period of time (from half-year, year) at different GSS positions relative to an observer. Basic observations are often limited due to weather conditions at observation sites.

However, there are some dates when it is possible to use telescopes with primary mirrors of 40-70 cm in diame-

ter for the photometry of GSS. Those are dates near the equinoxes, when a GSS enters and exits the Earth's shadow [2-4]. At that time, the GSS apparent brightness increases by $5^m - 10^m$ due to the so-called flash before entering and after exiting the Earth's shadow.

At this time, the GSS brightness increases by $5^m - 10^m$ due to the flash before entering and after exiting the Earth's shadow.

The flashes are created by quasi-mirror reflection of sunlight from the GSS surface, mainly from the solar arrays. Those flashes can be used to determine the object's payload [5] and orientation in space using the method suggested by V. Yepishev [6]. The number of such nights favourable for observations can be to 80 per year [7].

2. To register possible GSS rapid brightness changes, the obtained photometric measurements must be a minimum temporal resolution, a fraction of a second. In this case it is possible to use CCD run in storage mode for the rough photometry of three-axis stabilised GSSs, which change their brightness slowly. But using such CCD for the photometry of rapidly rotating GSS or space debris will result in smoothing small low-amplitude periodic effects on the light curve. The most relevant light detectors for this purpose are the following: 1) the use of CCD operated in TV mode with mode count pulses; 2) the use of the device immediate action photomultiplier (FEU) operating in the pulse-counting mode. The FEU is a single-channel device, but it has unexcelled advantages in its amplification factor ($>10^6$) and wide dynamic range ($>10^m$).

3. Multicolour photometry of GSS with the rapid changes of brightness; the time resolution is limited by the time the photometer switches the color filter.

3. Methodological problems

In the context of mathematical physics, the problem of identification by photometric observations can be solved in two ways.

Direct ways. The problem of calculating the brightness of the object from the known characteristics, such as shape, the laws of reflection, the orientation of the object, etc. In this case, we have a unique solution for any time.

Inverse ways. The determination of the object's shape by its light curve is an ill-posed inverse problem in mathematical physics. It does not correspond to the Hadamard criterion. We know only a part of the input information – brightness depending on the time F = *m (t)*. The output should be the object's shape as function $F = m(t) \, \Theta(X,Y,Z)$ with two arguments, i.e. the brightness of the time *m(t)* and angles of object's orientation $\Theta(X,Y,Z)$. In this case, the obtained results are characterised by the fact that small input changes can yield arbitrary large changes in the obtained results. In general, the solutions will be unstable, ambiguous or physically meaningless. The inverse problem solution depends on a large extent of the availability of a priori (physical) information on the object.

Several methods are used to reduce the reflectance profiles to $\psi = 0^0$. You can extrapolate the diffuse component of the light curve for $\psi = 0^0$, using a polynomial approximation. However, is possible to apply algorithm described in [8] where the GSS brightness is expressed by the formula:

$$m_\lambda = m_\lambda^\Theta - 2,5 \lg \left[\frac{S \gamma_\lambda F(\psi)}{d^2} \right],$$

where m_λ^Θ – is the magnitude of the Sun in a certain spectral range λ; S – is the GSS surface illuminated by the Sun and visible to an observer; γ_λ – is the spectral reflectance factor; $F(\psi)$ – is the phase function; ψ – is the satellite-centric phase angle; d – is the topocentric distance to the spacecraft; and $S \gamma_\lambda$ – is the effective reflecting area (ERA). All variables in the formula, except ERA, can be reliably measured or calculated from observations. $S\gamma_\lambda$ is a probabilistic variable. Incorrect determination of this variable leads to errors in calculation of other physical characteristics of GSS.

Experts use different ways of SO identification. They depend on the availability of a priori information about the SO observed. Therefore, the number of criteria for the identification of SO may be different. To identify an SO it is sometimes enough to determine 1-2 dynamic or reflection characteristics.

Let us present a brief overview of the most common methods for GSS identification by photometric data applied by the CIS experts. The methods for GSS identification used by Western experts from other countries are not given in the press.

1. The method for identification of low-orbit and high-orbit satellites developed in Uzhgorod, Ukraine, by V.P.Yepishev, I.I.Motrunich, Y.M.Motrunich, I.F.Naybauer et al.- is based on the on the complex approach to problem solving. The photometric data must be used together with positional observation data and colorimetric and polarimetric measurements applied when possible. That allows for determining the orientation of a satellite and individual fragments of its surface not only in space, but also relative to an observer and the GSS orbital plane. The authors developed nine criteria which makes it possible to achieve 80% probability of unknown satellite identification even when there is no a priori information on the SO [9].

2. The colour-index *(CI)* of an unknown spacecraft is the key characteristic of the idea developed by A.Murtazov, N.Nosova, V.Kupriyanov et al. (Ryazan, Rissia), as well V.Prokofieva (The Crimean Astrophysical Observatory). This *CI* is compared with the *CI* of known types of SOs. The phase coefficient should be applied when there is no similarity between *CIs*. Further, the comparison with mathematical simulation results for different geometric shapes is drawn and the scattered-field simulation is used [10, 11].

3. The methods by A.Didenko, B.Demchenko, L.Usoltseva et al. (Almaty, Kazakhstan). The reference data bank of photometric phase patterns is created for each GSS type. The phase pattern of an unknown GSS is compared with the bank data based on certain criteria. When it is impossible to identify an object, a phase pattern of a new GSS type is created for this object [12]. The identification procedure includes the following parameters: a phase factor – β, geometric albedo, ERA, spectral reflectance – γ_λ, period of light variation. Apply methods of the theory of pattern recognition [13].

4. The method by M.Smirnov, A.Bagrov, V.Vygon et al. (Moscow) are based on the study of the scattered field

formed by individual elements of the satellite structure. Implementation of this method requires conducting GSS observations over a long period at different phase angles [14]. The mathematical simulation is also applied. A.Bagrov also suggests carrying out GSS spectral observations to estimate the chemical composition of the GSS coating surface [15]. However, it is a sophisticated task to obtain a high-resolution spectrum of a faint GSS; maybe that is why the idea has not obtained a wide circulation.

5. A.Dobrovolsky, A.Korobko et al. (Odessa, Ukraine) have been exploring only the preliminary stage of identification by light curves at which they are divided into two groups: non-periodic and periodic light curves. Each group is broken down into several sub-groups. However, the accordance between the light curve groups and satellite types has not developed [16].

We can see that the solution of the ill-posed problems of GSS identification by photometric data is a long complicated process that requires additional information about the satellite. Such additional information can be the following: the satellite figure (configuration), its dimensions, the launch site and date, the orbit inclination to the equator, solar array power, nose-cone fairing dimensions, etc.

At the beginning of the 21st century, the main satellite systems remained the same as in 1980s. There is not much variety in satellite shapes; the design of their structures has been changed rather slowly. The evolution is driven mainly in towards the improvement of characteristics. As many experts noted, each GSS type has individual design features, which are representative and characterised by the light curve shape – signature. For example, the glare from

the scanning optics, the rotation around the axis, the type of stabilization, platform type, the size of the solar panels, and others. These features help to classify the spacecraft according to the light curve. The figures below, without going into the analysis, show the light curves of several geostationary objects with distinctive design and dynamic features characteristic of the respective spacecraft classes. The objects were observed by the authors at the calculated time for the flares maximum amplitude. Figure 1 – GSS "Sbirs GEO 2". Figure 2 – "DSP 18". Figure 3 – "Mentor 4". Figure 4 – tumble booster "Milstar 5R".

Many experts (see below) for identifying the GSS collect photometric database (DB) containing a set of characteristics with sufficient probability define a specific class of SO.The formation of such a DB is the problem of time and usage of uniform methodology for determining the physical characteristics of the SO. Such characteristics can be the following: ERA, phase coefficient β, spectral reflectance factors (γ_λ), CI, period of brightness variations, etc.

As proposed in the articles [13, 17], "the effective reflecting area is a rather important criterion, which can be used to identify a GSS type". It is known that the magnitude of the observed GSS mostly depends on two parameters: the ERA − $S\gamma_\lambda$ and phase angle − ψ. Hence, it may suggest taking ERA as a key characteristic of an SO. The ERA value will allow for the approximate estimation of what type the object belongs to. To simplify calculation of $S\gamma_\lambda$, it makes sense to bring ERA to the phase angle $\psi = 25^0$ or $\psi = 30^0$. At these ψ, the GSS brightness varies linearly. The phase coefficient β can be another important characteristic.
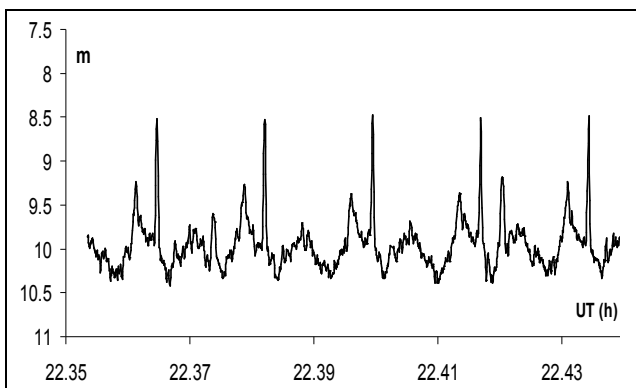
Figure 1: GSS "SBIRS GEO 2". 29/30.08.14
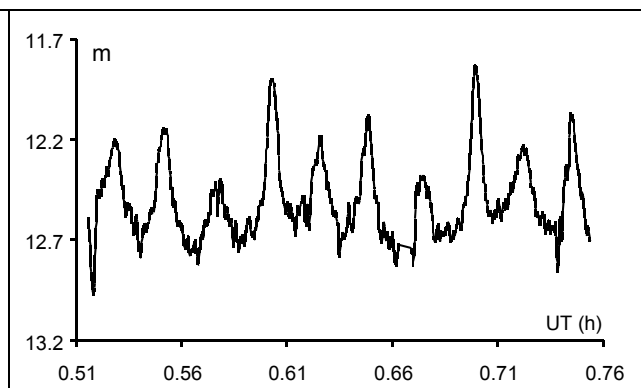
Figure 2: GSS "DSP 18". 28/29.09.14
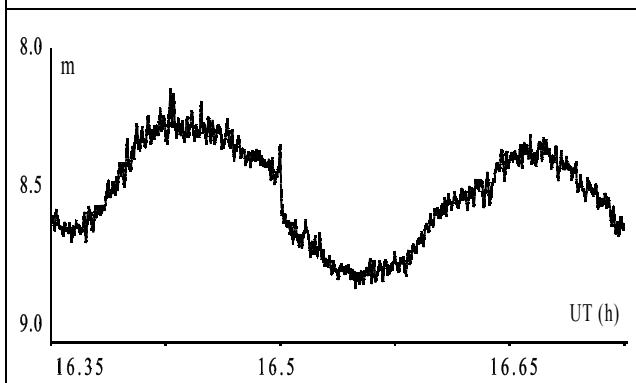
Figure 3: GSS "Mentor 4", 13/14.10.14
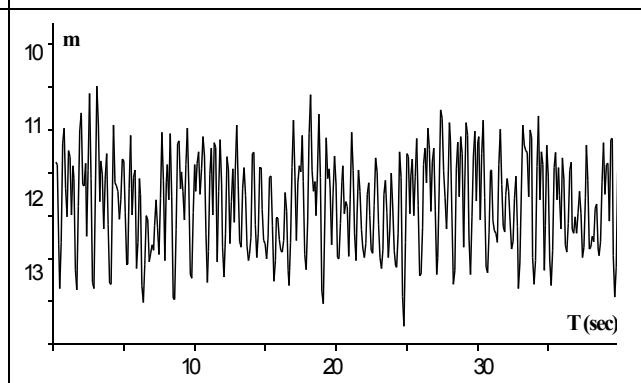
Figure 4: "Milstar 5R". 28/29.09.14

The division of characteristics into primary and secondary is relative and dependent on the availability and sufficiency of additional information on GSS. The further procedure of determination of other GSS physical characteristics depends on the final aim.

The large DB of standardised (B,V, R) physical characteristics of many GSS types is created and supported in the Fesenkov Astrophysical Institute (Almaty, Kazakhstan). The similar database of the Astronomical Observatory of I.I.Mechnikov, Odessa National University (Ukraine), contains data on more than 120 GSS and more than 800 light curves, and is updated every year. The "Kosmoten" station (Russia) DB consists of several thousands of light curves for many SO types. On the basis of AF USA – AMOS (Air Force Maui Optical and Supercomputing) intensively carried out are photometric, spectral, and polarization observations of different SO classes [18, 19]. However, the results of these studies are not known to us.

4. Conclusion

The database, additional information and simplification of input data when solving an inverse problem make it possible to identify an unknown satellite with a probability up to 80% using modern advanced methods [9].

References:

1. Kiladze R.I., Sochilina A.S. Theory of motion of geostationary satellites, S. Petersburg, 2008, 10.
2. Sukhov P.P, Karpenko G.F., Epishev V.P., Motrunych I.I.: 2009/2010, *Odessa Astron. Publ.*, **22**, 55.
3. Didenko A.V., Usol'tseva L.A.: 2002, Kosmicheskiye issledovaniya v Kazakhstane, Almaty: KazGosINTY, 355.
4. Didenko A.V., Usol'tseva L.A.: 2005, *Pervyye Fesenkovskiye chteniya «Sovremennaya astrofizika: traditsii i perspektivy»*, Almaty, 75 (in Russian).
5. Didenko A.V., Usol'tseva L.A.: 2008, *Izvestiya NAN RK, Seriya fiziko-matematicheskaya*, **4**, 96 (in Russian).
6. Yepishev V.P.: 1983, *Astrometriya i astrofizika AN SSSR*, 89 (in Russian).
7. Karpenko G.F., Murnikov B.A., Sukhov P.P.: 2009/2010, *Odessa Astron. Publ.*, **22**, 25.
8. Severnyy S.A., Smirnov M.A., Bagrov A.V.: 1986, *Nauchnyye informatsii*, **58**, M., 103 (in Russian).
9. Yepishev V.P., Isaak I.I., Motrunich I.I., Naybauer I.F., Novak E.I., Tsikavyy A.A.: 2005, *Sbornik trudov. Okolozemnaya astronomiya*, 267 (in Russian).
10. Murtazov A.K. Ekologiya okolozemnogo kosmicheskogo prostranstva, M.: FIZMATLIT, 2004; MAIK «Nauka / Interperiodika», 304 p. (in Russian).
11. Kuryshev V.I., Murtazov A.K.: 1985, *Nablyudeniya iskustvennykh nebesnykh tel*, 28 (in Russian).
12. Didenko A.V., Usoltzeva. L.A.: 2001, *Transaction of the KAU*, **2**, 83.
13. Didenko A.V., Usol'tseva L.A.: 2007, *Izvestiya NAN RK, Seriya fiziko-matematicheskaya*, **4**, 18 (in Russian).
14. Smirnov M.A. Fotometricheskiye nablyudeniya iskustvennykh nebesnykh tel //Diss. na Soiskaniye uchenoy stepeni doktora fiz.-mat. Nauk, Moskva, 1994, 163 p. (in Russian).
15. Bagrov A.V. Okolozemnaya astronomiya: issledovaniye iskustvennykh i yestestvennykh nebesnet tel v okolozemnom kosmicheskom prostanstve //Diss. na Soiskaniye uchenoy stepeni doktora fiz.-mat. Nauk, Moskva, 2002, 98-106 (in Russian).
16. Korobko A.A., Dobrovolsky A.V., Medvedev Y.A., et al.: 1999, in *Proc. Gamov memorial international conference*, Odessa, August 16-22, 122.
17. Yepishev V.P., Karpenko G.F., Sukhov P.P., Klabukova A.V., Volkov S.K.: 2009, *Okolozemnaya astronomiya*. Sbornik trudov konferentsii, Kazan', 22-26 Aug., M.: GEOS, 2010, 87 (in Russian).
18. Nishimoto D., Kissel K.E., Africano J.L., Lambert J.V., Kervin P.W.: 1993, in: *Proc. of the 1993 Space Surveillance Workshop. Project Report STK-206*, Vol. 1 //Ed. R.W.Miller & R.Sridharan, Lincoln Laboratory Massachusetts Institute of Technology, F19628-90-C-0002, p. 1-10.
19. Africano J., Kervin P., Sydney P., Hamada K., Soo Hoo V., Nishimoto D.: 2001, in: *Proc. of the Third European Conference on Space Debris*, 19-21 March 2001, Darmstadt, Germany //Ed. Huguette Sawaya-Lacoste. ESA SP-473, Vol.1, Noordwijk, Netherlands: ESA Publications Division, p. 107-112.

ON THE HEURISTIC RULE FOR PLANETARY DISTANCE DISTRIBUTION

N. D. Svyazhyn

I.I.Mechnikov Odessa National University
Odessa 65082, Ukraine, *swjashin@onu.edu.ua*

ABSTRACT. This paper presents a new heuristic rule for the planetary distance distribution in the solar system similar to the Titius-Bode rule of planetary orbit spacing. Application of this universal rule simultaneously for planets and planetary moons has been considered. Natural satellites orbiting around a central body are divided into groups of six satellites in each.

1. Introduction

There is a vast literature on the search of regularities of planetary and moon orbit spacing according to the Titius-Bode – type relation [1–8]. The Titius-Bode Law of Planetary Distances: Its History and Theory by Michael M. Nieto from the Niels Bohr Institute at the University of Copenhagen was issued in 1972. Apparently, the Titius-Bode relation expresses, to some extent, Newtonian mechanics in empirical form: each planet in the solar system is about 1.7 times further from the Sun than the next innermost planet. It was also shown that such regularities are realised in exoplanetary systems [2, 7]. The geometric series for distances follows from Newton's law; however, to perform sufficient simulation and deepen understanding of this phenomenon, it is necessary to rely on the methods of celestial mechanics and apply modern computer technologies. This study presents a new heuristic rule for the spacing of systems of different bodies in the solar system.

2. Rule definition

Natural satellites orbiting around a central body are divided into groups of six moons in each:

$$h_{m\,n}\,,\ \ n = \overline{1.6} \qquad (1)$$

where m – the group number; n – the ordinal number of a moon within a group starting with the central body; h_{mn} – the average distance between the central body and moon which equals to the radius of a sphere which has the same area as the planar figure restricted by the moon's orbit.

If $a,\ b$ – the ellipse semi – axes, then the sought radius equals to $\sqrt{ab}$. The distances in the group are approximated with the following formulae (see Table 1). (Here α_m – the group non – dimensional parameter; H_m – the average orbital radius of the 6th moon in the group, which is called the upper boundary of the group and h_{m1} – the lower boundary of a group. The distances h_{mn} within groups of moons are related as follows:

$$h_{m+k\ n} = \beta^{k} h_{m\ n}\,,\ \ \ k = 0, 1, 2, 3... \qquad (2)$$

where $m+k$ – the number of a group).

Having the relative values entered, the previous table can be presented as follows (see Table 2). As is evident, here

$$a_{m\,n} = \frac{h_{m\,n}}{h_{m\,6}} \ \ \text{and} \ \ \alpha_{m} = \frac{h_{m\,6}}{h_{m\,3}} \qquad (3)$$

Table 1

Moon number	1	2	3	4	5	6
Distance notation	h_{m1}	h_{m2}	h_{m3}	h_{m4}	h_{m5}	h_{m6}
Distance formula	$\dfrac{H_m}{\alpha_m^2 - 1}$	$\dfrac{H_m}{\alpha_m + 1}$	$\dfrac{H_m}{\alpha_m}$	$\dfrac{H_m}{\alpha_m - 1}$	$\dfrac{2\,\alpha_m\,H_m}{\alpha_m^2 - 1}$	H_m

Table 2

Moon	a_1	a_2	a_3	a_4	a_5	a_6
Distance formula	$\dfrac{1}{\alpha^2 - 1}$	$\dfrac{1}{\alpha + 1}$	$\dfrac{1}{\alpha}$	$\dfrac{1}{\alpha - 1}$	$\dfrac{2\alpha}{\alpha^2 - 1}$	1

Besides, it is supposed that the sequencing axiom is realised for planetary distances with any allowed values of the parameter α:

$$0 < a_{m\,n} = \frac{h_n}{h_6} < a_{m\,n+1} \le 1 \, , \; n = \overline{1,5} \qquad (4)$$

from which the left restriction for the parameter α is obtained:

$$1 + \sqrt{2} < \alpha_m \qquad (5)$$

From the sequencing axiom, which states that the upper boundary of the group is less than the lower boundary of the next group,

$$h_{m-1\,6} < h_{m\,n} \, , \quad n = 1, 2, 3, ...6 \qquad (6)$$

the right restriction is obtained:

$$\alpha < \sqrt{\beta + 1} \qquad (7)$$

Let us suppose that there are two Phaetons rather than one hidden in the asteroid belt at the distances of 2.26 and 2.94 AU from the Sun, and that asteroid Chiron ($a = 13.65$ AU, $e = 0.382$) is a minor planet (or its remainder). According to the above – formulated rule we receive the following (see Table 3).

Asteroid 538P – L with the average orbital radius of 2.261763 AU, asteroid 1992DT2 with the average radius of 2.9403035 AU and asteroid 1999W140 with the average radius 2.9399417 AU (or the members of the Flora and Eos families) were selected as the fragments of the 5th and 6th planets within the first group.

Thus, the values $\alpha_m \approx 2.94$, $m = 1, 2, 3$; $\beta \approx 13$ rather accurately approximate the relative distances

$$\frac{h_{m\,k}}{h_{m\,6}}, k = \overline{1.6}, m = \overline{1.3} \, ,$$ obtained on the basis of actual data.

The majority of the Kuiper belt asteroids are in the region extending between the orbits of the last planet of the second group and the second planet of the third group. The 3rd, 4th, 5th and 6th planets of the third group among trans – Neptunian objects do not belong to families.

3. Description of moon systems

To make it more illustrative, it is more convenient to examine the Neptunian moon system first (see Table 4).

As is seen from Table 4, the first four moons make up a family of the first object within the first group. Positions for the 4th and 5th objects within the first group are empty. The second group is completely empty.

The existence of positions in the second group is determined by the values β, which should meet some additional requirements (see Formula 8). Besides, a definite rule, such as density axiom, can be set: in accordance with this axiom parameters **α** and **β** should take on the least values given that conditions (2) and (6) are fulfilled.

In other words, when distributing moons within the first and third groups, the existence of the second group which fulfils condition (6) follows from condition (2).

Table 3

		PLANET	$h_3 = \beta h_2$ $\beta = 13.1$	AVERAGE RADIUS	RELATION WITHIN A GROUP	THEORETICAL RELATION	β
1	1	Mercury		.38294034	.130	.130	
	2	Venus		.722332359	.246	.254	
	3	Earth		.99993022	.340	.340	
	4	Mars		1.5203275	.5171	.516	
	5	The Flora family		(2.2616567)	.77	.77	
	6	The Eos family		(2.94)	1	1.	
2	1	Jupiter		5.208709	.134	.13	13.601882
	2	Saturn		9.5300711	.245	.25	13.175292
	3	Chiron		13.208832	.34	.34	13.209754
	4	Uranus		19.18058	.494	.52	12.616084
	5	Neptune		30.068409	.77	.77	13.258811
	6	Pluto		38.855936	1.	1.	13.352555
3	1	(229762) 2007 UK	68.234088	68.69	.139	.13	13.2
	2	(181902) 1999 RD, (82158) 2001FP	124.84393	105.564 157.7	.21 .319	.25	11.08
	3	(148209) 2009 CR	173.0357	169.644	.34	.34	12.85
	4	2004 VN	251.2656	243.365	.493	.52	12.69
	5	(90377) Sedna	393.89616	374.634	.76	.77	12.46
	6	2006 SQ	509.01276	493.24	1	1.	12.69

Table 4: The Neptunian moon system (Neptune's radius 24,764 km).

No	Group number	Object number within a group	Number within a family	Moon names	R, km	R/R	R/R theoretical	β	M, kg
1			1	**Naiad**	48 227	0.1359272			$1.9\cdot10^{17}$
2		**1**	2	**Thalassa**	50 075	0.1411358	0.11		$3.5\cdot10^{17}$
3			3	**Despina**	52 526	0.1480439			$2.1\cdot10^{18}$
4			4	**Galatea**	61 953	0.1746380			$2.1\cdot10^{18}$
5		**2**		**Larissa**	73 548	0.2072942	0.24		$4.9\cdot10^{18}$
6	**I**	**3**		**S/2004 N 1**	105 200	0.296505	0.32		
7				**Proteus**	117 647	0.3315858			$5.0\cdot10^{19}$
		4		*163.5*			0.46		
		5		*248.6*			0.70		
8		**6**		**Triton**	354 800	1.0000000	1.		$2.1\cdot10^{22}$
							α=3.17		
		1		*421 – 513.2*					
		2		*783 – 1060*					
	II	**3**		*1060 – 1252*					
		4		*1740 – 2108*					
		5		*2645 – 3500*					
		6		*3775 – 4240*					
								β=10.64	
9		**1**		**Nereid**	4 479 360.7	0.0992068	0.125	9.6401649	$3.1\cdot10^{19}$
		2		*11277.8*			0.25		
10		**3**		**Halimede**	14 249 954	0.315886	0.3(3)	11.007844	$9.0\cdot10^{16}$
11	**III**	**4**	1	**Sao**	21 924 105	0.4850029	0.5		$6.7\cdot10^{16}$
12			2	**Laomedeia**	22 433 384	0.4972924			$5.8\cdot10^{16}$
13		**5**		**Psamathe**	37 243 465	0.8255951	0.75		$1.5\cdot10^{16}$
14		**6**		**Neso**	45 111 053	1.0000000	1.	11.275853	$1.7\cdot10^{17}$
							α=3.0		

Now let us examine the Saturnian moon system:

Drawing an analogy between macrocosm and microcosm, in accordance with the planetary model of the atom in which an electron strives to occupy the lowest orbit from the allowed ones, it can be assumed that a similar phenomenon can be observed in macrocosm as it was in the case of the **β** parameter selection during assignment of the second group of the Neptunian moons. It means that the allowed orbits of a central body's moons are determined on the same ground.

As can be seen, the moons of the Saturnian system are divided into three groups.

The moons from the 0th to the 13th form a sub – group located between the orbits of the first and second moons within the first group. This group can be called a family or a sub – group of the first moon within the first group.

One of the criteria by which the moons were assigned to this group, is the moons' sizes given in the last column of the table as it is not feasible to perform any other assignment.

It should be noted that the 9th moon of the first family within the third group of the Saturnian system satisfies the following condition: $h_{3,1,9} = \beta h_{2,1} = 16938$ (see Table 5).

Further let us consider the moon system of Jupiter. Using the same principles as before, we obtain data presented in Table 6. The distance for the first moon of the first group of the Jupiter system is determined by relation $h_1 = \alpha_1 h_6$, although it is less than the central body's radius (see Table 6).

The Uranian moon system can be described with four groups (see Table 7).

In different sources, the solar and planetary parameters vary significantly. Table 8 presents some variations of those parameters, as well as the obtained values of parameters α and β.

Table 5: The Saturnian moon system (Saturn's radius 60,268 km).

No	Group number	Object number within a group	Number within a family	Moon name	R, thsd. km	R/R	R/R theoretical	β	D
1			0	S/2009 S 1	117	0.0957726			0,3
2			1	Pan	133	0.1088697			20
3		1	2	Daphnis	136.5	0.1117347	0.1011		7
5			4	Prometheus	139.4				100
14			13	Enceladus	238.1	0.1949014			499
15			1	Tethys	294.7				1060
16	I	2	2	Telesto	294.7	0.2412325	0.2326		24
17			3	Calypso	294.7				19
18			1	Dione	377.4				1118
19		3	2	Helene	377.4	0.3089282	0.3(3)		32
20			3	Polydeuces	377.4				4
21		4		Rhea	527.1	0.4314681	0.4348		1528
		5		*815*			0.6673		
22		6		Titan	1221.643	1. α=3.237	1. **α=3.3**		5150
23		1		Hyperion	1463.9814	0.1138775	0.1161	11.007	266
24		2		Iapetus	3560.1019	0.2769198	0.2439	12.08	1436
		3		*4147*			0.3226	*10.99*	
	II	4		*6122*			0.4762	*11.61*	
25		5	1	Kiviuq	10787.248	0.8390780	0.72	*13.23*	16
26			2	Ijiraq	10835.251	0.8428118			12
27		6		Phoebe	12856.073	1.	1. **α=3.1**	10.524	240
								β = 11.57	
28			1	Paaliaq	14669.37	0.5906256		1 : 10.02	22
29			2	Albiorix	15165.908			1 : 10.36	32
31		1	4	Bebhionn	**16088.201**			1 : 10.99	6
35			8	Skoll	**16626.089**	0.6694005		1 : 11.36	6
36			9	Siarnaq	17136.472	0.6899495			40
39			12	S/2004 S 7	17870.709	0.7195114		1 : 12.2	6
54			27	Farbauti	20170.152	0.8120917		1 : 13.78	5
57	III		30	Kari	20729.178	0.8345992		1 : 14.16	7
61			34	Loge	22860.661	0.9204171		1: 15.6	6
62			35	Fornjot	24837.282	1.0		1 : 16.97; 2: 6.98	6
		2		*39450 – 41190*					
		3		*50520 – 47980*					
		4		*70560 – 70832*					
		5		*109100 – 124809*				β = 11.57	
		6		*163535 – 148744*				β² = **133.8649**	

(α ≈ 3.2, β ≈ 11.57, αβ ≈ 37.024)

Table 6: The moon system of Jupiter (Jupiter's radius 71,492 km).

No	Diameter	Group number	Object number within a group	Number within a family	Moon name	Average radius, thsd. km	R/R	R/R theoretical	β	
		I	1		*20.49*			0.113		
			2		*43.89*			0.242		
			3		*57.67*			0.318		
			4		*84.70*			0.467		
1	~40		5	1	**Metis**	127.69	0.7040459	0.709		
2	~16			2	**Adrastea**	128.69	0.7955960			
3	~146		6		**Amalthea**	181.366	1.0	1.0		
								α=3.14		
4	~98	II	1		**Thebe**	221.872	0.1178490	0.15	*10.83*	
5	~3630		2		**Io**	421.7	0.2239892	0.26	*9.6*	
6	~3121,6		3		**Europa**	671.02	0.3564174	0.36	*11.64*	
7	~5262,4		4		**Ganymede**	1070.412	0.5685575	0.56	*12.64*	
			5		*1543.8*			0.82	*12.09*	
8	~4820,6		6		**Callisto**	1882.68	1.0	1.0	10.38	
								α=2.8	β=11.2	
		III	1		*2196 – 2622* **β ф2485**			0.1153123		
			2		*4634 – 5531* **β u4723**			0.243309		
9	8		3		Themisto	7309.11	0.3214949	0.3214949	10.89	
10	10		4	1	**Leda**	11108.66				
11	170			2	**Himalia**	11385.86	0.5008128	0.4739336	10.63	
12	86			3	**Elara**	11664.67				
13	36			4	**Lysithea**	11688.92				
14				5	S/2000 J 11	12435.16				
15	1		5	1	S/2003 J 12	16787.83		0.7172426	*10.87*	
16	3			2	Carpo	16814.85	0.7396097		*10.89*	
17	2		6	1	Euporie	19044.30			10.11	
22	2			6	Thelxinoe	20074.99			10.66	
32	28			16	**Ananke**	20787.92			/каллисто=11.04	
33	4			17	Hermippe	20898.75			11.10	
34	4			18	Thyone	**21055.91**	**β к=21086**		β=10.86	$K_{26}·β$
38				22	S/2003 J 10	22027.12			/каллисто=11.69	
51	60			35	**Pasiphae**	22734.76	1.00000000 –	1.0	/каллисто=12.08	
54	46			38	**Carme**	22873.13			/каллисто=12.15	
64	38			48	**Sinope**	23589.52			/каллисто=12.53	
65	4			49	Isonoe	23610.92			/каллисто=12.54	
								α=3.11		
66	5	IV	1	1	Megaclite	24080.92			10.418	
67				2	S/2003 J 2	30018.99			11.6318	
			2		*52900*					
			3		*81900*					
			4		*12750*					
			5		*17300*					
			6		*254600*					
					β=11.02			α=3.11		

(α ≈ 3.04, β ≈ 11.2, αβ ≈ 34.05)

Table 7: The Uranian moon system (the radius of Uranus is 24,800 km).

No	R thsd. km	Group number	Object number within a group	Number within a family	Moon name	r/r	β	β	Theoretical r/r
	13.83		1						0.18445
	21.22		2						0.28295
	29.6		3						0.3946
1	49.751000			1	Cordelia	0.6510206			
2	53.762629		4	2	Ophelia	0.7035151			0.652
7	66.097000			7	Portia	0.8649175			
8	69.927000		5		Rosalind	0.9150353			0.935
9	74.800000	I		1	Cupid	0.9788013			
10	75.255000		6	2	Belinda	0.9847553			1.
11	76.420000			3	Perdita	1. α=2.5342			
							β=6.25		
12	86.004000		1		Puck	0.1473864	6.23		0.126
13	97.734000				Mab	0.1674378			
14	129.389950		2		Miranda	0.2217652	6.09		0.251
15	191.019930		3		Ariel	0.327335	6.453		0.334
16	266.298930	II	4		Umbriel	0.4563838	5.32		0.5
17	435.909790		5		Titania	0.7470.	6.236		0.75
18	583.519630		6		Oberon	1. α=2.99	7.637		1.
			1		*618 – 656*				
			2		*819 – 1113*				
			3		*1209 – 1228*				
		III	4		*1685 – 1743*				
			5		*2438 – 2758*				
			6		*3067 – 3692*				
								β = 6.39	
19	4254.116700		1		Francisco	0.2139946		6.59	
20	7218.710300		2		Caliban	0.3631319		7.469	
21	7961.082700		3	1	Stephano	0.4			
22	8410.678200			2	Trinculo	0.423		6.359	
23	11297.873000		4	1	Sycorax	0.5682881			
24	11316.714000	IV		2	Margaret	0.569		6.519	
25	15801.542000		5	1	Prospero	0.795			
26	16239.657000			2	Setebos	0.8169		6.1	
27	19879.088000		6		Ferdinand	1. . α=**2.42** – 79		5.837	
						α=2.42			

(α ≈ 2.65, β ≈ 6.32, αβ ≈ 16.75)

Table 8: Dynamic parameters of the Sun and solar system planets.

Planetary names	The core temperature, T	Volume (V), cub. m	I_O	I_O *	α	β	αβ
Sun	$1.35 - 1.5 \cdot 10^7$	$1.41 \cdot 10^{27}$	0.171	0.34	2.94	13.1	38.514
Jupiter	$20 - 25 \cdot 10^3$	$14.3 - 15.2 \cdot 10^{23}$	0,20	0.262	3.04	11.2	34.05
Saturn	$11.7 - 20 \cdot 10^3$	$8.27 - 9.23 \cdot 10^{23}$	0,22	0.227	3.2	11.57	37.024
Uranus	$4.737 - 12 \cdot 10^3$	$6.39 - 6.833 \cdot 10^{22}$	0,23	0.212	2.65	6.32	16.75
Neptune	$7 - 14 \cdot 10^3$	$6,254 - 6.58 \cdot 10^{22}$	0,26	0.2	3.1	10.64	32.984

Here I_O is the reduced moment of inertia.

Table 9: The S parameter values for the solar system giants and the Sun.

Planetary names	The core temperature, T	Volume (V) cub. m	I_0	$\alpha\beta$	S	S~
Sun	$1.35 \cdot 10^7$	$1{,}41 \cdot 10^{27}$	0.34	38.514	$0.07977 \cdot 10^{20}$	$0.08 \cdot 10^{20}$
Jupiter	$25 \cdot 10^3$	$1{,}43 \cdot 10^{24}$	0.2	34.05	$0.08399 \cdot 10^{20}$	$0.08 \cdot 10^{20}$
Saturn	$12.15 \cdot 10^3$	$8{,}27 \cdot 10^{23}$	0.22	37.024	$0.08356 \cdot 10^{20}$	$0.08 \cdot 10^{20}$
Uranus	$2.45 \cdot 10^3$	$6{,}833 \cdot 10^{22}$	0.2	16.75	$0.08325 \cdot 10^{20}$	$0.08 \cdot 10^{20}$
Neptune	$1.2 \cdot 10^3$	$6{,}254 \cdot 10^{22}$	0.2	32.984	$0.08302 \cdot 10^{20}$	$0.08 \cdot 10^{20}$

The given values of the parameter S indirectly sustain the planetary spacing rule.

Having the values **T**, **V** and **I_O** selected (from Table 8), we see that the parameter **S**, determined by the following formula:

$$S = \frac{V}{T0} \frac{1}{I\alpha\beta} , \qquad (8)$$

takes on close values for planet – giants and the Sun.

4. Conclusions

Formally, α, in the units of the 3rd moon, is the upper boundary of the first group or the distance to the 6th moon. Then, αβ is the distance to the 6th moon within the next group or the upper boundary of the second group.

Thus, a set of values α and β can be determined from formulae (1) – (7) using two radii of the orbits of moons assigned to the given positions. Comparing these values with the values of T, V and I_O in formula (8), the fittest parameter values can be found.

References

1. Bakulev V.M. The Titius-Bode law of planetary distances: new approach (arXiv:astro-ph/0601369 2006astro.ph..1369B).
2. Cuntz Manfred: 2012, *Publications of the Astronomical Society of Japan*, **64**, No.4, Article No.73, 10 pp.
3. Griv E.: 2006, *European Planetary Science Congress*. Berlin, Germany, 18–22 September 2006, p.22.
4. Hayes Wayne, Tremaine Scott: 1998, *Icarus*, **135**, Issue 2, pp. 549-557.
5. Kotliarov I. The Titius-Bode Law Revisited But Not Revived (arXiv:0806.3532 2008arXiv0806.3532K).
6. Pankovic Vladan, Radakovic Aleksandar-Meda. A Close Correlation between Third Kepler Law and Titius-Bode Rule (arXiv:0903.1732 2009arXiv0903.1732P).
7. Poveda A., Lara P.: 2008, *Revista Mexicana de Astronomía y Astrofísica,* **44**, 243-246 (http://www.astro-scu.unam.mx/~rmaa/).
8. Zawisawski Z., Kosek W., Leliwa-Kopystyski J.: 2000, *A&AT*, **19**, Issue 2, 177-190.

THE SOLAR-RADIATION PRESSURE EFFECTS ON THE ORBITAL EVOLUTION OF ASTEROID MOONS

V.V. Troianskyi, O.A. Bazyey

Astronomical Observatory, Odessa National University
Shevchenko Park, Odessa 65014, Ukraine
v.troianskyi@onu.edu.ua, o.bazyey@onu.edu.ua

ABSTRACT. In the theory of motion, disturbances are divided into gravitational and non-gravitational ones. In this paper, we discuss the effects of solar-radiation pressure on the orbital evolution of asteroid moons.

It is known from the laws of physics that the smaller an object is the more pressure is exerted on it by solar radiation. That is the reason why asteroid moons with their small sizes are exposed to the solar-radiation pressure so much.

Key words: asteroid, asteroid moons, orbital evolution.

1. Equation of motion

To improve the accuracy of the theory of motion of asteroid moons, it is necessary to account for the effects of the solar-radiation pressure on their surfaces. For this purpose, the acceleration due to the solar-radiation pressure was expanded (Duboshin, 1971):

$$a_{Lpx} = \left(1+k\right)q\frac{S}{m}\Psi\left(\frac{a}{r_0}\right)\frac{x_{St}-x_S}{r_0}$$

$$a_{Lpy} = \left(1+k\right)q\frac{S}{m}\Psi\left(\frac{a}{r_0}\right)\frac{y_{St}-y_S}{r_0} , \qquad (1)$$

$$a_{Lpz} = \left(1+k\right)q\frac{S}{m}\Psi\left(\frac{a}{r_0}\right)\frac{z_{St}-z_S}{r_0}$$

$$r_0 = \sqrt{\left(x_S-x_A\right)^2+\left(y_S-y_A\right)^2+\left(z_S-z_A\right)^2} , \quad (2)$$

where k – the albedo; $q = 4,5605 \cdot 10^{-6}\frac{N}{m^2}$ - the solar

constant; S – the cross-sectional area of the asteroid moon; m – the asteroid moons' mass; Ψ – the shadow function; α – the mean distance from the asteroid to the Sun; x_A, y_A, z_A – the asteroid's coordinates; x_S, y_S, z_S – the Sun's coordinates; x_{St}, y_{St}, z_{St} – the asteroid moon's coordinates.

As a result the differential equations describing the motion of the asteroid moon in the asteroid-centric inertial coordinate frame can be formularized as follows:

$$\frac{d^2x}{dt^2} - a_{Lpx} = 0$$

$$\frac{d^2y}{dt^2} - a_{Lpy} = 0 , \qquad (3)$$

$$\frac{d^2z}{dt^2} - a_{Lpz} = 0,$$

where x, y, z – the position vector components; t – time; a_{Lp} – the acceleration due to the solar-radiation pressure.

To integrate differential equations of motion, the 15th order Everhart method was employed (Bazyey et al., 2009).

2. Shadow function

The conception of the shadow function Ψ was suggested by Ferraz-Mello in 1963 (Duboshin, 1971). This function equals to 1 when the natural satellite is illuminated by the Sun, and it is zero when the moon is in the shadow. At a first approximation, the shadow is reckoned to be cylindrical-shaped; but when higher accuracy is required, it is assumed that the shadow is cone-shaped.

Let us set the shadow function as Ψ . Then, for the cylindrical-shaped shadow we obtain the following:

$$\Psi = \begin{cases} 0, -\varphi < \lambda < \varphi, \\ 1, -\pi < \lambda < -\varphi, \varphi < \lambda < \pi. \end{cases} \qquad (4)$$
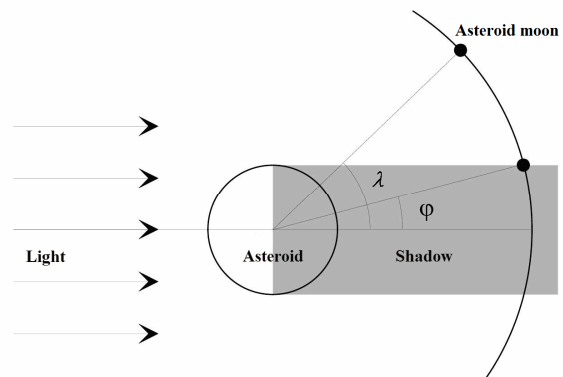
Figure 1: Geometric representation of the cylindrical-shaped shadow.
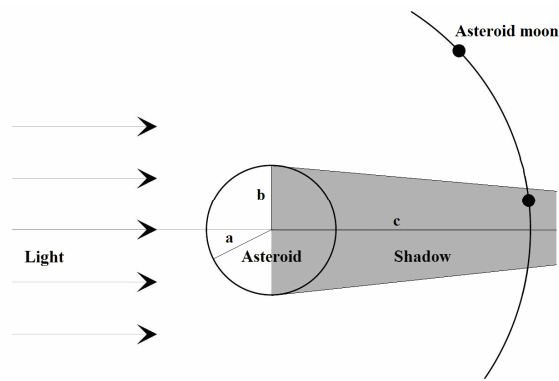
Figure 2: Geometric representation of the cone-shaped shadow.

Figure 4: Changes in the longitude of ascending node of natural satellite Beta in asteroid system (66391) 1999KW4.

In our model the shadow is supposed to be represented as cone-shaped; that enables to determine more accurately the instants when an asteroid moon enters into and exits from the shadow.

$$\Psi = \begin{cases} 0, \dfrac{x_S^2}{a^2} + \dfrac{y_S^2}{b^2} - \dfrac{z_S^2}{c^2} = 0, \\[2mm] 1, \dfrac{x_S^2}{a^2} + \dfrac{y_S^2}{b^2} - \dfrac{z_S^2}{c^2} = 1. \end{cases} \qquad (5)$$

where a, b, c – the cone axes. The compression of the body casting a shadow is also accounted for the shadow shape.

3. Orbital evolution of asteroid moons

As an example, we integrated the equations of motion of the moon of asteroid (66391) 1999 KW4 (http://www.johnstonsarchive.net/astro/astmoons/am-66391.html) over 1000-year interval accounting for the shadow function. The integration step is 6 minutes with the integration error 10^{-7} m.

As can be seen from the results obtained, only orbital inclination and the ascending node longitude have a secular component of the disturbance by the acceleration due to the solar-radiation pressure. The orbital inclination changes by 1 degree every 900 years while the longitude of the ascending node changes by 0.5 degree every 75 years. That can be also seen in Figs. 3 and 4.

4. Results

The obtained results show that the orbital inclination and longitude of the ascending node increase secularly; hence, it can be concluded that the acceleration due to the solar-radiation pressure is one of the reasons why asteroid moons go into retrograde orbits. For instance, the orbital inclination of the moons in asteroid systems (22)Kalliope (Margot et al., 2003), (93)Minerva (Marchis et al., 2013), (66391)1999KW4 (Ostro el al., 2006) and (153591)2001 SN263 (Fang et al., 2001) exceeds 90°.

To sustain this hypothesis, further more detailed investigation of the indicated asteroid systems over a longer interval of time is required.

References

Bazyey A.A., Kara I.V.: 2009, *Visnyk Astronomichnoyi shkoly*, **6/2**, 155 (in Ukrainian).

Duboshin G.N.: 1971, *Reference Guide on Celestial Mechanics and Astrodynamics*.

Fang J., Margot J.-L., Brozovic M., Nolan M.C., Benner L.A.M., Taylor P.A.: 2011, *Astron. J.*, **141**, 154.

Margot J.L., Brown M.E.: 2003, *Science*, **300**, 1939.

Marchis F. et al.: 2013, *Icarus*, **224**, 178.

Ostro S.J. et al.: 2006, *Science*, **314**, 1276.

Figure 3: Changes in the orbital inclination of natural satellite Beta in asteroid system (66391)1999KW4.

H$_\alpha$ LINE AS AN INDICATOR OF ENVELOPE PRESENCE AROUND THE CEPHEID POLARIS Aa ($\alpha\ UMi$)

I.A. Usenko,[1] A.S. Miroshnichenko,[2] V.G. Klochkova,[3] N.S. Tavolzhanskaya,[3]

[1] Astronomical Observatory, Odessa National University
   T.G.Shevchenko Park, Odessa 65014 Ukraine, *igus@deneb1.odessa.ua*
[2] Dpt of Physics and Astronomy, University of North Carolina
   Greensboro, NC 27402-6170, USA *a_mirosh@uncg.com*
[3] Special Astrophysical Observatory, Russian Academy of Sciences
   Nizhnij Arkhyz, Karachaevo-Cherkessia, 369167 Russia *valenta@sao.ru; panch@sao.ru*

ABSTRACT. We present the results of the radial velocity (RV) measurements of metallic lines as well as H$_\alpha$ (H$_\beta$) obtained in 55 high-resolution spectra of the Cepheid α UMi (Polaris Aa) in 1994–2010. While the RV amplitudes of these lines are roughly equal, their mean RV begin to differ essentially with growth of the Polaris Aa pulsational activity. This difference is accompanied by the H$_\alpha$ core asymmetries on the red side mainly (so-called knifelike profiles) and reaches the value of 8–12 km/s in 2003 with subsequent decrease to 1.5–2 km/s. We interpret so unusual behaviour of the H$_\alpha$ line core as dynamical changes in the envelope around Polaris Aa.

Key words: - Stars: Cepheids - Stars: radial velocities - Stars: H$_\alpha$ absorption line - Stars: envelopes - Stars: individual - α UMi (Polaris A)

1. Introduction

Detecting the extended envelope around the Cepheid Polaris (hereafter Polaris Aa) using a near-infrared interferometer (Mérand et al. 2006) suggested an idea to check its presence spectroscopically. Usenko et al. (2013, 2014ab), Usenko and Klochkova (2015) revealed that the H$_\alpha$ absorption line could be used as an indicator of the envelope presence not only in long-period Cepheids but also in short-period ones. As a rule, Cepheids with pulsational periods longer than 7–10^d demonstrate a pronounced appearance of the secondary variable absorption in the H$_\alpha$ cores, thereas short-period ones be noted by more smoothed, so called knifelike form. Besides, a slight change in the RV of the H$_\alpha$ core with pulsational phase compared to that determined from the metal lines is another indicator of the envelope presence in Cepheids.

Hence the main goal of this work is to measure the RVs of Polaris Aa in different pulsational phases using the metal lines and H$_\alpha$ (in some cases H$_\beta$) line cores and to estimate visually the form of the latter ones.

2. Observations

Observations of Polaris Aa have been obtained using:

1. 1 m telescope of the Ritter Observatory, University of Toledo (Toledo, OH, USA) - fiberfed echelle spectrograph 1150×1150 pixel CCD ($\lambda\lambda$ 5800–6800 Å).

2. 2.1 m Otto Struve telescope of the McDonald Observatory (Texas, USA) - SANDIFORD spectrograph (McCarthy et al. 1993) 1200×400 pixel CCD ($\lambda\lambda$ 5500–7000 Å).

3. 6 m telescope BTA - SAO RAS (Russia) - LYNX (Panchuk et al. 1993), PFES (Panchuk et al. 1997), NES (Panchuk et al. 2006) spectrometers ($\lambda\lambda$ 4470–7100 Å.)

The data reduction was made using IRAF and MIDAS software packages, all measurements of the RV were done using the DECH20 software (Galazutdinov 1992). In Table 1 we present these RV data from the spectra obtained in 2005–2010. This table contains the measurements determined from the metal lines, H$_\alpha$ and H$_\beta$, respectively.

2. Radial velocity measurement analysis and the H$_\alpha$ line cores behaviour

As seen in Table 1 and Fig. 1, originally the difference between the measurements obtained from metal lines and H$_\alpha$ (and one H$_\beta$) for each spectrum does not exceed 1.5 km/s in 1994. As seen from Fig. 2, the H$_\alpha$ core does not demonstrate any visible asymmetries.

Table 1: Radial velocity data of Polaris Aa in 1994–2010

Spec-trum	HJD 2400000+	Tele-scope	Metallic lines			H$_\alpha$	H$_\beta$
			RV	σ	NL	RV	RV
940609	49512.615	1	-13.28	1.23	126	-14.78	-
940815	49579.824	1	-14.21	1.21	116	-15.53	-
940908	49603.853	1	-13.35	0.93	152	-	-14.34
941012	49637.792	1	-14.97	1.05	132	-16.69	-
941023	49648.810	1	-14.38	1.07	130	-15.53	-
s22923	51240.612	3	-18.26	2.81	302	-19.98	-
s23908	51360.538	3	-16.51	2.36	317	-16.48	-
s24008	51361.536	3	-14.53	2.68	275	-15.33	-16.82
011009	52192.858	2	-16.88	0.81	281	-19.23	-
020522	52416.655	1	-16.53	1.17	138	-18.18	-
020523	52417.616	1	-17.67	1.45	145	-19.35	-
020527	52421.679	1	-17.85	1.32	109	-19.46	-
020601	52426.667	1	-18.18	1.28	121	-20.39	-
020602	52427.650	1	-17.35	3.06	119	-18.33	-
020610	52435.634	1	-16.53	1.18	142	-19.19	-
020616	52441.673	1	-16.78	1.08	112	-20.35	-
s36713	52514.575	3	-20.39	0.92	270	-22.54	-
s36814	52515.588	3	-15.33	0.86	396	-	-15.77
s40008	52782.543	3	-16.62	0.60	374	-	-16.41
031013	52833.741	1	-21.64	1.30	93	-14.25	-
031017	52837.678	1	-21.59	6.07	104	-17.13	-
031019	52839.746	1	-23.97	4.00	111	-15.07	-
s40410	52861.560	3	-17.76	0.73	279	-20.47	-
s40819	52867.562	3	-17.75	0.79	251	-20.25	-
s40921	52869.570	3	-16.62	0.76	247	-19.08	-
s41209	52891.600	3	-16.38	0.89	384	-	-15.76
031109	52952.700	1	-19.19	1.37	90	-7.46	-
0312131	52986.692	1	-18.48	1.89	125	-10.53	-
0312132	52986.709	1	-17.86	1.67	107	-9.31	-
040101	53005.595	1	-16.50	1.13	141	-8.17	-
s42006	53015.167	3	-17.79	0.88	279	-19.81	-
s42202	53019.108	3	-17.28	0.82	266	-19.22	-
s42302	53072.165	3	-17.81	0.64	251	-20.09	-
s42327	53072.631	3	-18.02	0.77	291	-20.17	-
s42421	53073.622	3	-17.52	0.80	278	-19.69	-
s42502	53131.194	3	-18.21	0.98	549	-18.40	-
s43302	53246.192	3	-16.50	0.73	281	-19.22	-
s43812	53285.167	3	-17.08	0.85	304	-19.06	-
041227	53367.091	2	-20.51	3.84	261	-23.39	-
s45233	53686.647	3	-17.68	1.05	198	-	-17.54
s45328	53687.637	3	-15.82:	1.00	616	-	-16.48
s45511	53689.649	3	-18.24	1.20	589	-18.60	-
s45602	53690.111	3	-17.80	1.13	566	-17.50	-
s45821	53691.635	3	-17.82	1.06	550	-17.34	-
s45902	53693.124	3	-17.93	1.06	549	-18.41	-
s463002	53751.123	3	-16.83	1.21	581	-	-16.72
s466002	53808.277	3	-18.78	1.55	933	-	-19.43
s469012	53904.348	3	-17.87	1.09	506	-	-17.21
s478030	53980.588	3	-17.40	1.29	569	-17.20	-
s482001	54073.591	3	-18.43	1.15	579	-17.88	-
s485029	54077.653	3	-17.58	1.21	406	-	-17.27
s494030	54169.639	3	-19.18	1.09	415	-	-20.09
s497012	54225.226	3	-18.92	1.25	592	-18.59	-
s504049	54344.551	3	-19.41	1.04	464	-18.47	-
s510001	54426.185	3	-16.65	1.19	603	-16.26	-
s532015	54934.587	3	-17.19	1.10	573	-16.61	-

1 - 1m Ritter Observatory;

2 - 2.1m McDonald Observatory;

3 - 6m Special Astrophysical Observatory, Russian Academy of Sciences.

Figure 2: H$_\alpha$ line core profiles of Polaris Aa during 1994–1999.
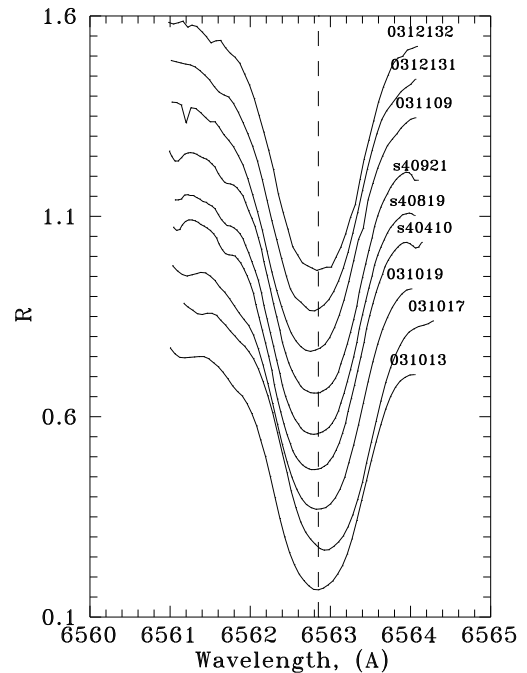
Figure 3: H$_\alpha$ line core profiles of Polaris Aa during 2003

Figure 1: Radial velocity estimates of Polaris Aa during 1994–2010. Six-point stars, - estimates from metal lines, open five-point stars, - from H$_\alpha$ line, open circles, - from H$_\alpha$ line. A square polynomial approximation is drawn for the metal lines.

Since 1999 (HJD 2451240–2451361), this difference begins to increase (Fig. 1) and a slight asymmetry on the red side of the H$_\alpha$ core are visible (Fig. 2). Two years later this difference becomes larger (from 1 km/s to 2 km/s), and the asymmetries on the red side of
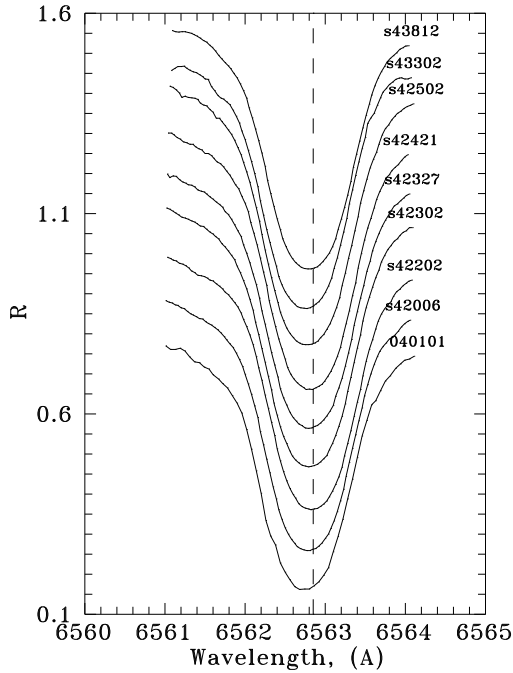
Figure 4: H$_\alpha$ line core profiles of Polaris Aa during 2004
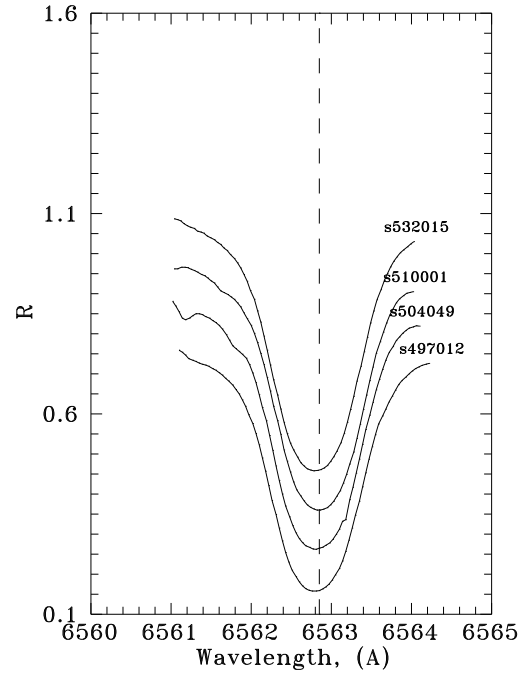
Figure 6: H$_\alpha$ line core profiles of Polaris Aa during 2008–2010
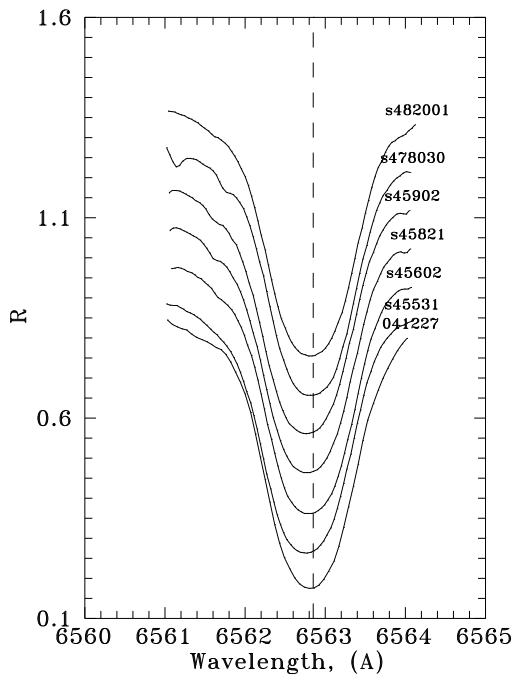
Figure 5: H$_\alpha$ line core profiles of Polaris Aa during 2005–2006

the core get quite visible (Fig. 3) during two years (2001–2002).

During 2003 we can see the most interesting event when the difference between the measurements reaches 8–12 km/s (see Table 1 and Fig. 1) and the H$_\alpha$ core

shows asymmetries on the red side as well as on the blue side (see Fig. 4).

Since 2004 this difference decreases to 2–2.5 km/s (HJD 2453015–2453367), and the H$_\alpha$ core exhibits asymmetries on the red side only (see Fig. 1 and 5).

During 2005–2006 (HJD 245689–2454073) the difference is less than 1 km/s and the asymmetries are less visible (Fig. 6). The same one can see in other results obtained during 2008–2010 (HJD 2454077–2454934) (Fig. 7). It should be noted that the differences between the H$_\alpha$ and H$_\beta$ measurements are negligible.

3. Conclusions

We can summarize the results of our investigations as follows.

1. As seen from the results of Table 1 and Fig.1, amplitudes of the RV curve from H$_\alpha$ and H$_\beta$ are very small and close to those determined from the metallic lines.

2. First H$_\alpha$ line core asymmetries on the red side arise with an increase of the RV curve amplitude after the historical minimum of the Polaris Aa pulsational activity in the beginning of the 1990s.

3. During 2003 the difference between the RV estimates obtained from metal lines and the H$_\alpha$ core reaches 8–12 km/s. This event is accompanied by

the pronounced asymmetries of the H_α core on the red side as well as on the blue side.

4. Since 2004, the H_α core asymmetries are observed on the red side only and nearly disappear after 2005, when RV amplitude grows to the new minimum.

5. H_α core asymmetries (so-called knifelike profile) in the Polaris Aa atmosphere show that this absorption line could be an indicator of the envelope presence in yellow pulsating supergiants with short periods and small amplitudes.

6. So unusual behaviour of the H_α core during 2003 could be explained by dynamical changes in the envelope around of Polaris Aa.

References

Galazutdinov G.A.: 1992, *Preprint SAO RAS*, **No.92**, 1.

McCarthy J.K., Sandiford B.A., Boyd D., Booth J.: 1993, *PASP*, **105**, 881.

Mérand A., Kervella P., Coudé du Foresto V., Perrin G. et al.: 2006, *A&A*, **453**, 155.

Panchuk V.E., Klochkova V.G., Galazutdinov G.A., Radchenko V.P., Chentsov E.L.: 1993, *AstL*, **19**, 431.

Panchuk V.E., Najdenov I.D., Klochkova V.G., Ivanchik A.B., Yermakov S.V., Murzin V.A.: 1997, *Bull. SAO RAS*, **44**, 127.

Panchuk V.E., Klochkova V.G., Nadenov I.D., Yushkin M.V.: 2006, *The Ultraviolet Universe: Stars from Birth to Death, 26th Meeting of the IAU, Joint Discussion 4, 16-17 Aug. 2006, Prague, Czech Republic*, **D04**, 14.

Usenko I.A., Kniazev A.Yu., Berdnikov L.N., Kravtsov V.V., Fokin A.B.: 2013, *AstL*, **39**, 432.

Usenko I.A., Kniazev A.Yu., Berdnikov L.N., Fokin A.B., Kravtsov V.V.: 2014a, *AstL*, **40**, 435.

Usenko I.A., Kniazev A.Yu., Berdnikov L.N., Kravtsov V.V.: 2013b, *AstL*, **40**, 800.

Usenko I.A., Klochkova V.G.: 2015 *AstL*, **41**, 351.

MODEL OF DEGENERATE DWARF WITH SPIN-POLARIZED ELECTRON SYSTEM

M.V. Vavrukh, D.V. Dzikovskyi, N.L. Tyshko

Dpt of Astrophysics of Ivan Franko National University of Lviv,
Ukraine, *mvavrukh@gmail.com*

ABSTRACT. A three-parametric model of a massive degenerate dwarf was proposed. Unlike paramagnetic state of electron system in the standard Chandrasekhar model electrons are considered in a partially spin-polarized state. The parameters of the model are: x_0 – the relativism parameter at stellar centre, $\mu_e = \langle \frac{Z}{A} \rangle$ – the average chemical composition parameter and ζ – the degree of spin polarization of the electron system. The macroscopic characteristics (e.g. mass, radius, energy) as functions of the model parameters were obtained from the solution of the mechanical equilibrium equation. The electron spin polarization was shown to lead to the increase of stellar radius and especially to mass compared with the corresponding characteristics of the standard model. The application of the proposed model to interpreting the stability of massive dwarfs in binary system was discused.

Key words: degenerate dwarf, electron system, spin polarization, relativism parameter, chemical composition parameter, mechanical equilibrium equation.

PACS 97.20Rp, 97.60Bw

1. Introduction

In the past two decades dwarfs with different characteristics were discovered with the help of the space telescopes. Therefore the problem of developing the general theory of white dwarfs, including hot dwarfs with great luminosities and dwarfs with great masses, became urgent. The correct consideration of the interparticle interactions and of the general relativity effects leds to the conclusion that the maximum of the dwarf mass, in which the stability is disturbed, is a few percent less than the weight limit, which is derived in standard Chandrasekhar model (Vavrukh et al., 2014). At the same time the observed data indicate the avaibility in a binary system of dwarfs with masses, which are very close to the Chandrasekhar limit, or exceed it. The search of the mechanism, which can provide the stability of dwarfs with great masses, is one of the urgent tasks for these objects. In this work, we proposed a model of the cold degenerate dwarfs with spin-

polarized electron system, which corresponding magnetic field. The homogeneous magnetic field does not affect directly the star mechanical equilibrium, but it may cause the redistribution of electrons by energies as the result of spins interaction with the field. The result is two subsystems of electrons, with opposite spins, each of which has its Fermi sphere. At absolute zero the temperature has the distribution of electrons by the wave vectors:

$$n_{\mathbf{k},\sigma} = \theta(k_F^\sigma - k), \quad \sigma = \pm 1, \tag{1}$$

where $k_F^+ > k_F, k_F^- < k_F$, k_F – Fermi waveguide number in paramagnetic model with the same general concentration of electrons.

The defining of partial electron concentrations in these two subsystems is determined by the ratios

$$n_+ = \frac{1}{V} \sum_{\mathbf{k}} n_{k,+}, \quad n_- = \frac{1}{V} \sum_{\mathbf{k}} n_{k,-}. \tag{2}$$

We introduce the value

$$\zeta = \frac{1}{n}(n_+ - n_-), \quad n = n_+ + n_-, \tag{3}$$

which determines the degree of spin-polarization of electron system. From the equation (3) we have found that

$$n_+ = \frac{n}{2}(1 + \zeta), \quad n_- = \frac{n}{2}(1 - \zeta). \tag{4}$$

With the ratios (2) we introduce the expression for the waveguides of Fermi numbers for both systems

$$k_F^+ = k_F \lambda_+, \quad k_F^- = k_F \lambda_-, \quad k_F = (3\pi^2 n)^{1/3},$$
$$\lambda_+ = (1 + \zeta)^{1/3}, \quad \lambda_- = (1 - \zeta)^{1/3}. \tag{5}$$

The model described here was considered in many works, devoted to the equation of solid state physics

both at $T = 0K$, and at low temperatures. The electron subsystem here consideres not non-relativistic, but thermodynamic characteristics calculated taking into account the electron interactions (Hong & Mahan, 1995; Tanaka & Ichimaru, 1989; Ortiz & Ballone, 1994; Ortiz & Ballone, 1997).

2. The dwarf mechanical equilibrium equation

The equation of model (1) – (5) state is derived by a simple generalization equation of state for paramagnetic system (Vavrukh et al., 2011). The equation of state in the spatially two-component homogeneous case of the electron-nuclear model at $T = 0K$ has a parametric representation:

$$P(x) = \sum_{\sigma} P_{\sigma}(x), \quad P_{\sigma}(x_{\sigma}) = \frac{\pi m_0^4 c^5}{3h^3} \mathcal{F}_{\sigma}(x_{\sigma}),$$

$$\mathcal{F}_{\sigma}(x_{\sigma}) = 4 \int_0^{x_{\sigma}} \frac{dy\, y^4}{(1+y^2)^{1/2}}, \quad (6)$$

$$\rho(x) = m_u \mu_e \sum_{\sigma} n_{\sigma} = \frac{m_u \mu_e}{6\pi^2} \left(\frac{m_o c}{\hbar}\right)^3 \sum_{\sigma} x_{\sigma}^3,$$

where $x_{\sigma} = \hbar k_F^{\sigma}/m_0 c$ – is relativism parameter, m_u – mass nuclear unit, $\mu_e = \langle \frac{Z}{A} \rangle$ – the average chemical composition, (Z – nuclear charge, A – mass number), m_0 – electron mass, c – speed of light, $P_{\sigma}(x)$ – the electron partial pressure, $\rho(x)$ – mass density of the nuclear subsystem. The pressure ratio in a spin-polarized model to the pressure in the paramagnetic model equals: $C_1(\zeta) = \frac{1}{2} \sum_{\sigma} \lambda_{\sigma}^4$ at the border $x \gg 1$ and $C_2(\zeta) = \frac{1}{2} \sum_{\sigma} \lambda_{\sigma}^5$ at the border $x \ll 1$. From this follows that the pressure in the spin-polarized model is greater than the pressure in the paramagnetic model at the same value x, and the functions $C_1(\zeta), C_2(\zeta)$ change within the limits: $1 \leq C_1(\zeta) \leq 2^{1/3}, 1 \leq C_2(\zeta) \leq 2^{2/3}$.

To obtain the equation of state for inhomogeneous model, we should perform replacement $x \to x(r), P_{\sigma} \to P_{\sigma}(x(r)), \rho \to \rho(r), x_{\sigma} \to x_{\sigma}(r)$. According to the formulas (5), $x_{\sigma}(r) = x(r)\lambda_{\sigma}$, where $x(r) = \hbar k_F(r)(m_0 c)^{-1}$ – is the relativism parameter value in a paramagnetic state.

Let us consider the mechanical equilibrium of star

$$\frac{dP(r)}{dr} = -G\rho(r)\frac{M(r)}{r^2}, \quad \frac{dM(r)}{dr} = 4\pi r^2 \rho(r), \quad (7)$$

where $P(r)$ – is the pressure on the sphere of radius r, $\rho(r)$ – density on this sphere, $M(r)$ – mass inside the sphere. The system of equations (7) is reduced to the nonlinear differential equation for $x(r)$,

$$\frac{1}{r^2}\frac{d}{dr}\left\{ r^2 \left[\frac{\lambda_+^5}{\sqrt{1+x^2(r)\lambda_+^2}} + \frac{\lambda_-^5}{\sqrt{1+x^2(r)\lambda_-^2}} \right] \times \right.$$
$$\left. \times\, x(r)\frac{dx}{dr} \right\} = -G(m_u \mu_e)^2 \frac{64\pi^2 m_0^2 c^4}{3(hc)^3} x^3(r), \quad (8)$$

where λ_+, λ_- – are the prescribed parameters, and $\lambda_+ + \lambda_- = 2$.

3. Full polarization case

In the particular case of full polarization, when $\zeta = 1$ ($\lambda_- = 0$, $\lambda_+ = 2^{1/3}$), in dimensionless variables

$$\xi = \frac{r}{\lambda}, \quad y_+(\xi) = (\varepsilon_0^+)^{-1}\{[1 + \lambda_+^2 x^2(r)]^{1/2} - 1\} \quad (9)$$

the equation (8) coincides its form with the equation of paramagnetic model

$$\frac{1}{\xi^2}\frac{d}{d\xi}\left\{ \xi^2 \frac{dy_+}{d\xi} \right\} = -\left\{ y_+^2(\xi) + \frac{2}{\varepsilon_0^+}y_+(\xi) \right\}^{3/2}, \quad (10)$$

however in this equation parameter $x_0\lambda_+$ is used instead of x_0. Herewith the scale λ_+ is determined by the ratio

$$\frac{16G\pi^2}{3(ch)^3}[m_u \mu_e m_0 c^2 \varepsilon_0^+ \lambda]^2 = 1, \quad (11)$$

where $\varepsilon_0^+ = [1 + x_0^2 \lambda_+^2]^{1/2} - 1$. The total mass of dwarf is determined by the ratio

$$M(x_0^+, \mu_e) = \frac{\sqrt{2}}{\mu_e^2} M_0 \,\mathcal{M}(x_0^+),$$

$$\mathcal{M}(x_0^+) = \int_0^{\xi_1(x_0^+)} d\xi\, \xi^2 \left(y_+^2(\xi) + \frac{2}{\varepsilon_0^+}y_+(\xi) \right)^{3/2}. \quad (12)$$

Herewith $\xi_1(x_0^+)$ – the dimensionless radius of a dwarf, which is determined from the condition $y(\xi_1(x_0^+)) = 0$. From the last formula it follows that the maximum mass of a dwarf which corresponds $x_0 \gg 1$, is equal

$$M_{max} = \sqrt{2}\frac{M_0}{\mu_e^2}\, 2{,}01824\cdots, \quad (13)$$

that is, it exceeds Chandrasekhar limit by $\sqrt{2}$ times. The radius of dwarf is equal

$$R(x_0^+, \mu_e) = \xi_1(x_0^+)\lambda = \frac{R_0 \xi_1(x_0^+)}{\mu_e}\frac{\sqrt{2}}{\varepsilon_0^+}. \quad (14)$$

The scales of mass and radius (M_0, R_0) are used in the formulas (13), (14) defined by the formulas

$$
\begin{aligned}
R_0 &= \left(\frac{3}{2}\right)^{1/2}\frac{1}{4\pi}\left(\frac{h^3}{cG}\right)^{1/2}\frac{1}{m_0 m_H}, \\
M_0 &= \frac{m_0 c^2 \lambda \varepsilon_0(x_0)}{G m_H} = \left(\frac{3}{2}\right)^{1/2}\frac{1}{4\pi}\left(\frac{hc}{Gm_H^2}\right)^{3/2} m_H.
\end{aligned}
\tag{15}
$$
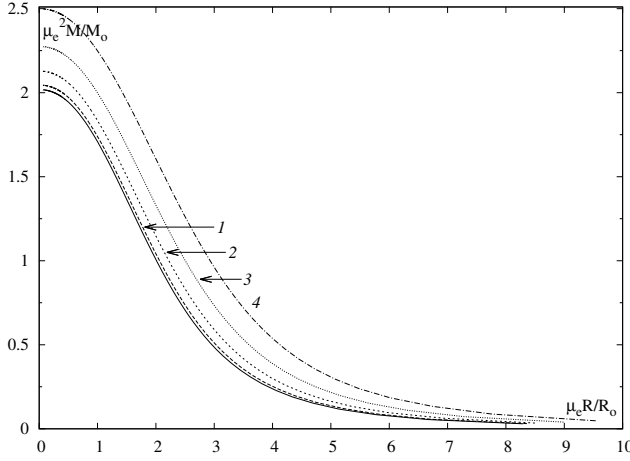
Figure 1: "Mass-radius" relations at different values ζ ($\zeta = 0$ – solid curve, $\zeta = 0.2$ – curve 1, $\zeta = 0.4$ – curve 2, $\zeta = 0.6$ – curve 3, $\zeta = 0.8$ – curve 4)

As it can be seen from the ratio (14), the radius of dwarf values in the ultrarelativistic region ($x_0 \gg 1$) $R(x_0^+, \mu_e) \Rightarrow R_0 \cdot 6{,}89685 \cdot 2^{1/2}(\mu_e x_0 \lambda_+)^{-1}$ exceeds the analogous value at the same concentration in the star centre by $2^{1/2}\lambda_+^{-1} = 2^{1/6}$ times. In figure 1 the "mass-radius" relations obtained in the standard (solid curve) and spin-polarized models at different values of the parameter ζ, are compared to each other.

4. The equilibrium equation solutions at arbitrary polarization

In a general case at arbitrary value of the parameter ζ, the equation (8) also can be reduced to the equation (10) using the substitution

$$
\begin{aligned}
\sum_{\sigma=\pm}\lambda_\sigma^3 \{(1 + x^2(r)\lambda_\sigma^2)^{1/2} - 1\} &= \varepsilon_0^\zeta y(\xi), \\
\text{where} \qquad\qquad\qquad & \\
\varepsilon_0^\zeta &= \sum_{\sigma=\pm}\lambda_\sigma^3 \{(1 + x_0^2(r)\lambda_\sigma^2)^{1/2} - 1\}.
\end{aligned}
\tag{16}
$$

To record the right side of the equation (8) by $y(\xi)$, we define $x(r)$ from the ratio (16). We reduce this ratio to the biquadratic equation. Positive and valid root of this equation is written as

$$
x(r) = 2^{-1/2}(\lambda_+^8 + \lambda_-^8)^{-1}[b(y) - \varphi(y)]^{1/2}, \tag{17}
$$

$$
\begin{aligned}
b(y) &= 2\{(\lambda_+^8 + \lambda_-^8)[(\varepsilon_0^\zeta y)^2 + 4\varepsilon_0^\zeta y] + \\
&\quad + 4(\lambda_+\lambda_-)^3(\lambda_+^5 + \lambda_-^5)\}, \\
\varphi(y) &= \{b^2(y) - 4ac(y)\}^{1/2} = \\
&= 4(2 + \varepsilon_0^\zeta y)(\lambda_+\lambda_-)^3\{(\lambda_+\lambda_-)^2 \times \\
&\quad \times [(\varepsilon_0^\zeta y)^2 + 4\varepsilon_0^\zeta y] + (\lambda_+^5 + \lambda_-^5)^2\}^{1/2}.
\end{aligned}
\tag{18}
$$

At the limit of star $y(\xi) = 0$, therefore $b(0) = \varphi(0) = 8(\lambda_+\lambda_-)^3(\lambda_+^5 + \lambda_-^5)$, and this provides the implementation of the equality $x(R) = 0$ at the arbitrary value ζ.

The equation (8) in a dimensionless form is

$$
\begin{aligned}
\frac{1}{\xi^2}\frac{d}{d\xi}\left(\xi^2\frac{dy}{d\xi}\right) = -\big\{\sqrt{2}(\lambda_+^8 + \lambda_-^8)^{-1}\times \\
\times (\varepsilon_0^\zeta)^{-1}[b(y) - \varphi(y)]^{1/2}\big\}^3.
\end{aligned}
\tag{19}
$$

The boundary conditions to $y(0) = 1$, $y'(0) = 0$, and the condition $y(\xi) \geq 0$ corresponds to this equation. The scale λ is determined by the ratio

$$
\frac{32\pi^2 G}{3(hc)^3}\left\{m_u\mu_e m_0 c^2\lambda\frac{\varepsilon_0^\zeta}{2}\right\}^2 = 1, \tag{20}
$$

which at the limit $\zeta \to 0$ coincides with the equality in the paramagnetic model.

The equation (19) – is two-parametric, with the parameters x_0 and ζ. The equation (19) takes the form of the equation (10) in the case of large values of x_0

$$
\frac{1}{\xi^2}\frac{d}{d\xi}\left(\xi^2\frac{dy}{d\xi}\right) \approx -\left\{y^2(\xi) + \frac{4}{\varepsilon_0^\zeta}y(\xi)\right\}^{3/2}, \tag{21}
$$

the parameter λ is determined by the equality

$$
\frac{64\pi^2 G}{3(hc)^3}\{m_0 c^2\lambda\varepsilon_0^\zeta m_u\mu_e\}^2(\lambda_+^4 + \lambda_-^4)^{-3} = 1. \tag{22}
$$

The equation solutions dependence (19) on the parameters x_0, ζ is illustrated figures 2 and 3, and the figure 4 shows the dependence of the dimensionless radius of star $\xi_1(x_0, \zeta)$ on these parameters.

4. The macroscopic characteristics of dwarfs

The equation solutions (19) determine the macroscopic characteristics of star dependence on the parameters of model x_0, μ_e, ζ. In particular the total mass of star is equal to
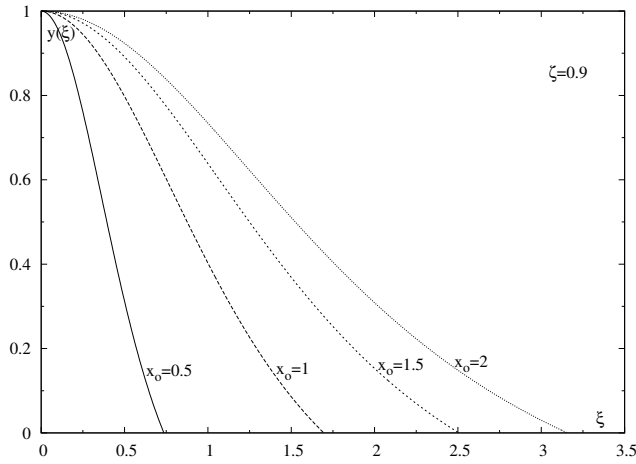
Figure 2: The equation solutions (19) at fixed value $\zeta = 0.9$
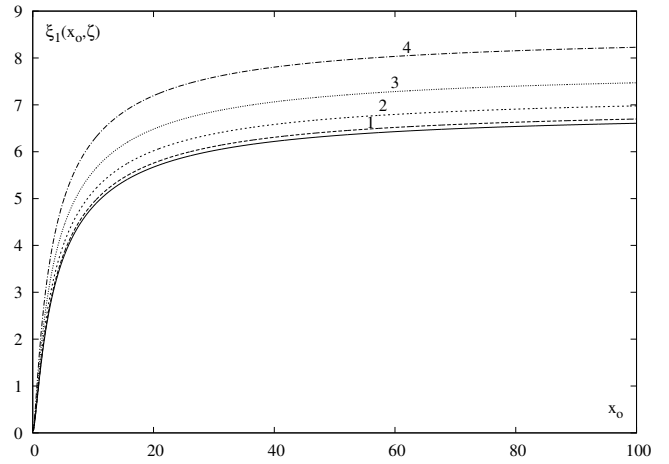
Figure 4: Dependence $\xi_1(x_0, \zeta)$ of the dimensionless star radius on parameter x_0 at different values ζ ($\zeta = 0$ – solid curve, $\zeta = 0.2$ – curve 1, $\zeta = 0.4$ – curve 2, $\zeta = 0.6$ – curve 3, $\zeta = 0.8$ – curve 4)
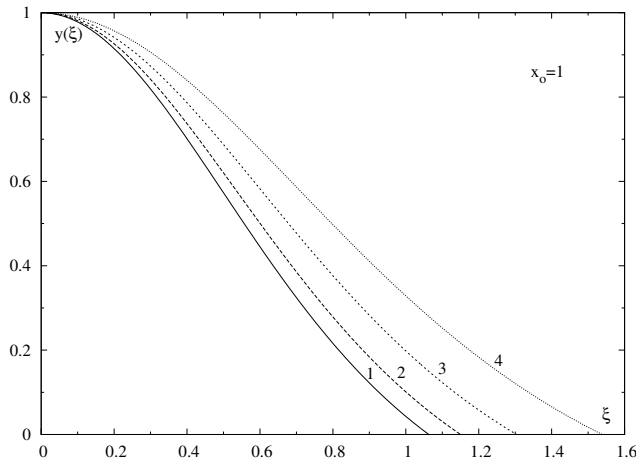
Figure 3: The equation solutions (19) at fixed value $x_0 = 1$ ($\zeta = 0$ – solid curve, $\zeta = 0.2$ – curve 1, $\zeta = 0.4$ – curve 2, $\zeta = 0.6$ – curve 3, $\zeta = 0.8$ – curve 4)
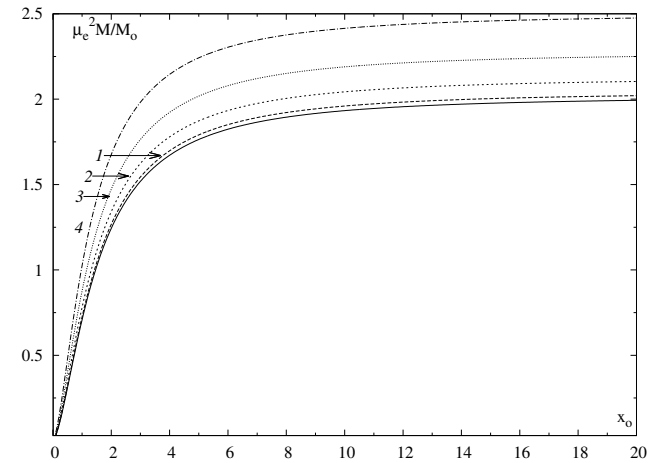
Figure 5: The mass dependence on parameter x_0 at different values ζ ($\zeta = 0$ – solid curve, $\zeta = 0.2$ – curve 1, $\zeta = 0.4$ – curve 2, $\zeta = 0.6$ – curve 3, $\zeta = 0.8$ – curve 4)

$$
M(x_0, \mu_e|\zeta) = \frac{M_0}{\mu_e^2} \mathcal{M}(x_0|\zeta),
$$

$$
\mathcal{M}(x_0|\zeta) = 2\sqrt{2}\{\varepsilon_0^\zeta(\lambda_+^8 - \lambda_-^8)\}^{-3} \times
$$

$$
\times \int_0^{\xi_1(x_0|\zeta)} d\xi\, \xi^2\, [b(y(\xi)) - \varphi(y(\xi))]^{3/2} = \tag{23}
$$

$$
= \xi_1^2(x_0|\zeta)\left|\frac{dy}{d\xi}\right|_{\xi=\xi_1(x_0|\zeta)}.
$$

The radius is determined by the ratio

$$
R(x_0, \mu_e|\zeta) = \lambda\xi_1(x_0|\eta) = 2R_0\frac{\xi_1(x_0|\zeta)}{\mu_e\varepsilon_0^\zeta}. \tag{24}
$$

The $\mathcal{M}(x_0|\zeta)$, $R(x_0, \mu_e|\zeta)$ dependence on the parameter x_0 is illustrated in figures 5, 6.

The average value of the electron kinetic energy E_{kin}, the potential energy of nuclear subsystem W gravitational interaction, and the total energy (taking into account the electrons rest energy) $\tilde{E}$ is determined by the ratios
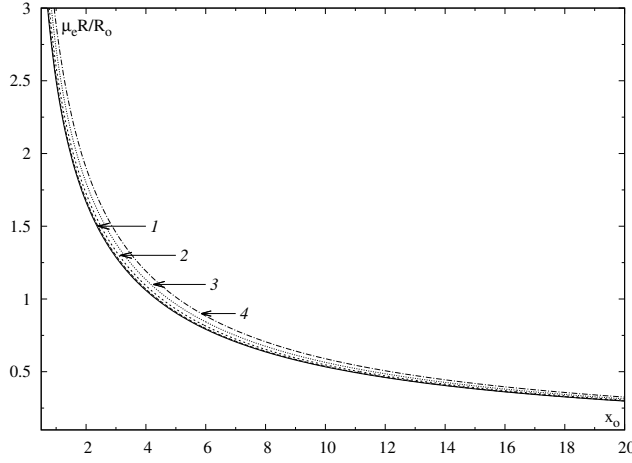
Figure 6: The radius dependence on parameter x_0 at different values ζ ($\zeta = 0$ – solid curve, $\zeta = 0.2$ – curve 1, $\zeta = 0.4$ – curve 2, $\zeta = 0.6$ – curve 3, $\zeta = 0.8$ – curve 4)

Figure 8: The total energy $\tilde{E}$ dependence on parameter x_0 at different values ζ ($\zeta = 0$ – solid curve, $\zeta = 0.2$ – curve 1, $\zeta = 0.4$ – curve 2, $\zeta = 0.6$ – curve 3, $\zeta = 0.8$ – curve 4)
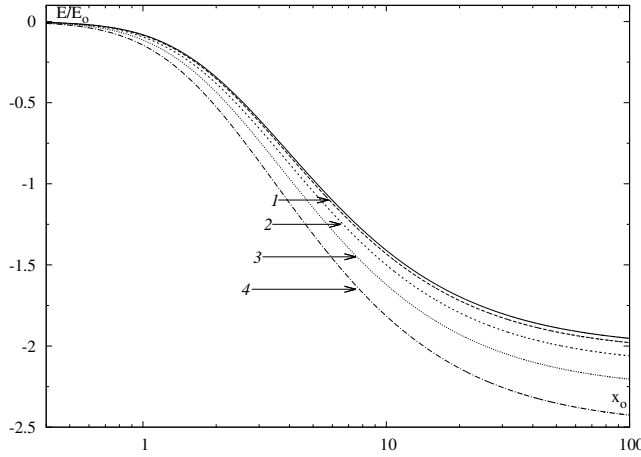
Figure 7: The total energy E dependence on parameter x_0 at different values ζ ($\zeta = 0$ – solid curve, $\zeta = 0.2$ – curve 1, $\zeta = 0.4$ – curve 2, $\zeta = 0.6$ – curve 3, $\zeta = 0.8$ – curve 4)

$$E(x_0, \mu_e|\zeta) = E_{kin}(x_0, \mu_e|\zeta) + W(x_0, \mu_e|\zeta) =$$

$$= \frac{E_0}{2\mu_e^3} \left(\frac{2}{\varepsilon_0^\zeta}\right)^3 \int_0^{\xi_1} d\xi \, \xi^2 \times$$

$$\times \sum_\sigma \left\{ x_\sigma^3(\xi)[(1 + x_\sigma^2(\xi))^{1/2}] - \mathcal{F}_\sigma(x_\sigma(\xi)) \right\},$$

$$\tilde{E}(x_0, \mu_e|\zeta) = E_{kin}(x_0, \mu_e|\zeta) + W(x_0, \mu_e|\zeta) +$$

$$+ m_0 c^2 N(x_0, \mu_e|\zeta) = \frac{3}{4} \cdot \frac{E_0}{\mu_e^3} \left(\frac{2}{\varepsilon_0^\zeta}\right)^3 \sum_\sigma \int_0^{\xi_1} d\xi \, \xi^2 \times$$

$$\times \left\{ x_\sigma(\xi)[(1 + x_\sigma^2(\xi))]^{1/2} - \ln[x_\sigma(\xi) + (1 + x_\sigma^2(\xi))^{1/2}] \right\}.$$

Herewith $x_\sigma(\xi)$ is determined by the equation (17), where $y(\xi)$ – the equation solution (19).

It is likely that the model has a physical meaning with a small value of the parameter polarization ($\zeta \ll 1$). In this case the equation (19) is simplified, because with precision to ζ^2

$$\lambda_+^5(1 + x^2(r)\lambda_+^2)^{-1/2} + \lambda_-^5(1 + x^2(r)\lambda_-^2)^{-1/2} =$$
$$= 2(1 + x^2(r))^{-1/2} \cdot \{1 + \zeta^2 \cdot f(x(r)) + \cdots\}, \quad (26)$$
$$f(x) = \frac{5}{9} - \frac{1}{2}x^2(1 + x^2)^{-1} + \frac{1}{6}x^4(1 + x^2)^{-2}.$$

Proceeding to dimensionless variables

$$r = \lambda\xi, \quad \mu(r) = m_0 c^2\{(1 + x_0^2)^{1/2} - 1\}y(\xi), \quad (27)$$

We summarize the equation (19) to this dimensionless form:

$$E_{kin}(x_0, \mu_e|\zeta) = \frac{E_0}{\mu_e^3} \left(\frac{2}{\varepsilon_0^\zeta}\right)^3 \int_0^{\xi_1} d\xi \, \xi^2 \frac{1}{2} \times$$

$$\times \sum_\sigma \left\{ x_\sigma^3(\xi)[(1 + x_\sigma^2(\xi))^{1/2} - 1] - \frac{1}{4}\mathcal{F}_\sigma(x) \right\},$$

$$W(x_0, \mu_e|\zeta) = \frac{E_0}{\mu_e^3} \left(\frac{2}{\varepsilon_0^\zeta}\right)^2 \int_0^{\xi_1} d\xi \, \xi^3 \, x^3(\xi)\frac{dy}{d\xi} = \quad (25)$$

$$= -\frac{3}{4} \cdot \frac{E_0}{\mu_e^3} \left(\frac{2}{\varepsilon_0^\zeta}\right)^3 \int_0^{\xi_1} d\xi \, \xi^2 \frac{1}{2} \sum_\sigma \mathcal{F}_\sigma(x_\sigma(\xi)),$$

$$\frac{1}{\xi^2}\frac{d}{d\xi}\left\{\xi^2\frac{dy}{d\xi}\right\} = -\left(y^2 + \frac{2}{\varepsilon_0}y\right)^{3/2} +$$
$$+ \frac{1}{6\xi^2}\frac{d}{d\xi}\left\{\xi^2\frac{(y^2 + \frac{2}{\varepsilon_0}y)(2y^2 + \frac{4y}{\varepsilon_0} + \frac{1}{\varepsilon_0^2})}{(y + \frac{1}{\varepsilon_0})^4}\frac{dy}{d\xi}\right\}. \quad (28)$$

Herewith the scale λ is determined by the ratio

$$\frac{32\pi^2 G(m_u\mu_e m_0 c^2 \lambda \varepsilon_0)^2}{3(hc)^3} = 1 + \frac{5}{9}\zeta^2. \quad (29)$$

The equation solution (28) can be found by successive approximations for small values ζ, using substitution

$$y(\xi) = y_0(\xi) + \zeta^2 y_1(\xi). \quad (30)$$

The mass and radius of dwarf dependence on parameters of model is given by

$$M(x_0, \mu_e, \zeta) \cong \frac{M_0}{\mu_e^2}\left(1 + \frac{5}{6}\zeta^2\right)\mathcal{M}(x_0),$$
$$R(x_0, \mu_e, \zeta) \cong \frac{R_0}{\mu_e \varepsilon_0}\left(1 + \frac{5}{18}\zeta^2\right)\xi_1(x_0), \quad (31)$$

where $\mathcal{M}(x_0), \xi_1(x_0)$ are the characteristics of standard model (paramagnetic).

5. Summary and conclusions

The degree of spin polarization of the dwarf electron system significantly affects its characteristics as it follows from the calculations, it leads to the increase the mass and radius. At an arbitrary value ζ the maximum dwarf mass exceeds this value in the standard model. Within the spin-polarized model the existence of dwarfs in binary systems can be explained, where the dwarfs mass reaches the value $1,5M_\odot$ and it is at the limit of stability (or beyond it) in terms of the standard model (Vavrukh et al., 2012). Above we considered a somewhat idealized model, in which the parameters μ_e and ζ are constants independent of the coordinates. From physical considerations, the degree of spin-polarization electron subsystem depends on the temperature and magnetic field values. Obviously, the global magnetic field has a dipole character, and therefore it is concentrated in the external star regions. Thereby the degree of spin polarization is greater in the outer dwarf regions. In term of strong accretions on the massive magnetic dwarf, in its surface layers thermonuclear reaction can start, which will lead to their heating and reducing the degree of spin polarization. There may be the conditions, in which the mass of star exceeds the permissible critical mass (which is a function of ζ), resulting in the collapse and supernova explosion. Hence follows the need for accurate description of a dwarf within the model with the parameter ζ, which is a function of the distance from the star center, as well as the consideration of other factors – interparticle interactions and the effects of general relativity theory.

References

Hong S., Mahan G.D.: 1995, *Phys. Rev. B.*, **51**, 24, 17417.

Ortiz G., Ballone P.: 1994, *Phys. Rev. B.*, **50**, 3, 1391.

Ortiz G., Ballone P.: 1997, *Phys. Rev. B.*, **56**, 15, 9970.

Tanaka S., Ichimaru S.: 1989, *Phys. Rev. B.*, **39**, 2, 1036.

Vavrukh M.V., Tyshko N.L., Smerechynskyj S.V.: 2011, *AJ*, **88**, 6, 549.

Vavrukh M., Tyshko N., Shabat B.: 2012, *Visnyk of the Lviv University. Series Physics*, **47**, 204 (in Ukrainian).

Vavrukh M.V., Tyshko N.L., Smerechynskyj S.V.: 2014, *Visnyk of the Lviv University. Series Physics*, **49**, 83 (in Ukrainian).

ANALYSIS OF SELF – GRAVITATING PLANETARY SATELLITES IN THE SOLAR SYSTEM

S.O.Yasenev

Dpt of Aerospace Surveying, National Aviation University
Kyiv, Ukraine, *yasenev91@gmail.com*

ABSTRACT. As of today there have been more than 180 planetary satellites discovered in the Solar system, and the number of outer moons found continues to grow. Most of those natural satellites have insufficient mass and are able to retain their shape only due to the strength of the electromagnetic force. The purpose of this paper is to analyze the moons' physical properties. The analysis of planetary satellites as self – gravitating bodies, i.e. celestial bodies which rely on the weight of their own mass and resulting gravitational force to maintain their shape and tend to bring it closer to the hydrostatic equilibrium, was performed.

Key words: planetary satellites; gravitational field; shape; mass; classification.

1. Introduction

Modern astronomical observations carried out by space – and ground – based means resulted in the discovery of a large number of planetary satellites – more than 180, and this number continues to grow. But most of these moons have small masses while their shape and size are kept fixed by the strength of electromagnetic interactions in their composite minerals. Due to that all small planetary satellites are irregular in shape [2, 5].

On the other side, the planets in the Solar System also have massive moons that keep their spherical shape by their own gravity; in other words, the gravitational field and proper rotation had a paramount importance during their evolution. It is evident that those moons significantly differ from smaller ones, most of which have been discovered over the last twenty years (Fig. 1).
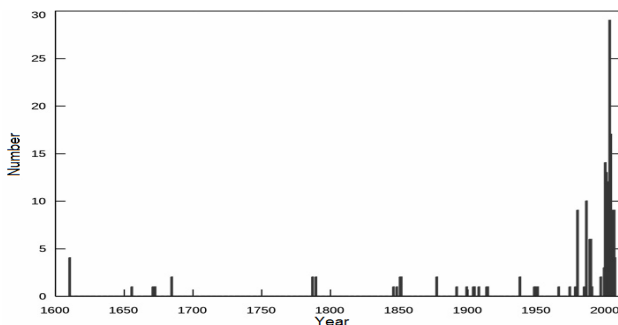
Figure 1: Number of planetary satellites discovered over the course of a year.

In view of the above, the problem of classification of planetary satellites in the Solar System by their size, distribution of mass, gravitational field, shape, etc. has arisen.

The problem of investigation of planets and their moons by spacecraft means is important and requires the most thorough study of their characteristics by methods of celestial mechanics.

2. Problem statement

This study is focused on planetary satellites, the so – called self – gravitating bodies, i.e. bodies which retain their shape by their own mass, mass distribution and resulting gravitational force and tend to bring it closer to the equilibrium. Such moons are called either planets or planetoids or true companions.

What are the criteria to distinguish such planetoids among a total of over 180 planetary satellites? We selected the total mass of a moon as the first criterion while its size is the second criterion and its shape is the third one. It is obvious that a planetary satellite should have a shape close to spherical to be assigned as a planetoid.

The objective of this study is to establish the mentioned criteria and detect the planetary satellites in the Solar System which meet those criteria.

By now there have been a series of studies of this subject carried out by numerous scientists, including K.Kholshenikov, L.Sokolov, B.Kondratiev, O.Zheleznyak, A.Zavizion, A.Vidmachenko, A.Morozhenko, L.Konstantinovskaya, E.Ruskol, A.Ivanov, V.Uralskaya and others.

3. Materials of the study

It was found that the largest moons have a radius which is within the range from 0.002 to 0.270 of the host – planet radius. The only exception is Pluto and its largest moon – Charon. For most of the planets (except for the Earth and Pluto), this range is rather narrow – from 0.002 to 0.042 of the host – planet radius [3].

All major moons (except Triton) are synchronized with their host planets; it means that such a moon rotates with the same side facing its host planet orbiting the Sun (Table 1).

Planetary satellites deviate from hydrostatic equilibrium; hence, they tend to have a shape different from a

spheroid and asymmetric with respect to the axis of rotation and equatorial plane. Besides, unlike asteroids, large moons are evolving objects, so they have inner cores, magnetic fields (some of them), and regular shape [4, 6].

Table 1. Physical characteristics of different moons

№	Name of the moon	Mass, kg 10^{20}	Density, kg·m^{-3}	Mean radius, km	Host planets
1	Ganymede	1481.90	1936	2 634.10	Jupiter
2	Titan	1345.20	1880	2 576.00	Saturn
3	Callisto	1 077.00	1835	2 410.30	Jupiter
4	Io	893.19	3528	1 821.00	Jupiter
5	Moon	734.80	3347	1 737.10	Earth
6	Europe	480.20	3019	1 561.00	Jupiter
7	Triton	214.00	2061	1 354.00	Neptune
8	Titania	35.27	1711	788.50	Uranus
9	Oberon	30.14	1630	761.50	Uranus
10	Rhea	23.07	1234	764.50	Saturn
11	Iapetus	18.06	1089	735.80	Saturn
12	Charon	15.80	1650	606.00	Pluto
13	Ariel	13.50	1670	578.90	Uranus
14	Umbriel	11.75	1405	584.30	Uranus
15	Dione	10.96	1479	562.00	Saturn
16	Tethys	6.18	0986	531.20	Saturn
17	Enceladus	1.10	1610	252.20	Saturn
18	Miranda	0.71	1214	236.50	Uranus
19	Proteus	0.44	1300	210.00	Neptune
20	Mimas	0.38	1160	198.60	Saturn
21	Nereid	0.31	1150	170.00	Neptune
22	Phoebe	0.08	1638	106.50	Saturn

Let us conduct an analysis of mass and size of a celestial body that can have any shape and does not tend to bring it closer to the equilibrium. Suppose the body's mass equals m, its density is ρ; then, its volume is $V = \dfrac{m}{\rho}$,

thus, the radius is $R = \left(\dfrac{m}{\rho}\right)^{\frac{1}{3}}$.

Given that a celestial body is a sphere, we can define the acceleration of gravity on its surface by the formula:

$$g = \frac{Gm}{R^2} = Gm^{\frac{1}{3}}\rho^{\frac{2}{3}} \qquad (1)$$

where G is the gravitational constant.

Now we can estimate the pressure created at the centre of the celestial body by gravity. The pressure created by an uniform column with the height of R in the gravitational field g is defined as follows: $P = \rho g R$.

Then, the pressure inside the celestial body equals to:

$$P = \rho g R = Gm^{\frac{2}{3}}\rho^{\frac{4}{3}} \qquad (2)$$

Thus, there is the pressure on the body from all directions, and if the body shape is unable to withstand the effect of that force, in other words, the body is not spherical, the shift (deformation) resulted from the shear stress occurs. Since elastic solids are able to withstand the shear

stress to some extent, celestial bodies of arbitrary shape are likely to exist.

If the shape of a celestial body is different from a sphere, the shear stress σ in it is of the same order as the pressure P:

$$\sigma = P = Gm^{\frac{2}{3}}\rho^{\frac{4}{3}} \qquad (3)$$

Solid bodies are able to resilient response to the shear stress, but every substance has limited ability to resist. In other words, every solid celestial body has its tensile strength – suppose it equals σ_m. Under the shear stresses that are greater than σ_m, a solid celestial body undergoes irreversible changes in its shape.

Now, based on the conditions $\sigma = \sigma_m$, we can estimate the critical mass $m_{\kappa p}$ and critical radius $R_{\kappa p}$ with which the celestial bodies can only have a shape close to spherical [1].

We can define the critical mass by the formula:

$$m_{\kappa p} = \frac{1}{\rho^2}\left(\frac{\sigma_m}{G}\right)^{\frac{3}{2}} \qquad (4)$$

We can determine the critical radius by the formula:

$$R_{\kappa p} = \frac{1}{\rho^2}\left(\frac{\sigma_m}{G}\right)^{\frac{1}{2}} \qquad (5)$$

Taking into account that most planetary satellites in the Solar system with the shape close to spherical are icy moons, we can suppose that the lower limit to the density is $\rho = 1000\,kg/m^3$ while the tensile strength of ice is $\sigma_m = 3 \cdot 10^6\,N/m^2$ (Table 2).

It is obvious that whether satellite reaches equilibrium shape (i.e. approaches to the spherical shape) or not depends on its composite material (Fig. 2 – 3).

It is clear from the figures that a planetoid or a self – gravitating body in the Solar system, which retains its shape by the weight of its own mass, mass distribution and resulting gravitational force and tends to bring it closer to the equilibrium, is a planetary satellite with the mass and mean radius exceeding critical ones. The smallest moon in the Solar system which meets the above requirements is Miranda.

Table 2. Critical masses and radii for celestial bodies composed of different materials with different densities

Parameters	Composite materials			
	Ice	Regolith	Granite	Iron
Density, kg/m^3	1000	2500	2700	7800
Tensile strength, N/m^2	$3 \cdot 10^6$	$3 \cdot 10^7$	$1 \cdot 10^8$	$1 \cdot 10^9$
Critical mass, kg	$1 \cdot 10^{19}$	$3 \cdot 10^{19}$	$3 \cdot 10^{20}$	$1 \cdot 10^{21}$
Critical radius, km	212	268	453	496
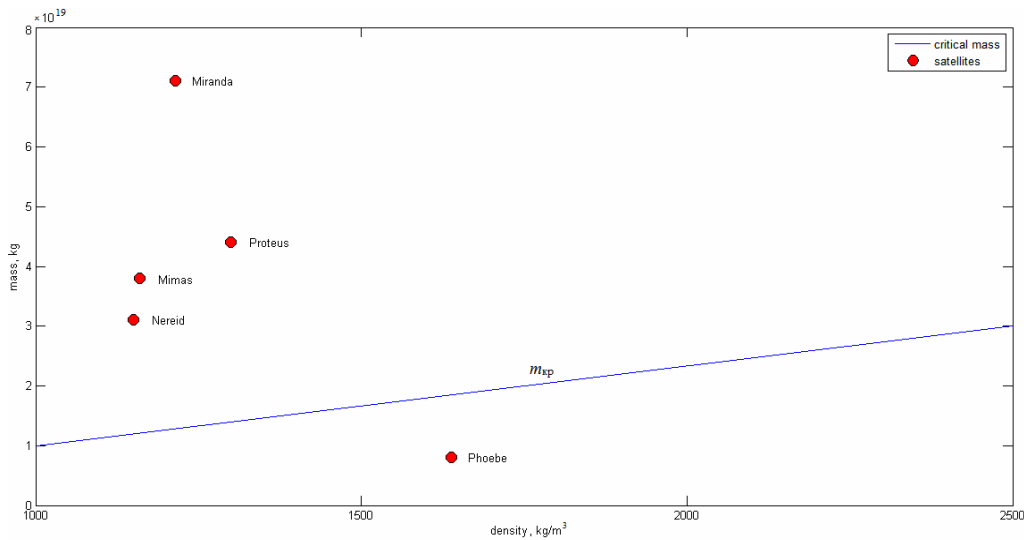
Figure 2: Critical masses for different moons.
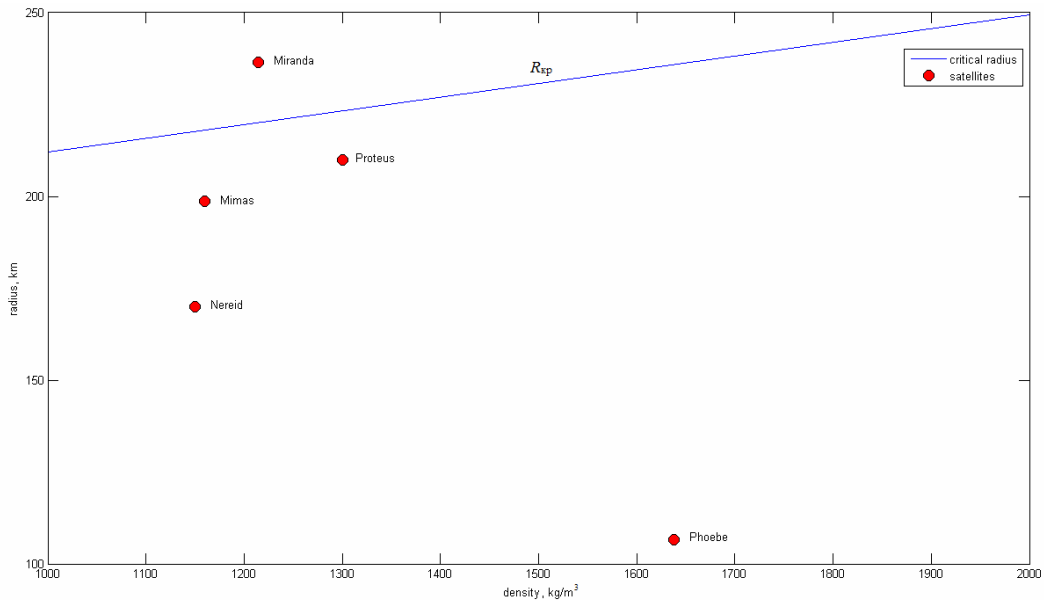
Figure 3: Critical radii for different moons.

Conclusions

It has been found that a natural planetary satellite can be referred to as a planetoid if it is a celestial body of spherical shape with the mass of over 10^{19} kg and mean radius of over 212 km. Celestial bodies with smaller masses remain firm and retain their irregular shapes.

According to the afore – indicated criteria, only 18 moons can be selected from over 180 planetary satellites in all. Saturn has 6 such moons while Uranus – 5, Jupiter – 4, Neptune – 1, the Earth – 1, and Pluto – 1.

Because of the elasticity of composite materials such moons could get nearly spherical shape, and their level surface would coincide with their actual surface. However, that is not the case in fact, which indicates that actual conditions deviate from the hydrostatic equilibrium.

References

Byalko A.V.: 1989, *Earth is our planet*. Moscow, Science, 240 p. (in Russian).
Konstantinovskaya L.V.: 2002, *Math. Meth. Geol. Cycl.*, 9.
Konstantinovskaya L.V.: 2008, *Math. Meth. Geol. Cycl.*, 14.
Natural satellites of the planets: [http://lnfm1.sai.msu.ru/ neb/rw/natsat].
Ruskol E.L.: 2002, *The Earth and the Universe*, 2.
Vidmachenko A.P., Morozhenko O.V.: 2014, *The physical characteristics of surfaces Earth-like planets, dwarf planets and small planet and their satellites from distance research Kyiv*, Prophi (in Ukrainian).

LIGHT POLLUTION IN LEO-SATELLITE TRACKING

L.S.Shakun[1], V.I.Marsakova[2], T.A.Golubovskaya[1], S.S.Terpan[1],
S.M.Melikyants[1], E.A.Korobeynikova[1]

[1] Astronomical Observatory of I.I.Mechnikov Odessa National University
[2] Astronomy Department of I.I.Mechnikov Odessa National University
Shevchenko Park, Odessa 65014, Ukraine
leomspace@gmail.com, v.marsakova@onu.edu.ua

ABSTRACT. Because of the high level of the light pollution in Odessa city, only the observations of LEO (low Earth orbit)-satellites are performed in the main office of the Astronomical observatory of Odessa National University named after I.I. Mechnikov. As the one of the observation results we obtain the sky background measurements along the satellite's way through the sky (at different azimuths and altitudes that change during the satellite tracking). We propose the method of irregular extinction changes diagnostics that realized by using the different data filtration methods. Also as the result of our analysis of these observations we present azimuth-altitude diagram of sky background that shows the most significant light pollution at the north-western and northern directions caused by the Port of Odessa and the stadium "Chernomorets".

Key words: Sky background; light pollution; LEO-satellites: optical observations: reduction; LEO-satellites: photometry.

Observations

Observatory of I.I.Mechnikov Odessa National University that located near historical center of Odessa, in the T.G.Shevchenko park. Thus, only observations of the LEO (Low Earth Orbit) satellites still take place there. The satellites are bright enough and they are observed with relatively short expositions (because of their fast motion) to make the coordinate measurements and the photometry possible.

We perform the observations by using telescope KT-50 with analog CCD-camera WATEC-902H2. The diameter of the main mirror is 50 cm, the focal length is 2 m, the resolution and the field of view on the camera are 0,9 arcsec/pixel and 10 arcmin, consequently. The telescope works in the tracking mode along the satellite's trajectory in the sky.

There are two main aims of these observations: determination of precise positions of the satellites for refinement of their orbits and photometry for determination of their rotational parameters (Shakun & Koshkin, 2013; Shulga et al., 2015). An example of the light variations of the satellite during one track is shown at Fig. 1. Cyclic variations due to rotation is visible.
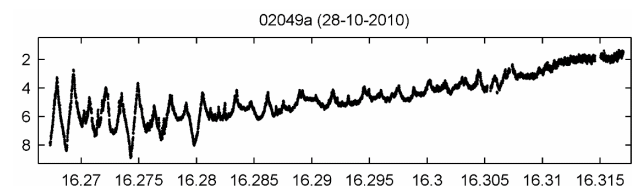
Figure 1: An example of the light variations of the satellite during one track. On horizontal axis is the time in hours, on vertical axis is the brightness in visual magnitudes.

Sky background measurement

As the one of the observation results, we obtain the sequence of images (frames) along the line of satellite way in the sky with intervals between the frames of 0.02 sec. In one clear night we obtain from 10 to 30 satellite tracks. Satellite tracking started in the twilight but we use the observations since the altitude of the Sun is not higher than -14 degrees (this limits was found experimentally, see Fig. 2, for example). The calculation of brightness (here and below) was performed in grayscale units from 0 to 250.
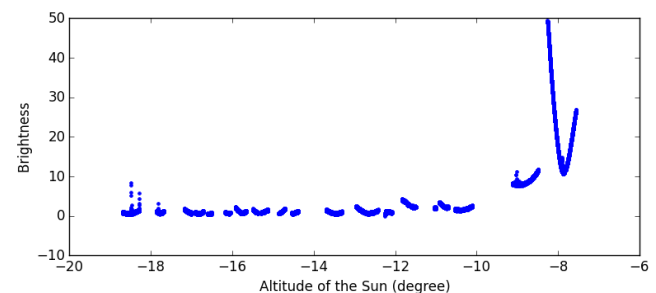
Figure 2: The observed brightness of the sky background in dependence on the altitude of the Sun (12-06-2015).

In this work we studied 647 tracks of satellites during 47 clear nights within 7 months of this year, but the described analysis may be applied to observations in any time interval.

For each image we eliminated all pixels that have brightness higher than certain level (they were marked as objects or stars) and in the rest part of image we calculated average value of the sky background by using the each fourth pixel. Thus, we obtained the average value of the background (average of 100000 pixels) in each frame. Also for each frame the standard deviation of the background was calculated**.**

Detection of sky background irregularities

One of the our purposes is the sorting of tracks into "good" and "bad", because the sky can have the irregularities of the background due to an atmospheric haze, cirrus clouds and other effects that are not visible for observers. To solve this problem we applied the comparison of the smoothing curves obtained by using the methods of "running average" and "median filter" or "running median". First the strongly deviating values were discarded by using "running median". Then the curves of "running average" (with the bigger filter width of 2000 frames) and of "running median" (with the filter width of 50 frames) were compared. The deviations between these curves are shown at Fig. 5. In most cases, the value of deviations lies within from -0.07 to 0.07. (The calculation of brightness was performed in grayscale units from 0 to 250). Therefore, the limit of 0.08 was chosen. If the maximal difference in the track had been higher of this limit then the background changes were considered as "irregular" and the track was refused as "bad". Figures 3-5 illustrate the process of discarding the strongly deviating values of the background and rejection of the "bad" tracks. Fig. 6 gives us the example of the "bad" track.
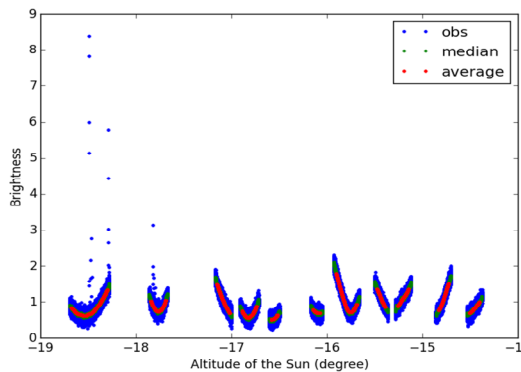
Figure 3: Initial observations of the sky background brightness without previous filtration of random deviations. All tracks on 12-06-2015.
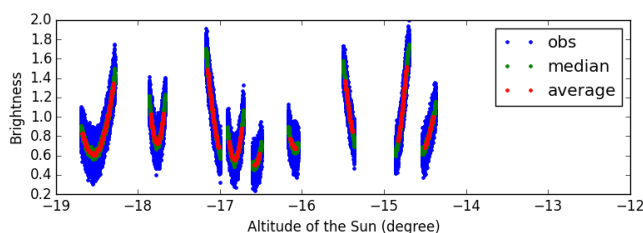
Figure 4: Brightness of the sky background after filtration of random deviations and rejection of the "bad" tracks with irregular changes of the sky background. "Good" tracks on 12-06-2015.
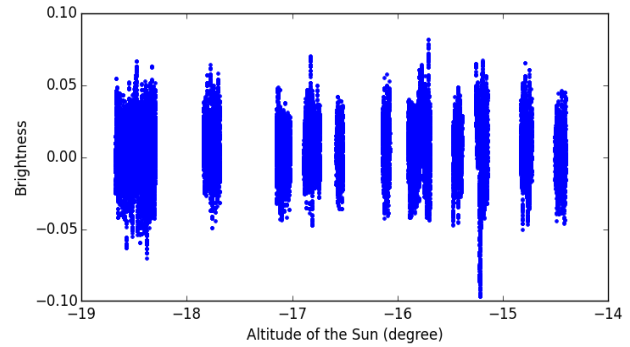
Figure 5: Difference between the approximations of the sky background by using "running average" (with the bigger filter width of 2000 frames) and of "running median" (with the filter width of 50 frames). All tracks on 12-06-2015.
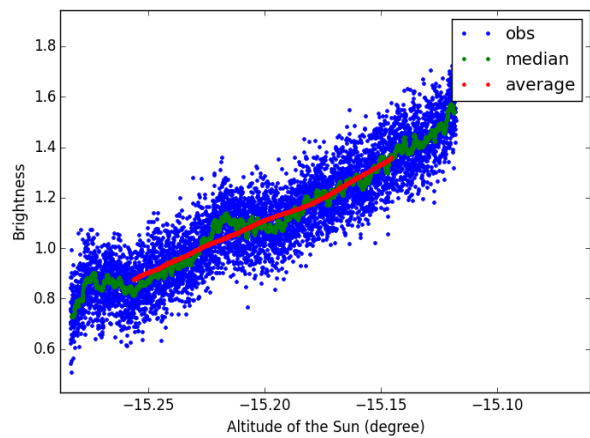
Figure 6: One of the "bad" track with irregular changes of the sky background on 12-06-2015.

Distribution of the background brightness

Our second task was the obtaining of distribution of the background brightness on the sky and determination of its azimuthal dependence for optimization of the observing program. This is important because intense light pollution, small field of view and stretching of stars during the satellite tracking can severely restrict the limiting magnitude of the telescope (In our case the limiting magnitude is about 10.5^m).

As one can see at Fig. 7, the satellite tracks cover a small percentage of the sky hemisphere area. So we gathered the values of sky background brightness in the areas of 25 square degrees (Fig. 8) using the observations within several clear nights with the abundance of the observed tracks. To avoid the discrepancy in background brightness on different dates, we built the dependence of the background brightness of one night on the analogous value of another night. This procedure was performed for all areas, which correspond to the observations on the both dates. The dependence can be well described as linear one (see examples at Fig. 9, 9a) and we calculated the transition coefficients for all nights to transform their background brightness to the level of the one chosen night (12-06-2015 in our example).
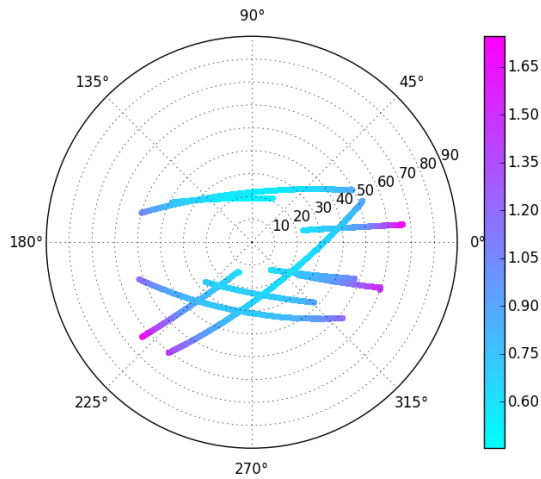
Figure 7: Sky background brightness in the azimuthal coordinates along the satellites tracks. The values of the sky background brightness are shown by using different colors. ("Good" tracks on the date 12-06-2015). Zenith distances is marked on the circles.
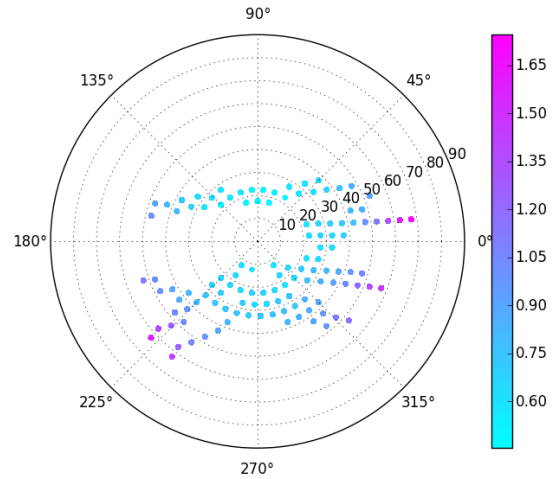
Figure 8: Sky background brightness in the azimuthal coordinates in the areas of 25 square degrees. The value of the sky background brightness is shown by using different colors. ("Good" tracks on the date 12-06-2015).
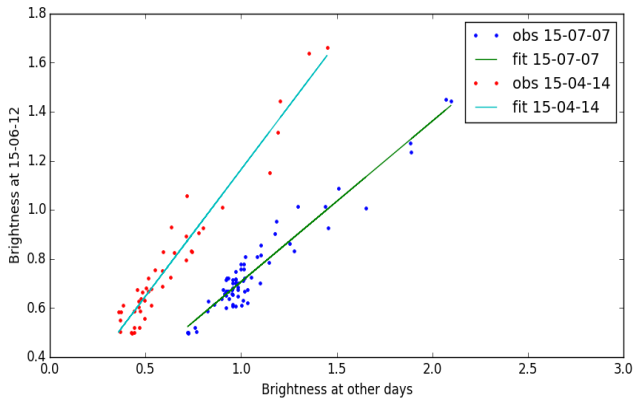
Figure 9: Sky background brightness in the same areas obtained in different "good" nights. comparison of the 14-04-2015, 07-07-2015 with 12-06-2015.
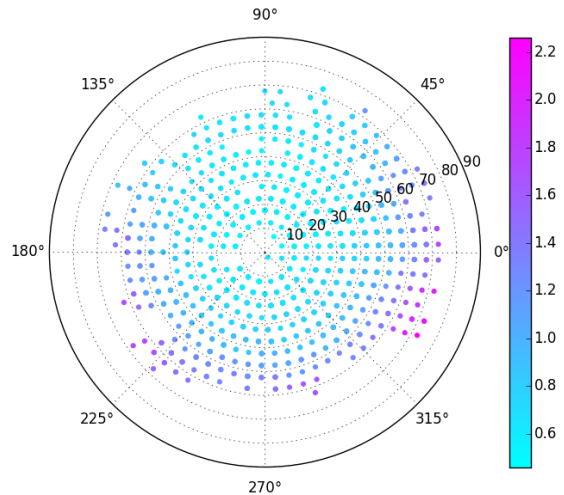
Figure 10: Joint altitude-azimuthal diagram of the sky background brightness. The values of brightness are transformed to ones for the date 12-06-2015. Generally 11 nights (with large amounts of the observations) were used for obtaining of this diagram.
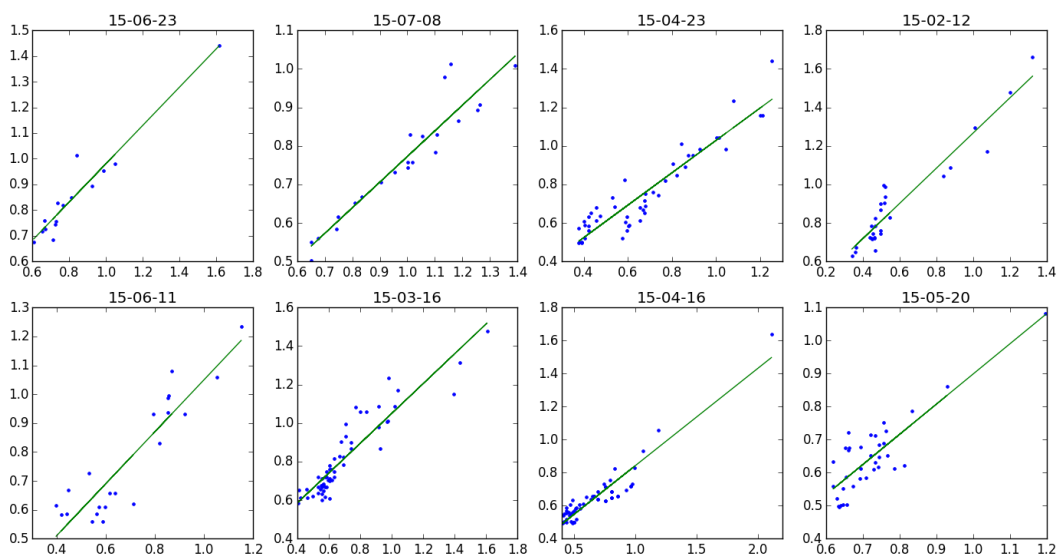
Figure 9a: Some more nights (with sufficient quantities of the observations) in comparison with the 12-06-2015. (See description of the Fig. 9)

Finally, we obtained the joint altitude-azimuthal diagram which show the distribution of the background brightness on the sky (Fig. 10). It shows the significant increase of the light pollution (by the factor 3) in the north-western direction and minimal values of light pollution in the eastern and south-eastern directions. Since we selected the tracks in which the altitude of the Sun was not higher than -14 degrees and satellites were not observed at too low altitudes, it can't be due to the illumination from the Sun on the West side. Most likely, it is light pollution due to the activities of the Odessa Sea Port (in the North-west) and the Stadium "Chernomorets" (in the North). East side (in the direction to the sea away from the Port) is mostly free from light pollution.

Discussion

The method of choosing of "good" tracks (with the regular changes of sky background) is based on the comparison of "running" approximations with narrow and wide filter widths. The main advantage of the method is that the information about the sky background brightness distribution or about transparency of the atmosphere in different directions is not needed a priory. This allows to process a large range of observations that were obtained in different observational conditions. But this approach has a range of certain disadvantages.

Typically the choice of the value for the smaller filter width is not difficult and it can be selected within wide limits. The choice of the value for the larger filter width is associated with a number of difficulties. Firstly, it should be significantly larger than the smaller one and that imposes restrictions on the smaller filter width. Secondly, larger filter width should be significantly wider than the size of irregularities of the sky background of which we want to detect. As such irregularities can vary in a wide range covering the significant part of the size of the track, thus the filter width tends to size comparable to the length of the entire track.

Using the running approximation with a given filter width we either lose the edges of the observation range within of filter half-width, either we deal with edge effects of such smoothing. In our case, the presence of edge effects was very undesirable, as well as the discarding of observa-tions. Thus, the larger filter width was limited by the considerations about the saving of the possible largest number of observations. Therefore, the maximum filter width must be significantly less than the length of the track. The characteristic form of the changes in sky background brightness along the track leads us to the same conclusion.

In case of large zenith distances (more than 70 degrees) the sizes of irregularities (due to both natural reasons and anthropogenic light pollution) become smaller. So it will cause discarding the whole track which cover the low altitudes of the satellite if we use excessively large filter width but that is undesirable.

Thus, we see that there are certain difficulties with the choice of the larger filter width.

The problems described above could be avoided if instead of the low-frequency smoothing we use an approximating model for the brightness of the entire sky. The making of such a model in any case requires a preliminary study of altitude-azimuthal distribution of the sky background brightness, and this task was also performed in this paper.

Conclusion

Thus, the proposed method allows to detect irregular deviations in low-frequency changes of the sky background and it enables automatic selecting of the tracks which were carried on through the cloud cover. So it makes the separation of "good" tracks (suitable for the precise photometry) possible.

Also we propose the method for building of the average light pollution map based on the entire season of LEO-satellite observations. This promotes the preparation of the optimal observations programme.

References

Shakun L.S., Koshkin N.I.: 2013, *Advances in Space Research*, **53**, 1834.

Shulga V. et al.: 2015, *Space Science and Technology*, **21** (3), 74.

THE 15th ANNIVERSARY OF THE ODESSA BRANCH OF THE ISAAC NEWTON INSTITUTE (INI)

Valery Kovtyukh

Astronomical Observatory of Odessa National University,
the Odessa Branch of the Isaac Newton Institute,
Shevchenko Park, 65014, Odessa, Ukraine
val@deneb1.odessa.ua
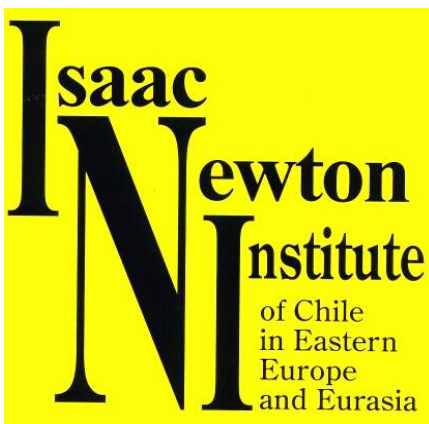
The Isaac Newton Institute (Instituto Isaac Newton) for Astronomical Research (INI) was founded in 1978 by Gonzalo Alcaino (http://www.ini.cl/). The head office is located on the eastern outskirts of Santiago (Chile). Since 1992, the Institute has branched out in several countries of the former Soviet Union in Eastern Europe and Eurasia. The Moscow branch was the first one established outside Chile. As of 2002, there are 14 branches of the Institute in nine countries (see the figure): namely, Armenia (19 members), Bulgaria (28), Crimea (27), Kazakhstan (17), Kiev (11), Moscow (15), Odesa (34), Poland (13), Pushchino (18), St. Petersburg (24), Special Astrophysical Observatory (41), Tajikistan (8), Uzbekistan (19), and Yugoslavia (21). The total number of scientists involved in the project in Eastern Europe and Eurasia is about 300.

INI pursues two major goals, such as offering scientists an opportunity to be published in the most prestigious scholarly journals worldwide and improving motivation to pursue science in the countries with insufficient funding for scientific activities.

As of 2014, there have been 820 articles published. That made INI one of the most productive research centres in the world. Nowadays, more than 300 specialists from nine countries work in INI.

The Odessa Branch of the Isaac Newton Institute was founded in May, 2000, with the aim of contributing to further development of scientific research in observational and theoretical astrophysics in Ukraine. The formal Agreement was signed with Prof. Valentin Karetnikov, the Director of the Astronomical Observatory of Odesa National University.

Alexandr Yuschenko became the first Resident Director of the Odessa Branch of INI; today, this position is held by Valery Kovtyukh.

The results of the studies conducted by the scientists of the Odessa Branch of the Isaac Newton Institute have been submitted for publication to the four most prestigious journals in astronomy and astrophysics, namely the Astrophysical Journal and the Astronomical Journal in the United States (2013 Impact Factors were 6.28 and 4.05, respectively); Astronomy & Astrophysics and Monthly Notices of the Royal Astronomical Society in Europe (2013 Impact Factors were 4.48 and 5.23, respectively).

Today, 20 research workers make up the Odessa Branch staff. The members of the Isaac Newton Institute Branch are actively involved in the following areas of research: studies of chemical composition of stars at different evolutionary phases, such as Cepheids, nonvariable supergiants and their ancestors, B-type Main Sequence stars, metal-poor stars, blue stragglers and lambda Bootis type stars; determination of evolutionary stages and ages of those stars; investigation of the abundance gradient and chemical evolution of the Galaxy. During the indicated research activities the following methods are employed: high dispersion spectral observations at Western observatories, the LTE and non-LTE chemical composition analysis.

The overview of the papers published by Odessa scientists is given in the table below. As of now, the total number of the articles published is 81.

Being involved in fruitful collaboration with the Isaac Newton Institute of Chile, Odessa Astronomical Observatory has significantly levelled up its scientific studies in modern astrophysics.

Let us quote a saying by Luis Ortiz Quiroga, which gives a representative opinion about this institute: «The Isaac Newton Institute is a source of pride for Chile, indeed. Today, this phantom of Gonzalo Alcaino's imagination and creative skill became one of the most productive research centres in the world. It has branches in different countries of Eastern Europe and Eurasia, thereby providing jobs and earnings for tens of experts in astronomical observations. All of them are particularly experienced and skilled though most of them had to reap

the bitter fruits of the USSR collapse. The Institute should be able to raise funds to fulfil its obligations towards its research scientists and implement plans for expansion of its activities domestically and abroad».

Besides, the opinion of a famous politician José Miguel Insulza Salinas should not be left unmentioned: «The Isaac Newton Institute is an unpublished experiment which has worked to the benefit of our country and Eastern Europe. When 10 years ago Gonzalo Alcaino opened up the possibility to establish business relations with a part of the world which Chile was related to only a small extent, he apparently could not figure to himself the consequences of his venture. It resulted in the formation of a scientific network consisting of several hundreds of highly-skilled astronomers scattered to more than 15 observatories in Eastern Europe and former Soviet republics».
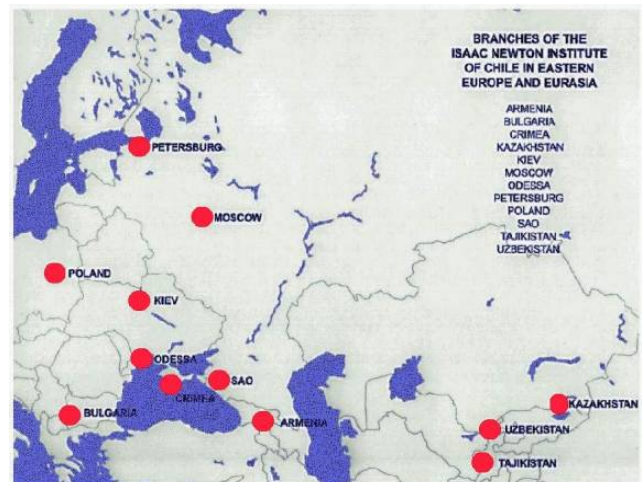
Surname & First name	The number of articles published within the framework of INI in 2000-2015				
	A&A	ApJ	AnJ	MNRAS	Total
Andrievsky, Sergei M.	29	1	2	8	38
Basak, Nina Yu.	1				1
Beletsky, Yu. V.	2				2
Belik, Stanislav I.	2			4	6
Britavskiy, Nikolay E.	3				3
Chekhonadskikh, Fedor A.				3	3
Chernyshova, Irina V.	1				1
Gorbaneva, Tatyana I	1			1	2
Gorlova, Nadezhda I	2				2
Korotin, Sergei A.	23		1	7	31
Kovtyukh, Valery V.	23	2	2	13	40
Mishenina, Tamara V.	8			4	12
Udovichenko, Sergei N.			1		1
Usenko, Igor A.	3	1		1	5
Yasinskaya, Margarita P.				1	1
Yegorova Iryna, A.	4				4